



Faculteit Wetenschappen
Departement Fysica

LOCAL STUDY OF THE BAND GAP AND STRUCTURE OF
DIAMOND-BASED NANOMATERIALS BY ANALYTICAL
TRANSMISSION ELECTRON MICROSCOPY

LOKALE STUDIE VAN DE BANDKLOOF EN STRUCTUUR VAN
DIAMANT GEBASEERDE NANOMATERIALEN MET
ANALYTISCHE TRANSMISSIE ELECTRONEN MICROSCOPIE

Proefschrift voorgelegd tot het behalen van de graad van
Doctor in de Wetenschappen, Fysica
aan de Universiteit Antwerpen, te verdedigen door

Korneychuk Svetlana

Promotor:

Prof. Dr. Jo Verbeeck

Antwerpen, 2018

Chairman

Prof. Dr. Francois Peeters, University of Antwerp, Belgium

Supervisor

Prof. Dr. Jo Verbeeck, University of Antwerp, Belgium

Members

Prof. Dr. Nick Van Remortel, University of Antwerp, Belgium

Prof. Dr. Ken Haenen, Hasselt University, Belgium

Dr. Stuart Turner, Agfa-Gevaert NV, Mortsel, Belgium

Contact information

Svetlana Korneychuk

Univeristy of Antwerp

Faculty of Science

Department of Physics

Groenenborgerlaan 171

2020 Antwerp

Belgium

svetlana.korneychuk@uantwerpen.be

Table of Contents

Preface	1
Samenvatting	3
List of abbreviations	7
Introduction 1. Diamond	9
General properties of diamond	9
Natural diamond	10
Artificial diamond	12
Nanodiamonds	15
Introduction 2. Transmission Electron Microscopy	17
General description of a transmission electron microscope	17
Types of signals in TEM.....	22
Image processing in (S)TEM.....	26
Energy electron loss spectroscopy (EELS) in a transmission electron microscope	28
Chapter 2. Application of TEM on novel diamond based materials	47
Diamond based materials for field emission electron sources.....	48
Diamond plates deposited at low temperature	55
Conclusions	59
Chapter 3. Direct visualisation of the platelet structure in natural Ia diamonds by STEM and EELS	61
Overview of the platelet research.....	62
Visualisation of the platelet.....	62
Determination of the platelet structure	66
Role of nitrogen in the platelet investigated by STEM EELS	68
Conclusions	70
Chapter 4. Band gap measurement of diamond and other high refractive index materials with off-axis EELS using an annular aperture	71
Band gap measurements with EELS in TEM	72
Experimental set-up.....	72
q selection.....	75
Results.....	79
Conclusions	85

Chapter 5. Measurement of the indirect band gap of diamond with EELS.....	87
Probing the band structure with EELS	88
Experiment.....	88
Model.....	91
Results and discussion	95
Conclusions	99
Chapter 6. Future prospects	101
Experiment on partial reconstruction of the band structure.....	101
Conclusions	106
General conclusions.....	107
List of scientific contributions	109
Bibliography.....	113
Thanks	125

Preface

Diamond, a material of extremes and the hardest allotrope of carbon, is formed in the mantle of the Earth at high pressures and temperatures, obtaining its unique physical and mechanical properties. The geological past of natural diamonds leaves traces in the numerous impurities and defects which endow every gemstone with exclusive properties, such as color. Nowadays, the development of fabrication techniques, such as chemical vapor deposition (CVD) allows to produce diamond materials in the laboratory in a controlled way and take advantage of its properties at industrial scale. Diamond based materials find their application in electronics, optics, electrochemistry, photonics, biology etc. For instance, due to its excellent thermal conductivity, diamond can be used as a heat spreader in high electron mobility transistors which operate at high power and tend to overheat. Also, diamond films are perspective materials for large field emitting devices. The combination of diamond with other materials, for instance, hexagonal boron nitride with negative electron affinity, could provide higher emission efficiency. Techniques of diamond synthesis continue to develop, and recent advances in CVD synthesis with linear antenna microwave delivery systems allow to decrease the thermal load on the substrate and deposit good quality diamond films at low temperatures, opening a new field of applications of diamond coatings on the thermally sensitive substrates. Still, either natural gemstone or artificial novel diamond material require detailed investigation, with one of the best techniques being transmission electron microscopy (TEM).

TEM is an ideal tool to study microstructure and composition of the materials at the local scale, routinely providing atomic resolution. A microscope is a versatile tool and can be equipped with an electron energy loss spectrometer which allows to study the composition of the materials including the chemical bonding down to sub-ångström spatial resolution and even investigate dielectric properties including the band gaps with nanometer resolution. The modern monochromators in TEM allow to commonly achieve the energy resolution of about 100 meV in energy electron loss spectroscopy (EELS) and, therefore, study the band gaps of semiconductors and dielectrics on the nanometer scale. However, EELS has not become conventional and widely used due to the ambiguity of data interpretation. The retardation losses, including e.g. Cherenkov radiation emission, occur when a charged particle travels through a dielectric medium at a speed greater than the phase velocity of light in that medium and have an undesirable impact on the low loss signal complicating the retrieval of the band gap signal. For instance, diamond, being an indirect semiconductor with high refractive index, is a very challenging material for the band gap measurement with EELS. Nevertheless, good spatial resolution, the chief advantage of EELS over optical methods, was motivating to push the technique forward and a few methods were developed to overcome the retardation losses and correctly measure the band gaps.

The topic of this thesis is characterization of diamond and related materials with TEM and EELS techniques devoting the first part to the structural and compositional investigation of the novel diamond materials, the second part to the study of the defects in natural diamond and in the last part developing the methods to correctly measure the band gap with EELS emphasizing its application on the diamond which is widely used in the semiconductor devices where the knowledge of band gaps at the local scale is very important.

Preface

- The first part of the introduction gives an overview on natural and artificial diamond materials focusing on the fabrication of diamond films with CVD method. The second part briefly describes the working principle of the transmission electron microscope and types of information which it can provide with the focus on EELS and especially, on the measurement of dielectric properties with EELS.
- The second chapter covers the investigation of two types of novel diamond based materials - the diamond/hexagonal BN heterostructure proposed for field emission devices and the diamond film grown by the novel CVD technique at extremely low temperatures. Both materials were thoroughly studied with high resolution scanning transmission electron microscopy (STEM) and EELS. This revealed the good crystallinity of the hexagonal BN and allowed to explain the superior field emission properties of this heterostructure by the ability of hexagonal BN to grow directly on the diamond surface. On the basis of TEM data the model of hexagonal BN growth was proposed and three mechanism for the unusual plate-like morphology of the diamond film grown at low temperatures were suggested.
- The third chapter is devoted to the study of the nitrogen platelet defect in natural diamond by means of STEM and EELS. This defect is present in 98% of all natural diamonds but its exact crystalline structure remained a mystery since its disclosure about seventy years ago. Based on the high resolution STEM data and novel image processing techniques, the consistent model of the platelet is proposed. The role of nitrogen in the platelet structure is also addressed and its substitutional nature is suggested.
- The fourth chapter presents a technique to measure the band gap of dielectric materials with high refractive index, such as diamond, by means of EELS. The technique relies on the use of a circular (Bessel) aperture and suppresses Cherenkov losses and surface-guided light modes by enforcing a momentum transfer selection. The importance of selecting the optimal experimental convergence and collection angles is highlighted. The effect of the created off-axis acquisition conditions on the selection of the transitions from valence to conduction bands is discussed in detail on a simplified isotropic two band model. The experiment shows interpretable band gap signals on reference samples of diamond, GaN and AlN while offering spatial resolution in the nanometer scale.
- Continuing the ideas on deliberate selection of certain transitions from the previous chapter, the fifth chapter presents a simple method to measure the indirect band gap of diamond with EELS in TEM. The possibility to deliberately select specific transitions of interest is shown and the importance of momentum space resolution in EELS for the accurate measurements of indirect band gap is demonstrated both experimentally and on a simple 2 parabolic band model of the band structure.
- Finally, in the sixth chapter the future prospects are outlined pointing out the emerging possibility to partly reconstruct the band structure with EELS and obtain a distribution of the transitions with the lowest energy from valence to conduction band in momentum space.

Samenvatting

Diamant is een materiaal met uitzonderlijke kenmerken en een van de hardste allotropen van koolstof. Het wordt onder hoge druk en temperatuur gevormd in de mantel van de aarde, waar het zijn unieke fysieke en mechanische eigenschappen ontwikkeld. Het geologisch verleden van natuurlijke diamanten laat sporen na in de vorm van vele onzuiverheden en defecten, welke elke edelsteen voorzien van exclusieve eigenschappen, zoals hun kleur. Tegenwoordig laten moderne technieken, zoals *chemical vapor deposition* (CDV), ons toe om diamant te produceren in een laboratorium op een gecontroleerde wijze, om zo te profiteren van deze eigenschappen op een industriële schaal. Materialen gebaseerd op diamant worden toegepast in elektronica, optica, elektrochemie, fotonica, biologie enz. Zo kan bijvoorbeeld diamant door zijn uitstekende thermische geleidbaarheid gebruikt worden om warmte te verspreiden in transistoren met een hoge elektronen mobiliteit, welke functioneren bij een hoog vermogen en hierdoor de neiging hebben om te oververhitten. Daarnaast tonen diamante films ook potentieel voor gebruik in grote veld emitterend toestellen. De combinatie van diamant met andere materialen, zoals hexagonaal boornitride met een negatieve elektronenaffiniteit, kan zorgen voor een hogere emissie efficiëntie. De syntheses technieken van diamant zijn ook voortdurend in ontwikkeling. Recente vooruitgang in CVD synthese, gebruik makend van lineaire antenne microgolf overdracht systemen, staat ons toe om de thermische belasting op het substraat te verminderen en diamante films van een goede kwaliteit aan te brengen bij lage temperaturen. Dit introduceert een nieuw toepassingsgebied van diamante films op thermisch gevoelige substraten. Zowel natuurlijke als artificiële diamant materialen vereisen echter uitgebreid onderzoek, waarvoor transmissie elektronenmicroscopie (TEM) een van de meest geschikte technieken is.

TEM is een ideale techniek om de microscopische structuur en samenstelling van materialen op lokale schaal te onderzoeken, vaak tot op atomaire resolutie. Een microscoop is een veelzijdig werktuig en kan uitgerust worden met een elektronen energieverlies spectrometer, welke ons toestaat om de samenstelling van materialen, inclusief de chemische bindingen, te onderzoeken met een sub-ångström ruimtelijke resolutie. Het is zelf mogelijk om diëlektrische eigenschappen en de bandkloof te bepalen tot op nanometerschaal. Met de moderne monochomatoren in TEM is het mogelijk om een energieresolutie van ongeveer 100 meV te bereiken, waardoor de bandkloof van halfgeleiders kan onderzocht worden op nanometerschaal. Het toepassen van elektronen energie verlies spectroscopie (EELS) is echter nog niet gebruikelijk door de dubbelzinnigheid in de interpretatie van de data. Wanneer een elektron sneller beweegt doorheen een medium dan de fasesnelheid van het licht in dat medium, zendt het bijvoorbeeld Cerenkovstraling uit, wat leidt tot een energieverlies voor het elektron. Dit heeft een onwenselijke impact op het lage energieverlies gebied in het EELS spectrum en compliceert het onderscheiden van het signaal dat overeenstemt met de bandkloof. Diamant is als indirecte bandkloof halfgeleider met een hoge brekingsindex een uitdagend materiaal voor de bepaling van de bandkloof met EELS. Desalniettemin was de goede ruimtelijke resolutie, een van de grootste voordelen van EELS over optische methoden, een sterke motivatie om de techniek verder te ontwikkelen door te corrigeren voor de ongewenste energieverliezen en op de wijze de bandkloof correct te bepalen.

Samenvatting

Het onderwerp van deze thesis is de karakterisatie van diamant en verwante materialen met TEM en EELS technieken. Het eerste deel is toegewijd aan het onderzoek naar de structuur en samenstelling van de nieuwe diamant materialen, het tweede deel behandelt de studie van defecten in natuurlijk diamant en het laatste stuk betreft de ontwikkeling van de methoden om correct de bandkloof met EELS te bepalen. Bij dit laatste wordt de nadruk gelegd op de toepassing van deze technieken op diamant, welk vaak wordt gebruikt in halfgeleider apparatuur, waar de kennis van de lokale bandkloof onontbeerlijk is.

- Het eerste deel van de inleiding geeft een overzicht van de natuurlijke en artificiële diamant materialen, met de nadruk op de productie van diamante films met de CVD methode. Het tweede deel beschrijft kort het werkingsprincipe van de transmissie elektronenmicroscopie en de verschillende soorten informatie die we ermee kunnen verkrijgen. Hierbij ligt de nadruk op EELS en in het bijzonder het meten van diëlektrische eigenschappen met behulp van EELS.
- Het tweede hoofdstuk behandelt het onderzoek naar twee nieuwe types diamant gebaseerde materialen – de diamant/hexagonale BN heterostructuur voorgesteld voor veldemissie toestellen en de diamant film gegroeid met de nieuwe CVD techniek bij extreem lage temperaturen. Beide materialen werden uitgebreid bestudeerd met hoge resolutie gerasterde transmissie elektronenmicroscopie (STEM) en EELS. Dit toonde aan dat het hexagonale BN een goede kristalstructuur heeft en liet toe om de superieure veldemissie eigenschappen van deze heterostructuur te verklaren doordat de hexagonale BN direct op het diamantoppervlak kan groeien. Op basis van data opgenomen met de TEM, werd het model van hexagonale BN groei voorgesteld. Verder worden ook drie mechanismen voor de ongebruikelijke plaatachtige morfologie van de groei van de diamant film bij lage temperaturen voorgesteld.
- Het derde hoofdstuk is toegewijd aan de studie van het stikstof plaatdefect in natuurlijk diamant met behulp van STEM en EELS. Dit defect komt voor in 98% van al het natuurlijke diamant, maar sinds de ontdekking ervan zo'n zeventig jaar geleden, is zijn precieze kristalstructuur nog steeds ongekend. Op basis van hoge resolutie STEM data en nieuwe beeldverwerkingstechnieken wordt een consistent model voor het plaatdefect voorgesteld. De rol van stikstof in de plaatstructuur wordt onderzocht, en de vervangende rol ervan wordt voorgesteld.
- Het vierde hoofdstuk beschrijft een techniek om de bandkloof van diëlektrische materialen met hoge brekingsindex, zoals diamant, te meten met EELS. De techniek maakt gebruik van een cirkelvormig (Bessel) apertuur en onderdrukt Cerenkov verliezen en oppervlaktegeleide licht modi door een selectie op te leggen aan de impulsoverdracht. Het belang van de keuze voor de optimale experimentele convergentie- en collectiehoeken wordt benadrukt. Het effect van de gecreëerde *off-axis* acquisitievoorwaarden op de selectie van de transitie van valentie- naar conductieband wordt gedetailleerd besproken op basis van een vereenvoudigd en isotroop tweebandenmodel. Het experiment demonstreert interpreteerbare bandkloofsignalen op de referentiematerialen diamant, GaN en AlN, terwijl een ruimtelijke resolutie in de nanometerschaal behaald wordt.

- In het vijfde hoofdstuk wordt verder gebouwd op het idee van de bewuste keuze van bepaalde transities uit het vorige hoofdstuk. Een eenvoudige methode om de indirecte bandkloof van diamant en EELS in TEM te meten wordt voorgesteld. Er wordt getoond dat het mogelijk is om doelgericht specifieke interessante transities te selecteren, en het belang van resolutie in de impulsruimte in EELS voor de accurate meting van de indirecte bandkloof wordt experimenteel aangetoond, alsook op basis van een eenvoudig model met twee parabolische banden als de bandenstructuur.
- Ten slotte worden in het zesde hoofdstuk de toekomstperspectieven opgesteld. Hieruit blijkt duidelijk de opkomende mogelijkheid om de bandenstructuur gedeeltelijk te reconstrueren met EELS en om een verdeling van de transities met de laagste energie van valentie- naar conductieband in de impulsruimte te bekomen.

List of abbreviations

(A)BF	(Annular) Bright Field
a-BN	amorphous Boron Nitride
ADF	Annular Dark Field
ARPES	Angle-Resolved Photoemission Spectroscopy
BFP	Back Focal Plane
BZ	Brillouin Zone
CBED	Convergent Beam Diffraction Pattern
CCD	Charge Coupled Device
CCVD	Combustion Chemical Vapor Deposition
CL	Camera Length
CVD	Chemical Vapor Deposition
DFT	Density Functional Theory
EDX	Energy Dispersive X-ray
EELS	Electron Energy Loss Spectroscopy
EFTEM	Energy Filtered Transmission Electron Microscopy
EPR	Electron Paramagnetic Resonance
EXAFS	Extended X-ray Absorption Fine Structure
EXELFS	Extended Energy-Loss Fine Structure
FCC	Face Centered Cubic
FEE	Field Electron Emission
FEG	Field Emission Gun
FET	Field-Effect Transistor
FFP	Front Focal Plane
FFT	Fast Fourier Transform
FIB	Focused Ion Beam
FTIR	Fourier-Transform Infrared Spectroscopy
GOS	Generalized Oscillator Strength
HAADF	High Angle Annular Dark Field
HEMT	High Electron Mobility Transistor
HFCVD	Hot Filament Chemical Vapor Deposition

List of abbreviations

HPHT	High Pressure High Temperature
HRSTEM	High Resolution Scanning Transmission Electron Microscopy
IP	Image Plane
IR	Infrared
JDOS	Joint Density Of States
MPECVD	Microwave Plasma-Enhanced Chemical Vapor Deposition
NCD	Nanocrystalline Diamond
PCD	Polycrystalline Diamond
RF	Radio Frequency
RIE	Reactive Ion Etching
SE	Secondary Electrons
SEM	Scanning Electron Microscopy
STEM	Scanning Transmission Electron Microscopy
tBN	turbostratic Boron Nitride
TEM	Transmission Electron Microscope(y)
UHV	Ultra High Vacuum
UV	Ultraviolet
XPS	X-ray Photoelectron Spectroscopy
XRD	X-ray Diffraction
ZLP	Zero-Loss Peak

Introduction 1. Diamond

General properties of diamond

Diamond is one of the allotrope modifications of carbon together with graphite, graphene, amorphous carbon, carbon nanotubes etc.[1]. Each carbon atom in diamond is situated in the center of a tetrahedron formed by four neighboring carbon atoms at the corners. Each carbon is sp^3 -hybridized and the four equal covalent bonds have a length of 1.54 Å. Due to the tetrahedral coordination of the atoms, the diamond lattice is face centered cubic (FCC) with a space group $Fd\bar{3}m$ with a translation of $[\frac{1}{4}, \frac{1}{4}, \frac{1}{4}]$ and a lattice parameter of 3.56 Å. It has three main crystallographic planes – {100}, {110} and {111}. This close-packed structure can form only under extreme conditions in nature though several methods mentioned below were developed to synthesize diamond in the lab. The unique strong and symmetrical structure of diamond is the key to its unusual properties and applications in various fields.

Strong covalent bonds and tetrahedral coordination of each atom make diamond the hardest natural material reaching 10 on Mohs hardness scale with very small compressibility. It can, therefore, be used as (nano)indenter to measure hardness of other materials [2] and serves as a coating for cutting tools. On the other hand, compared to hardness, the toughness of diamond is average due to its easy octahedral cleavage in {111} planes making it relatively brittle. This property is used when cutting diamond for jewelry applications.

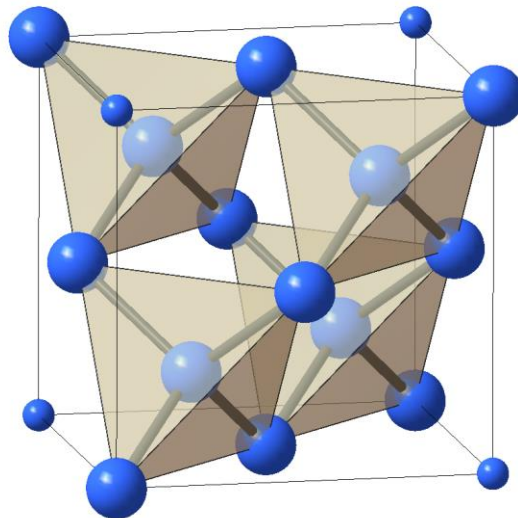


Figure 1.1. Cubic unit cell of diamond showing tetrahedral coordination of each carbon atom.

Surprisingly for an electrical insulator, diamond has good thermal conductivity of 2300 W/(m·K) because of the strong covalent bonds and high sound velocities allowing to easily propagate thermal energy between atoms. This makes diamond highly resistant to thermal shock and thermal lensing and, hence, it can be used as an electrical insulator in heat sink applications to prevent silicon and other materials in semiconductor devices from overheating [3]. Purity of the crystal plays an important role – the higher it is the better diamond conducts heat. Single crystals

Introduction 1. Diamond

outperform polycrystalline diamond in terms of heat conduction. Moreover, diamond is thermally very stable, oxidizing in air above 700°C [4] and remains stable in the non-oxygen environment up to about 1700°C [5].

Optical properties of diamond are unique as well – ideal single crystal diamond is transparent in most of the ultraviolet (UV), visible light and microwave range. Higher-order multiphonon lattice absorption creates a strong absorption band in the 2.5-6 μm region [6]. Pure single diamond crystals are close to this ideal case. However, impurities and intrinsic defects which are present in every real natural or synthetic crystal absorb light in various regions which helps to identify them with light absorption techniques. The refractive index of diamond is high at ~2.4 in the visible range of light and shows a strong dependence on frequency. Diamond is optically isotropic due to its cubic crystal structure.

Table 1.1. General properties of diamond

Property	Value
Density	3,520 kg/m ³
Elastic (Young) modulus (random averaged)	~ 1150 GPa
Hardness	~ 100 GPa
Band gap (indirect)	5.47 eV
Thermal conductivity	2300 W/(m·K)
Debye temperature	2200 K
Refractive index (at 620 nm)	2.41

Defects in diamond are also responsible for its luminescent properties. For example, peculiar luminescent qualities of a single nitrogen vacancy NV⁻ which can serve as a single photon emitter recently have attracted a lot of attention due to its possible application as a qubit in a quantum computer or a sensor of magnetic fields, temperature, molecular environment etc.[7].

Pure diamond is an insulator with an indirect band gap of 5.4-5.5 eV [8] but boron doping, even in small amounts, makes diamond a p-type semiconductor [9]. Phosphorous doping provides diamond with n-type conductivity. Electron and hole mobilities of diamond are the highest among wide-band gap semiconductors, for instance, for a pure single crystal diamond the values are 4,500 $\text{cm}^2\text{V}^{-1}\text{s}^{-1}$ and 3,800 $\text{cm}^2\text{V}^{-1}\text{s}^{-1}$, respectively [10]. Both mobilities are maintained even at high operation temperatures of 400-500 K. High charge mobility together with high saturation velocity (maximum possible velocity of a charge carrier in the presence of the high electrical fields), high predicted dielectric breakdown field and good thermal conductivity makes diamond a very advantageous material for high frequency field-effect transistors (FET) and high power switches and devices such as Schottky diodes [11]. Diamond has also recently been considered as field emission source [12].

Natural diamond

In the history of human kind, diamond was always attracting a lot of attention, thanks to its outstanding properties such as hardness, thermal conductivity, transparency and, of course, indisputable beauty (related to dispersion). Excellent reflectivity of faceted brilliant and multiple varieties of color and shape makes this gemstone an object of desire, which requires careful and

Introduction 1. Diamond

detailed investigation. Natural diamonds are formed from carbon sources of different kinds in the lithospheric mantle of the Earth under high pressure ranging from about 4.5 GPa to 6 GPa and temperatures in the range 900-1300 °C [13]. Diverse conditions of their formation can cause strong variations in the properties of diamonds mined in different parts of the globe [14].

Nitrogen is the main impurity in diamond [15] and can reach up to 0.3 atomic % due to their close match in atomic radiuses making embedding into the diamond lattice much easier for nitrogen than for the majority of other elements. One of the main classifications of natural diamonds is based on the type and quantity of nitrogen impurities [16]. Most of these gemstones contain aggregated forms of nitrogen, mostly A centers formed by two neighboring nitrogen atoms and B centers with four nitrogen atoms around a vacancy [17], and belong to the so-called *I* type. Around 98% of natural diamonds are attributed to the subtype *Ia* with a high amount of nitrogen aggregates which are relatively widespread in the crystal giving it a slight yellow or almost transparent color. On the contrary, in a type *Ib*, nitrogen concentration is much lower and it is distributed more uniformly with mostly single substitutional N occupying isolated sites in the crystal. They strongly absorb blue and green light and, therefore, provide these rare gemstones with deep yellow and even brown color [18]. Only 0.1% of diamonds are of this type.

Diamonds where nitrogen cannot be detected by current means of technology belong to the *II* type. They make up to 1-2% of all natural diamonds and are the purest and most valuable on the market. This second type of diamond is also divided into *a* and *b* categories where the *b* subtype contains boron impurities. Usually, *IIa* diamonds are colorless like, for example, the Beau-Sancy diamond (table 1.1.1) or, sometimes, due to intrinsic imperfections they can have tints of yellow, brown or red like the De Young Red Diamond, the third largest known red diamond.

Table 1.2. Varieties of color in natural diamonds

			
Beau Sancy ¹	De Young Red Diamond ²	Dresden green diamond ³	Koi diamond ⁴

However, not only nitrogen can be present in natural diamonds. It is well known to contain hydrogen [19], nickel [20] and boron [14]. B impurities are quite common in *IIb* type and are responsible for an increase in electrical conductivity acting as acceptors and making diamond a p-

¹ By Heleashard (Own work) [CC BY-SA 3.0], via Wikimedia Commons

² By MBisanz (Own work) [CC BY-SA 3.0 or GFDL], via Wikimedia Commons

³ By Chris73 [CC BY-SA 3.0], via Wikimedia Commons

⁴ By Rawstone Business Holding (Own work) [CC BY-SA 3.0], via Wikimedia Commons

Introduction 1. Diamond

type semiconductor [21]. The color of *I Ib* diamonds can vary from green to grey due to the absorption of red, orange and yellow light by the boron sites.

Properties of natural diamonds can be changed artificially, for example, in order to impart them with a more attractive color. Different ways to manipulate colors of diamond through introducing new defects with radiation and/or temperature [14,22] or removing existing by high pressure high temperature (HPHT) conditions [23] have been developed. Diamonds are also known to change their color under natural radiation (table 1.1, Dresden green diamond).

Impurities mentioned above together with intrinsic imperfections form a wide range of defects in natural diamond including point defects, carbon interstitials, dislocations, platelets and voidites [24]. Among many there are a few that attracted a lot of attention recently like the N-V vacancies. Others, like platelets have been studied for decades but their exact crystalline structure is still not completely clarified. The platelet defect was first detected in the 40s by means of X-ray diffraction (XRD) [25] and found only in nitrogen-rich *Ia* natural diamonds. Platelets are semi-planar structures with size from a few tens of nm to μm oriented along $\langle 100 \rangle$ crystallographic planes in diamond. Remarkably, platelet-like structures were also observed in other materials with FCC lattice - Si [26] and Ge [27]. Dislocations are very widespread in natural and synthetic diamond as well [28]. Voidites, nm sized nitrogen clusters with octahedral shape, are considered as a product of thermal degradation of platelets [29].

Defects and impurities in diamond are commonly studied by light absorption spectroscopy in infrared (IR), visible and UV parts of the spectrum, photoluminescence, cathodoluminescence and electron paramagnetic resonance (EPR) [14,30]. These techniques while having undeniable advantages lack spatial resolution which in some cases makes it difficult to attribute a spectral feature to a specific defect considering their abundant variety in natural diamond.

Transmission electron microscopy (TEM) is capable to directly visualize materials at the atomic scale and can help to obtain missing information about defect structure, or even reveal new defects [31]. For example, this method heavily impacted the investigation of the platelet by directly visualizing the defect and measuring nitrogen concentration precisely in the platelet by means of energy electron loss spectroscopy [32]. These measurements demonstrated that a platelet does not contain enough nitrogen to be a sink of nitrogen aggregates in a *Ia* diamond, as it was suggested before, and different models with mixed carbon and nitrogen interstitials were developed [33,34].

TEM also proved itself as an excellent technique to study dislocations in natural diamond. For example, in order to investigate the correlation between the brown color of natural *I Ia* diamonds and dislocation type Willems *et al.* [35] statistically determined total dislocation density and Burgers vectors of dislocations using TEM. Visualization of the object with atomic resolution also allows to do sanity checks for the theoretical models developed for this object like, for example, in the study on modeling the dissociation and glide motion of the dislocations in *I Ia* natural diamonds [36].

Artificial diamond

Nowadays, diamond synthesis has evolved to the level where artificial diamonds can be given most properties of natural ones, even outperforming them. Synthetic diamonds cover the major part of industry demand. There are a few approaches to produce artificial diamonds which suits best for different purposes.

High pressure high temperature (HPHT)

HPHT method is one of the first developed techniques of diamond synthesis which reproduces natural conditions of the Earth's crust in the lab. A pure carbon source is placed in a specially designed anvil cell where a temperature of about 1300-1500 °C and a pressure of 5-6.5 GPa is applied to synthesize crystals up to about 15 mm [37]. Usually, transition metals such as nickel and cobalt are used as solvent-catalysts in this process as they allow to significantly decrease the required temperature and pressure. Most of HPHT diamonds are of *Ib* type and may contain impurities of the metal catalysts or materials of the anvil cells. Diamonds obtained through the HPHT method find their application in abrasive coatings or as substitution of natural diamonds in jewelry.

Chemical Vapor Deposition (CVD)

Chemical Vapor Deposition (CVD) synthesis together with HPHT pioneered the production of artificial diamonds. In general, CVD is based on the pyrolysis reaction of gas or gases flowing in a chamber towards a heated substrate to be coated. CVD [38] is widely used to perform thin film growth in the semiconductor industry and also to coat cutting tools. This process does not require such extreme conditions as HPHT though the temperature may reach 1600°C. CVD can be accomplished even at atmospheric conditions but in modern systems it is performed at low pressure or ultra-high vacuum in order to eliminate unwanted gas-phase reactions and improve film uniformity across the substrate. Chemical reactions between gas precursors can be enhanced with plasma, microwaves, UV-light, laser or electron beam. This allows to reduce the temperature of the CVD process which can be crucial in production of multilayered semiconductor heterostructures. Carbon containing gases such as methane, carbon monoxide, hydrocarbons, alcohol, ether, can be used as precursors in CVD synthesis of diamond, among which methane is the most frequently used.

Depending on the substrate single- or polycrystalline diamond films can be produced during the CVD process. Monocrystalline diamond can be grown on another monocrystalline diamond substrate or iridium due to its crystalline structure, lattice parameter, thermal stability and catalytic activity [39]. Still, imperfections such as dislocations [40] can appear during the synthesis. Their number can be reduced by consecutively growing a stack of single crystal diamond layers where the top one will have the least defects [41]. Polycrystalline diamond films can be deposited on many substrates, for example, silicon or carbon nitride. Direct growth of diamond film on materials with a different nature can be achieved by spreading nanodiamond seeds on the surface of the substrate [42].

Many types of CVD processes were designed throughout its history each having pros and cons. In particular, a few are used in diamond production [43]. For example, the hot filament CVD (HFCVD) process uses a filament which is kept at higher temperatures than the substrate in order to decompose the gas reagents to free radicals. Meanwhile, the low temperature of the substrate allows to increase the absorption rates. Unfortunately, the deposited diamond film is likely to be contaminated with the material of the filament in this process.

Another suggested method is combustion flame CVD (CCVD) [44] where the flame of a welding torch is placed closely to the substrate. The acetylene/oxygen flame converts into highly reactive intermediates, rapidly interacting with the substrate and forming a strongly adhering

Introduction 1. Diamond

coating. This process is fast and cheap as the growth rates are high and it can be carried out in air, not requiring expensive ultra-high vacuum (UHV) equipment. However, CCVD also has a few disadvantages, for instance, damage of the substrate due to interaction with the flame and the small area of deposition.

The most widespread and best controlled method of diamond synthesis is a microwave plasma-enhanced CVD (MPECVD) carried out at UHV conditions. It is highly reproducible and allows to obtain good quality highly pure diamond films on large surfaces. The mix of gaseous precursors consists of carbon source, usually methane with hydrogen which content is significantly higher than the methane concentration. Nitrogen, trimethylborate or trimethylborane *etc.* can be added into the mixture in order to dope the film with desired elements.

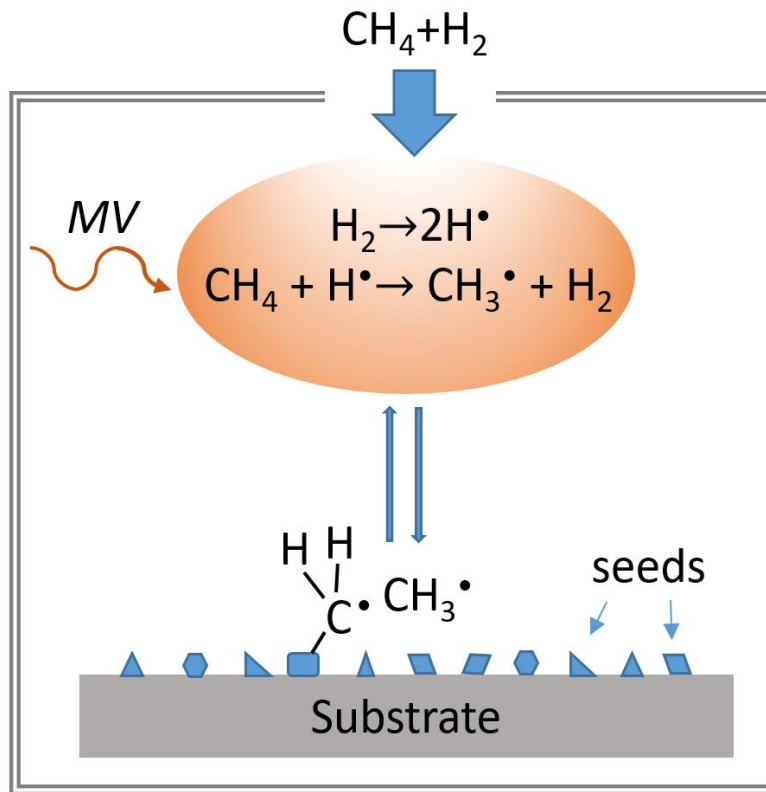
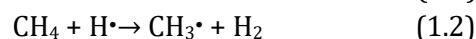


Figure 1.2. Scheme of the microwave plasma-enhanced CVD process of diamond growth.

Chemical reactions in the MPECVD chamber can be described by the following simplified equations (figure 1.2):



The hydrogen molecule dissociates in two radicals in the microwave plasma environment by reaction (1.1). Then the hydrogen radical can interact with the molecule of methane breaking the

Introduction 1. Diamond

C-H bond and creating a methyl radical. In the meanwhile, the hydrogen radical also breaks the dangling bonds at the surface of the diamond seeds or diamond substrate. Due to convection of gases in the CVD chamber, $\text{CH}_3\cdot$ radicals are transported to the substrate where they have non-zero probability to engage with broken dangling bonds at the seed. Omitting the details, this process continues while methyl molecules attach to the surface of the seeds. A large abundance of hydrogen is required to etch away non-diamond carbon formations. This process is described in more detail in the Standard Growth Model for CVD diamond [45]. During the growth of polycrystalline diamond film argon can be added to the gas mixture in order to obtain smaller grains due to renucleation [46].

MPECVD is widely used to deposit diamond layers in semiconductor heterostructures as it allows to create good quality films on large areas and is relatively gentle to the substrate. As mentioned before, diamond has excellent thermal conductivity and can be used to remove extensive heat in semiconductor devices, such as AlGaIn/GaN high electron mobility transistors (HEMTs) which tend to degrade due to overheating. The maximum benefit of diamond's good thermal properties can be exploited by placing a diamond heat spreader as close as possible to the electron channel as AlGaIn/GaN HEMT as it was shown, for example, in this work [47].

The temperature of the diamond deposition during this process is around 1000°C but it can be decreased down to about $350\text{-}410^\circ\text{C}$ by using linear antenna MPECVD [48-50]. In this method a conductive antenna – source of the microwaves, is placed within a few centimeters above the substrate. By controlling the gas flow it is possible to keep the plasma concentration near the substrate much lower than around the antenna and this way the temperature of the diamond growth can be decreased. This method opens attractive opportunities to deposit diamond coatings on more heat sensitive substrates, for example, plastics.

By combination of different deposition techniques various layers can be grown on the CVD diamond film obtained in the previous step. For example, in Hasselt University a boron nitride layer was grown on a polycrystalline diamond (PCD) film by physical vapor deposition [51]. This multilayered material can serve as an efficient field electron emission (FEE) source due to the high carrier mobility of BN and diamond and low work function or even negative electron affinity of BN reported in some works. The diamond substrate helps to grow vertically elongated hexagonal nanowalls of BN right away. This allows to skip the turbostratic stage of BN growth and, hence, improve electron emitting properties. This material also demonstrated low turn-on field, high field enhancement factor and high life-time stability.

Diamond itself can be a good candidate for a FEE source. Its emitting properties can be improved even more by modifying the shape of the diamond layer, for example, creating an array of 1D diamond nanorods on top of the first diamond layer. This structure was grown in Hasselt University by applying a selective seeding technique. Nanodiamonds in a pseudo-stable suspension in deionized water were deposited on top of the polycrystalline diamond film and served as etching mask during reactive ion etching process in an O_2 (80%) gas mixture fabricating vertically aligned diamond nanorods [52]. This structural variant surpasses diamond film in field electron emission.

Nanodiamonds

Nanodiamonds make up the third category of artificial diamonds. They are obtained during controlled explosion of a carbon source inside a closed area when high pressure high temperature

Introduction 1. Diamond

conditions are created for a short time. Besides explosion, nanodiamonds can be synthesized by hydrothermal synthesis, ion and laser bombardment etc. [53]. Natural nanodiamonds are also found in meteorites. It was proposed that they formed due to the high impact events with other cosmic objects. The size of nanodiamonds for most applications varies from 5 nm to 150 nm though smaller nanodiamonds of 1 nm and bigger ones up to 1 μm are known. They find application in many fields including:

- medicine as drug delivery carriers related to their biocompatibility;
- biology in biolabeling with nanodiamonds containing luminescent centers such as NV $^-$, SiV $^-$, GeV $^-$
- sensors of various kinds. Luminescent centers such as NV $^-$, SiV $^-$, GeV $^-$ which naturally occur or can be created in nanodiamonds are sensitive to weak magnetic fields, temperature etc.;
- polishing agent.

Introduction 2. Transmission Electron Microscopy

General description of a transmission electron microscope

The idea to create a microscope where matter can be investigated by electrons was raised as an answer to the limitations of the light optical microscope where the spatial resolution¹ cannot exceed the wavelength of light. On the other hand, electrons accelerated to 300 keV, have a matter wavelength of ~ 1.97 pm which would result in this reasoning to an ultimate spatial resolution of this order of magnitude. The general equation for the matter wavelength of accelerated electron reads:

$$\lambda = \frac{h}{\sqrt{2m_0E(1+\frac{E}{2m_0c^2})}}, \quad (1.3)$$

where E is an acceleration voltage in eV , m_0 is an electron rest mass and c – speed of light in vacuum.

The first prototype of an electron microscope was created by Ernst Ruska in 1932 [54,55]. Soon after that, the resolution of an electron microscope surpassed the optical one. Nowadays, high-end modern microscopes can have spatial resolution of up to 0.5 \AA which allows investigating materials truly at atomic level. Electron microscopes typically operate in two main modes: TEM where the sample is illuminated with a parallel beam and in STEM where a beam is focused and scanned over the sample. Both modes can provide different types of information as described in more details in the next section.

The manipulation of electrons is quite complicated, and the main challenge of an electron microscope is to create a coherent non-aberrated beam which could allow to come as close as possible to the theoretical resolution set by the matter wavelength. This challenging task is accomplished with a sophisticated vertical design of a microscope column where electrons, firstly extracted from the source, are accelerated and then guided down to the sample with a large number of magnetic lenses and apertures (figure 1.3).

Several non-ideal factors affect the performance of the microscope with reduced coherence being an important factor. The first reason of limited coherence in TEM originates from the source of electrons. An ideal electron source should be infinitely small and bright; this leads to good spatial coherence in the parallel beam that hits the sample. Small spread in energy of the extracted electrons and stability in time are equally important factors influencing the observed coherence in the sample plane[56]. The technological evolution of the electron sources went from thermionic sources like a heated tungsten wire to heated field emission guns (FEGs) of the Schottky type or with field emission in a cold-cathode variant (table 1.3). The energy spread of the electron source is mostly responsible for the appearance of the chromatic aberration before hitting the sample. In fact, it worth mentioning that the energy spread of electrons in the beam can also significantly increase by passing through thick samples, for example, those encountered in biology.

An ideal electron source should serve as a point source of spherical waves. However, the whole design of a microscope is dedicated to limit the curvature of the wave front in order to get as

¹ At least in simple setups. Recently great progress has been made in sub-wavelength optical imaging with widely different setups.

Introduction 2. Transmission Electron Microscopy

close as possible to the plane wave front situation and stay in a so-called *paraxial* approximation. This paradox is explained by the limitations of the magnetic lenses outlined below.

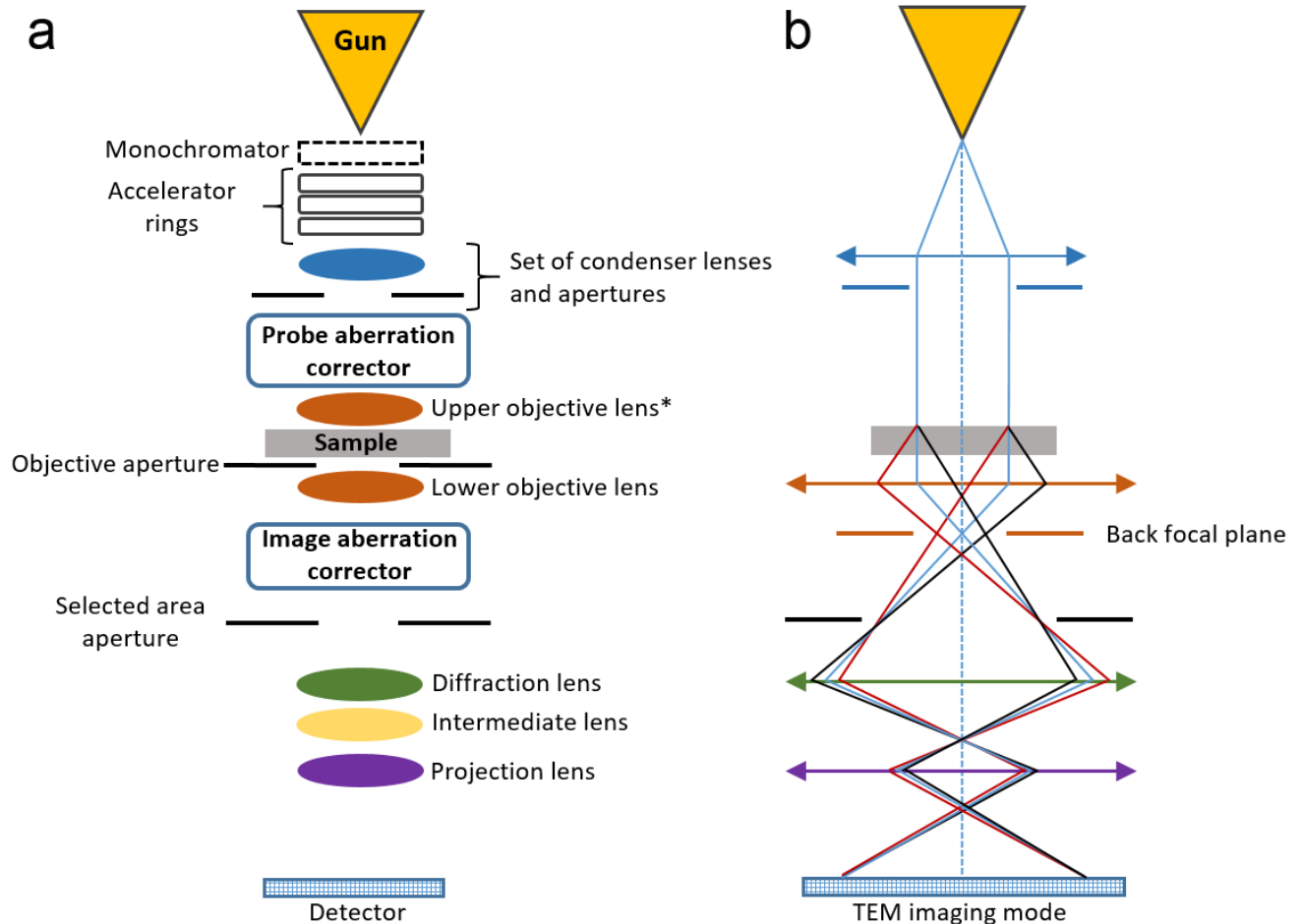


Figure 1.3. a. Simplified scheme of a double aberration-corrected monochromated TEM b. Schematic ray diagram for TEM imaging mode of the microscope (color of parts of the column corresponds to (a), correctors and some parts are omitted for simplicity). *In modern microscopes there are two objective lenses above and below the sample. This situation is shown at (a); ray diagram just demonstrates the case of the one aperture (note that objective aperture is placed on the back focal plane).

Table 1.3. Comparison of different electron sources

Property	W	LaB ₆	Schottky	Cold FEG
Operating temperature, K	2700	1700	1800	300
Operating vacuum, Pa	10 ⁻²	10 ⁻⁴	10 ⁻⁶	10 ⁻⁸
Virtual source size, nm	2500	500	15	2.5
Brightness, A/m ² sr	10 ⁹	5 × 10 ¹⁰	5 × 10 ¹²	10 ¹³
Energy spread, eV	1.5-3	1.3-2.5	~0.7	0.3-0.4
Stability, %/hour	1	1	2	5

Magnetic lenses [57] which guide and focus electrons along the column are the second and the main reason for the distortions of the electron beam. Highly accelerated electrons are to be manipulated the best with a magnetic field¹ and creation of a symmetric magnetic field is not a trivial task. With comparison to optical lenses in light microscopes, magnetic lenses introduce a substantial amount of aberrations while guiding the electrons down the column. The simplest design of a magnetic lens is a hollow cylindrical core – polepiece, made from a soft magnetic material like iron with a copper wire coiled around it. The magnetic field guides the electrons through the middle of the polepiece. Electrons which travel not at the optical axis in a circularly symmetric magnetic field acquire a helical trajectory due to the azimuthal component of the Lorentz force caused by the radial component of the magnetic field; while focusing towards optical axis happens because of the radial component of the Lorentz force created by the interaction of the azimuthal component with the z component of the magnetic field.

There are a few reasons for distortions to appear [58]: chromatic aberration mentioned above; parasitic aberrations arise from deviations from perfect circular symmetry caused by imperfections in the lens polepieces; geometrical aberrations are caused by geometrical properties of the magnetic field itself. There are five primary distortions, called Seidel aberrations: spherical, astigmatism, coma, field curvature, distortion. The last aberration – distortion, starts to play a role only at low magnifications and can be ignored for high magnification work.

How to describe these aberrations? One of the ways was suggested by Hawkes and Kasper [59] and outlined by Marc de Graef [58]. Every point of the wave front P_{initial} after passing through the lens will turn into P_{final} . If the lens is imperfect then the final position will be shifted from the ideal case resulting in a blurred final point which shape is determined by the aberration. This shift can be represented mathematically. Let's assume that a complex number $u = x + iy$ denotes the location of the point in a plane normal to the optical axis. Then the distance between this point and the axis will be $r^2 = uu^*$. In case of an imperfect lens the position of the final point will be shifted by Δu from the ideal case and the final deviation is the sum of all these aberrations:

¹ Electrons accelerated at low voltages (a few keV) can be manipulated as well with electrostatic fields but the operation with highly accelerated electron requires either the electrostatic fields which are not feasible or unreasonably long electrostatic lens. Moreover, it can be proven that aberrations are worse for electrostatic lenses as compared to electromagnetic lenses of the same focal length.

Introduction 2. Transmission Electron Microscopy

$$\begin{aligned}
 \Delta u_{final} = & Cr_{lens}^2 u_{lens} + \quad \leftarrow \text{spherical aberration} \\
 & + 2(K + ik)r_{lens}^2 u_{initial} + (K - ik)u_{lens}^2 u_{initial}^* + \quad \leftarrow \text{coma} \\
 & + (A + ia)u_{initial}^2 u_{lens}^* + \quad \leftarrow \text{astigmatism} \\
 & + Fr_{initial}^2 u_{lens} + \quad \leftarrow \text{field curvature} \\
 & + (D + id)r_{initial}^2 u_{initial} \quad \leftarrow \text{distortion} \quad (1.4)
 \end{aligned}$$

C, K, k, A, a, F, D, d are the real coefficients of the aberrations.

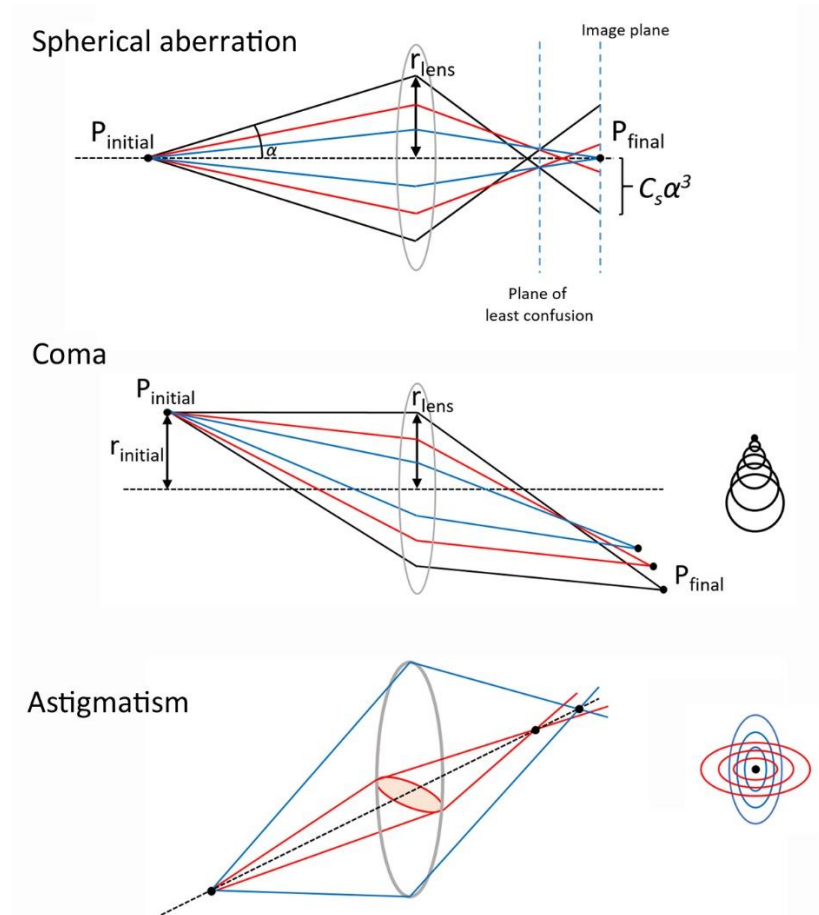


Figure 1.4. Ray diagrams of distortions caused by three main lens aberrations.

The origin of spherical aberration lays in the symmetry of a round magnetic lens as described by Scherzer's theorem. The further an electron is from the optical axis the stronger it focuses by the lens causing the separation of a plane of least confusion where the image is the smallest and the Gaussian image plane. As long as circular symmetry is used, it is impossible to avoid this aberration, yet values for C_s have reached 0.5-1.5 mm.

Coma aberration describes the situation when imaginary rays come out from the same point outside the optical axis and after passing through the lens converge in a set of different back focal planes resulting in a comet-like tail. Besides physical imperfections in the lens this aberration

Introduction 2. Transmission Electron Microscopy

emerges from the lens magnetic field which is not centered on the optical axis or when an aperture is not symmetrically positioned on the optical axis.

Astigmatism occurs when rays that propagate in two perpendicular planes have different foci. It results in the elongation of the image in opposite directions when going through focus. This aberration can be corrected by a special stigmator lens consisting of two magnetic quadruples rotated by 45° degrees according to each other. Due to the linear dependence on u_{lens} astigmatism and field curvature are treated at the same time. Usually, there are two stigmatators – one is for condenser lens, another is for the objective lens.

Geometrical and parasitic aberrations are possible to correct with a set of hexapolar (sometimes, octopolar) lenses which can be tuned to compensate for existing aberrations. Due to technological limitations low aberration conditions of the microscope exist only for electrons which travel very close to the optical axis in a *paraxial* approximation. This means that even for the modern aberration-corrected microscopes the operational angles are in the range of 0-30 mrad. Recently, some new ideas are suggested on how to overcome this limitation, for example, by targeted manipulation of the wave front and adjusting the phase at every point [60].

Let's consider taking an image with one single lens. It is important to highlight that in the paraxial assumption the lens makes a Fourier transform of the wave function in the front focal plane (i.e. the object wave function after undergoing free propagation to the FFP) into the wave function of the back focal plane (BFP):

$$\phi_{bfp} = e^{\pi i k x^2 \left(\frac{1}{f} - \frac{u}{f^2} \right)} \tilde{\psi} \left(\frac{kx}{f} \right); \quad (1.5)$$

and, hence, the wave function at the image plane when imaging with one single lens, can be calculated by applying free propagation from the lens's back focal plane to the image plane (IP):

$$\phi_{ip} \approx \psi \left(-\frac{ux}{v} \right), \quad (1.6)$$

- where u is the distance between the source (point $P_{initial}$) and the lens plane;
- v is the distance from the lens plane to the point P_{final} – image of $P_{initial}$ after passing through the ideal lens;
- f is the focal length.

Thus yielding an inverted and magnified copy of the initial wave function. Such an imaging system would however have fixed focus and magnification.

In real electron microscopes a succession of lenses is used in order to obtain a high flexibility on imaging conditions. Hence, the initial wave function will reproduce through a sequence of ideal lenses up to a magnification factor. It also means that we can modify the wave function by creating an aperture with a certain shape which makes a superposition with a plane wave front and 'shapes' the beam. Different types of beams, for example, Vortex or Bessel, can be obtained by producing the right shape of the aperture.

Let's describe in more detail the creation of a special beam on the example of a Bessel beam. This beam came to the attention for optics applications after the works by Durnin [61] who showed

Introduction 2. Transmission Electron Microscopy

that a beam with an amplitude distribution described by a first order Bessel function normal to the direction of propagation will possess non-diffractive self-healing properties and, thence, high (in theory infinite) depth of focus. In electron optics, recent works [62,63] demonstrated the possibilities to create such beams in TEM. Electron Bessel beam can be described by the following equation:

$$\Psi(\rho, \phi, z; t) = J_n(k_\rho \rho) e^{in\phi} e^{-i(tE/\hbar - k_z z)}, \quad (1.7)$$

- where J_n represents an n^{th} order Bessel function of the first kind;
- k_ρ and k_z are transverse and longitudinal wave vector components of the wavefunction;
- the position of the wave front in space is described in the cylindrical polar coordinates: ρ , ϕ , z . t is responsible for the time component of the wave propagation.

For the simple case of zeroth order Bessel function the beam can be written as:

$$\Psi(\rho, z) \propto J_0(k_\rho \rho) e^{ik_z z}; \quad (1.8)$$

Fourier transform of the previous equation will give:

$$\tilde{\Psi}(p_\rho, p_z) \propto \delta(p_\rho - \hbar k_\rho) \delta(p_z - \hbar k_z), \quad (1.9)$$

where δ marks the Dirac delta function, p_ρ, p_z - coordinates of reciprocal space.

It is easy to notice that the Fourier transform (1.9) of a Bessel beam can be considered as a conical superposition of plane waves which can be created by superimposing a thin (in theory infinitely thin) ring aperture function with a planar wavefront. Technically it is impossible to create such infinitely thin ring required for an ideal Bessel beam but a ratio of 9/10 between the radii of inner and outer circles is already sufficient to produce a very good approximation to the ideal case. This type of a ring-shaped Bessel aperture will play a major role in the experimental part of this work in Chapter 4. Other types of beams like Vortex [64], Gaussian [65] or Helix, standing outside current work, can be manufactured as well using the same approach.

Types of signals in TEM

Different types of signals are generated when an electron beam interacts with the sample [66]. In TEM the sample is typically less than a few hundred nanometers thick, and therefore we concentrate here mostly on the electrons that are transmitted through the sample and the signals they generate. The main part consists of the transmitted electrons elastically scattered from the atoms of the sample. This can provide structural information through electron diffraction patterns, or form an image of the sample. Elastic scattering occurs when the electrons interact with the microscopic electrostatic potential of the crystal, made up by the positive nuclei and the electron distribution around them. Another important part of the signal consists of inelastically scattered electrons which lost a fraction of their energy interacting with the electron cloud of the atoms in a specimen and, hence, carry information about the chemical bonds and dielectric response of the material. Separation of the scattering events into elastic and inelastic is done for simplicity as, for

Introduction 2. Transmission Electron Microscopy

'elastic' scattering it is difficult to define if there really was no energy transfer between sample and electron and often the term quasi-elastic is used here.

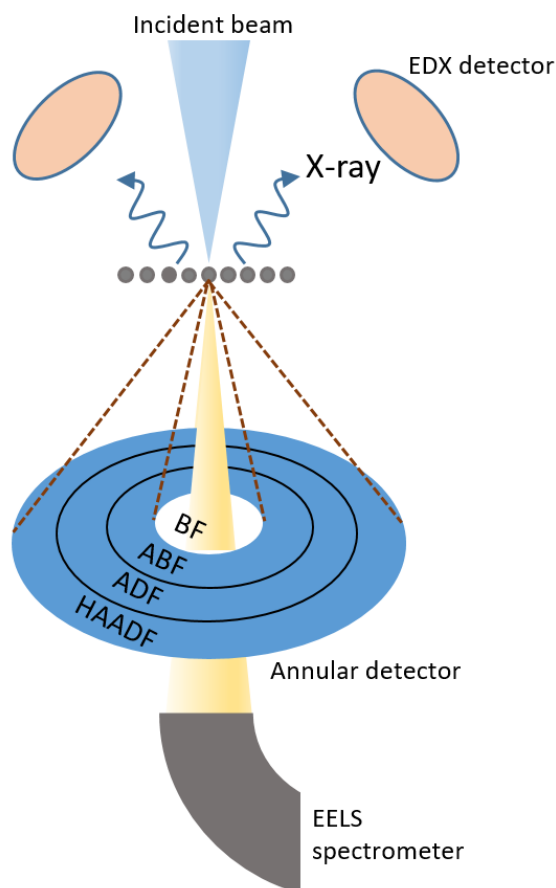


Figure 1.5. Standard detection scheme of an electron microscope in STEM mode.

X-ray signals are also generated during the interaction of the sample with the electron beam. Incoming electrons excite electronic states in the sample followed by a de-excitation process which is accompanied by an X-ray being emitted. Energy dispersive X-ray (EDX) spectroscopy [67] is widely used in TEM to estimate the chemical composition of the materials.

Cathodoluminescence [68] is a less common but nevertheless interesting technique in TEM revealing optically transitions in the material with very good energy (due to optical spectrometers) and spatial resolution (due to the localized electron probe). This technique is also highly interesting to study the band gap of materials with high precision.

A small amount of Auger and secondary electrons are also present in the signal generated by the electron beam. Though standard TEM equipment is not typically set up to measure these signals, recent works on TEMs with modified system of detection of secondary electrons (SE) show the possibility to image the surface atomic structure of materials using SE with atomic resolution [69].

Diffraction

Diffraction of electrons on the periodic electrostatic potential of a crystal, can be seen in terms of the Huygens principle. Indeed, each scattering atom can be regarded as the source of a scattered spherical wave originating on this atom, and the interference of all these scattered waves leads to specific directions of diffraction where strong constructive interference occurs. These interference directions cause typical diffraction spots in the far field of the scattering pattern, superimposed on a strong unscattered beam in the center (the so-called zeroth-order beam). Alternatively, the electron wave can be expressed in terms of so-called Bloch eigenstates in the periodic crystal potential and the Schrodinger equation provides the weight of these Bloch states depending on the boundary conditions of the incoming wave. The Bloch states are labelled through their reciprocal vector g and each state corresponds to the occurrence of a specific diffraction peak with the same label g .

Such diffraction patterns carry structural information about the sample and are usually acquired in TEM mode, making use of a plane wave illumination, though nanobeam diffraction in STEM with a small convergence angle and quasi-parallel beam is also common.

Imaging

Materials can be visualized in two operating modes of the microscope: conventional TEM uses a parallel beam illumination and in STEM, a converged beam is scanned over the sample. Contrast in TEM images is formed by interference effects caused by the modulation of the plane wave by the crystal potential, and care should be taken to link the position of these interference effects with the position of atoms, but in general some relation between the actual projected crystal and the image exists. Through-focal series of TEM images can give an opportunity to reconstruct the so-called exit wave, retrieve the phase and remove the aberrations and distortions [70] where the phase now directly relates to the projected electrostatic potential of the crystal. However, recent technological evolution of the TEM has allowed to obtain sub-angstrom probe sizes and atomic resolution STEM imaging became possible. Since then it has taken a major part in visualizing the structure of materials due to its more straightforward interpretation.

Elastic scattering of an electron beam from a nucleus can be described by the Rutherford cross-section:

$$\sigma_R(\theta) = \frac{e^4 Z^2}{16(4\pi\epsilon_0 E_0)^2} \frac{d\Omega}{\sin^4 \frac{\theta}{2}}, \quad (1.10)$$

where e is an electron charge, Z - atomic number, ϵ_0 - dielectric constant of vacuum, Ω - scattering body angle and E_0 - acceleration voltage of a microscope.

Equation (1.10) has one important consequence - elastic scattering from a nuclei is proportional to Z^2 and heavier atoms scatter much stronger than lighter ones. This expression for Rutherford scattering is only valid for high angles as it doesn't take into account wave nature of the electrons including Bragg scattering. In reality the probability of scattering for the same atom varies in different angle ranges, especially for low angles. This factor represents the scattering amplitude of the electron wave from the single atom and is proportional to the elastic cross-section as:

$$|f(\theta)|^2 = \frac{\sigma(\theta)}{d\Omega}, \quad (1.11)$$

Introduction 2. Transmission Electron Microscopy

The equation for the scattering factor can help to describe angular dependence of elastic scattering:

$$f(\theta) = \frac{\left(1 + \frac{E_0}{m_0 c^2}\right)}{8\pi^2 a_0} \left(\frac{\lambda}{\sin\frac{\theta}{2}}\right)^2 (Z - f_x), \quad (1.12)$$

where E_0 is acceleration voltage, λ is wavelength corresponding to E_0 , $a_0 = \frac{4\pi\epsilon_0\hbar^2}{m_0 e^2}$ is Bohr radius and f_x is scattering factor for X-rays which is usually well-known and tabulated.

Typically, STEM detectors are angular, exploiting the lack of azimuthal dependence in equation 1.12 which does not strictly hold in crystals where the structural effect will break the circular symmetry of the scattering (figure 1.5). Due to the different types of signals at smaller and higher scattering angles, there are usually up to four annular ring shaped STEM detectors in a microscope made to collect the electrons which undergo different scattering events. The bright field (BF) detector is meant to pick up the forward-scattered electrons (on-axis) which form a phase contrast image comparable to that in conventional TEM. The annular bright field (ABF) detector also collects forward-scattered electrons but without the central part removing unwanted dynamical effects. These detectors are very sensitive to the diffraction contrast induced by defects or grain boundaries. The annular dark field (ADF) detector is built to collect the intermediate signal between diffraction and mass-thickness contrast. The high angle annular dark field (HAADF) detector is placed further away from the optical axis and is made to acquire the electrons scattered from the nuclei and, therefore, forms mostly Z-contrast images. It is important to remember that the actual signal is determined by the type of atom and the camera length (CL) which is a measure for the magnification of the diffraction pattern and determines the angular collection range of the detectors (table 1.4). For instance, the ADF detector can serve as an ABF detector with a longer CL. An image collected with the same detector and at the same CL for a carbon and Pt specimen can have purely Z-contrast for carbon and carry mostly diffraction contrast for a Pt sample.

Table 1.4. Experimental parameters for acceptance angles of HAADF detector for an FEI cubed Titan at 120kV and 300 kV at various nominal camera lengths.

Camera length, mm	Inner HAADF angle, mrad		Outer HAADF angle, mrad	
	300 kV	120 kV	300 kV	120 kV
29.3	140.2	237.7	320.5	543.4
46.2	92.5	156.9	211.5	358.5
73	62.4	105.7	142.5	241.7
115.9	41.5	70.4	94.9	160.8
182.9	25.7	43.5	58.6	99.4
286.3	16.1	27.3	36.9	62.5
457.5	10.3	17.4	23.5	39.8

Image processing in (S)TEM

Image processing of the (S)TEM images can provide much more additional information about the specimen than at first apparent. For example, the positions of atoms in the crystalline lattice can be precisely estimated from atomic resolution STEM in order to calculate the strain at the atomic scale [71] or to create a relevant model of the structure as a starting point for density functional theory (DFT) calculations. Moreover, image processing can help to correct images for scanning artefacts, such as drift or scanning distortions. New image processing techniques of most relevance for this work will be discussed below.

Commonly, the positions of the atomic columns are estimated from maxima in the intensity line profile extracted from the ADF or HAADF STEM image [72]. For better accuracy, each peak in this line profile can be fitted with a Gaussian or Lorentzian function. This approach gives good results, though it is not optimal as a one-dimensional profile is used to obtain a position of the column which has two dimensions in reality. The software STATSTEM recently developed in EMAT [73] is capable to determine the atomic column position in two dimensions and also calculate scattered intensities for each column. Experimental ADF STEM images serve as a data plane from which the unknown parameters, such as atomic positions or scattering cross-sections can be statistically estimated. As intensity of the atomic column can be approximated with a two-dimensional Gaussian function, the whole ADF STEM image is modeled with a superposition of Gaussian peaks. In this model each pixel with coordinates (x_k, y_l) is given the statistical expectation of its intensity $f_{kl}(\theta)$:

$$f_{kl}(\theta) = \zeta + \sum_{i=1}^I \sum_{m_i}^{M_i} \eta_{m_i} \exp\left(-\frac{(x_k - \beta_{x_{m_i}})^2 + (y_l - \beta_{y_{m_i}})^2}{2\rho_i^2}\right), \quad (1.13)$$

where ζ – is a constant background, ρ_i - the column dependent width of the Gaussian peak, η_{m_i} - the column intensity of the m_i^{th} Gaussian peak, $\beta_{x_{m_i}}$ and $\beta_{y_{m_i}}$ the x - and y -coordinate of the m_i^{th} atomic column respectively. The index i determines the type of atoms in the column with I different types and the index m_i refers to the m^{th} column of type i with M_i the number of columns of type i . θ is a vector of unknown structure parameters:

$$\theta = (\beta_{x_1}, \dots, \beta_{x_{M_1}}, \beta_{y_1}, \dots, \beta_{y_{M_1}}, \dots, \rho_1, \dots, \rho_I, \eta_{m_1}, \dots, \eta_{M_1}, \zeta)^T. \quad (1.14)$$

The parametric model represented by equation (1.13) is fitted to the experimental data using the uniformly weighted least squares criterion quantifying the similarity between the experimental images and the model. The scattering cross-section of each atomic column in case of ADF STEM images can as well be extracted from this model as the intensity of the column approximately represents the total number of electrons collected by the detector. The area under the peak m_i with subtracted background represents the scattering-cross section:

$$V_{m_i} = 2\pi\eta_{m_i}\rho_i^2. \quad (1.15)$$

This gives an opportunity to calculate the number of atoms in one column for a crystalline specimen consisting only of one element. Combining this information with so-called depth-sectioning when the position of an atom in the nanoparticle can be estimated from a through-focal series, the 3D shape of the nanoparticle can be reconstructed [74]. In case of a thin specimen with two elements in the same column such as, for instance, a Ag/Au nanoparticle, the 3D reconstruction

can also be possible by using so-called atomic lensing model [75]. With the prior knowledge about the thickness and shape of the specimen only one HAADF-STEM image is required to extract the 3D information of thin-enough heterogeneous nanostructures.

The aberration-corrected STEM microscopes are very sensitive to acoustical, mechanical or electromagnetic interference which can introduce image distortions at different frequencies. For example, low frequency distortions are mostly caused by the sample/stage drift, and high – by the scan noise [76]. Image distortions can introduce artefacts in the STEM images which may lead, for example, to errors in the estimation of the atomic positions. Each type of distortion should be approached differently and various methods have been proposed to correct for every frequency range.

Arbitrary sample/stage drift makes the actual scanned area a rhombus assuming constant speed and direction of the drift. This distortion can be corrected, for instance, by comparing the corrupted STEM data with its TEM analog. An affine transformation (translation, rotation, dilation, shearing etc.) which corrects for the image drift, can be defined from this comparison [77]. This approach belongs to the so-called rigid registration techniques where all the points of the imaging data are shifted by the same vector and straight lines are preserved.

Scan noise adds a rapidly varying random signal to the beam position and can only be corrected by non-rigid registration. During this transformation different sub-regions of an image may move by differing vectors and straight lines are not necessary preserved. An experimental STEM image is a combination of the actual signal and these time-varying distortions. Assuming that atomic features are circular and without discontinuities, the distortions can be identified and corrected to a certain extent.

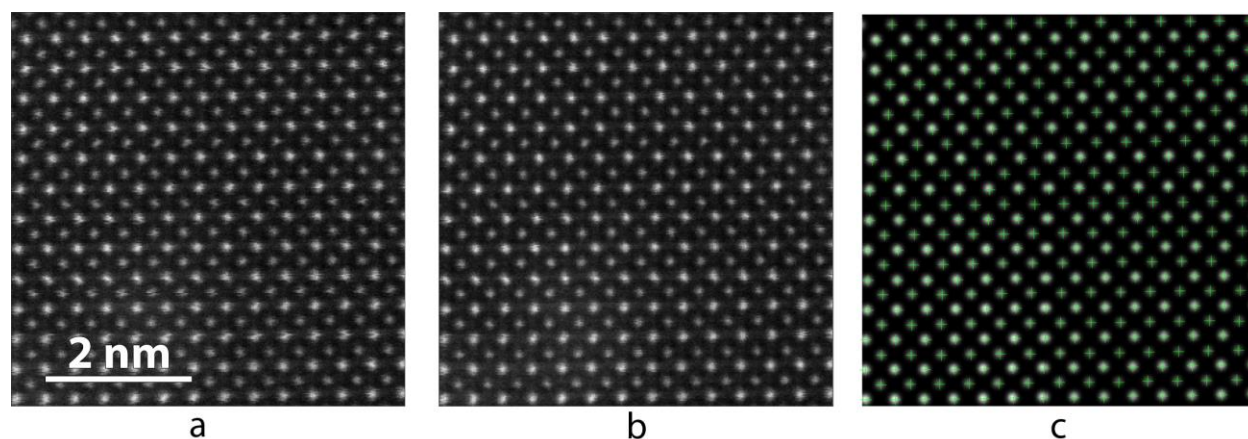


Figure.1.6. a. Experimental HAADF STEM image of strontium titanate. b. Image corrected for scanning artefacts with JitterBug software. c. Refined atomic positions together with fitted Gaussian model in the STATSTEM for input image a.

One of the ways to correct for the scan distortions is implemented in the Jitter Bug software developed in the University of Oxford [78]. In case of the standard line by line scanning scheme in STEM mode, the distortions caused by scan noise can be separated into a component parallel to the scan direction (horizontal) and perpendicular to the scan direction (vertical).

Introduction 2. Transmission Electron Microscopy

To correct for horizontal distortions, a subset of pixels in a row is cross correlated with the row above and below. This way, the average offset is estimated which represents the displacement between the intended and the real probe position due to scan noise.

Vertical distortions appear as a shift of intensity to the lower or higher rows being the most prominent at the top or bottom edges of atomic features. The way to correct them is to obtain first an intensity profile summed horizontally along the atomic feature and then rearrange the intensity of each row in the way that it would decay smoothly to both sides from the brightest row in the middle of the feature. Important to note is that this algorithm assumes a smooth signal which implies oversampling with respect to the Nyquist sampling theorem.

Another approach implemented in the Smart Align software [76], is based on the time image series from which the time-varying distortions can be separated from the genuine sample information. The distortions are identified by the gradient descent method where the differences between the gradient of two grayscale images are used to propose the displacement field between them. One of the images which can be simply taken as an average of the time series, is considered as a reference and stationary and the second one represents an actual image from the time series. It is commonly called 'moving' and adjusted to the reference. The displacement field is calculated as the difference between the intensity of the moving and static images, multiplied by the sum of their gradients. By interactively decreasing the displacement field better scan distortion corrections can be achieved. Then, this procedure is repeated for the next image from the time series.

Energy electron loss spectroscopy (EELS) in a transmission electron microscope

Electrons of the primary beam can lose a fraction of their energy through the Coulomb interaction by exciting atomic electron shells (figure 1.7.a). This interaction is distinguished from the elastic one where the electron also 'feels' the total potential of an atom (nucleus and electron shell) but scatters without any excitation of the target atom (any possible excitation is considered negligible and 'quasi-elastic'). Primary electrons excite the electrons of the specimen atom to empty states above the Fermi level. By measuring the energy loss of the inelastically scattered electrons of the primary beam, information about chemical composition and dielectric properties of the sample can be retrieved [79]. The EELS spectrum between 0-100 eV loss is commonly called a low loss EELS and carries information about dielectric properties of the material such as, plasmonic excitations and transitions from the valence to conduction band as can be seen in figure 1.7.b. The most pronounced feature of the low loss spectrum is a zero-loss peak (ZLP). It is formed by elastically scattered electrons or electrons which lost a non-detectable amount of energy through, for instance, excitation of phonons. The latest generation of monochromators in TEM is capable to provide an energy resolution down to 10 meV and detect some of these phononic modes [80].

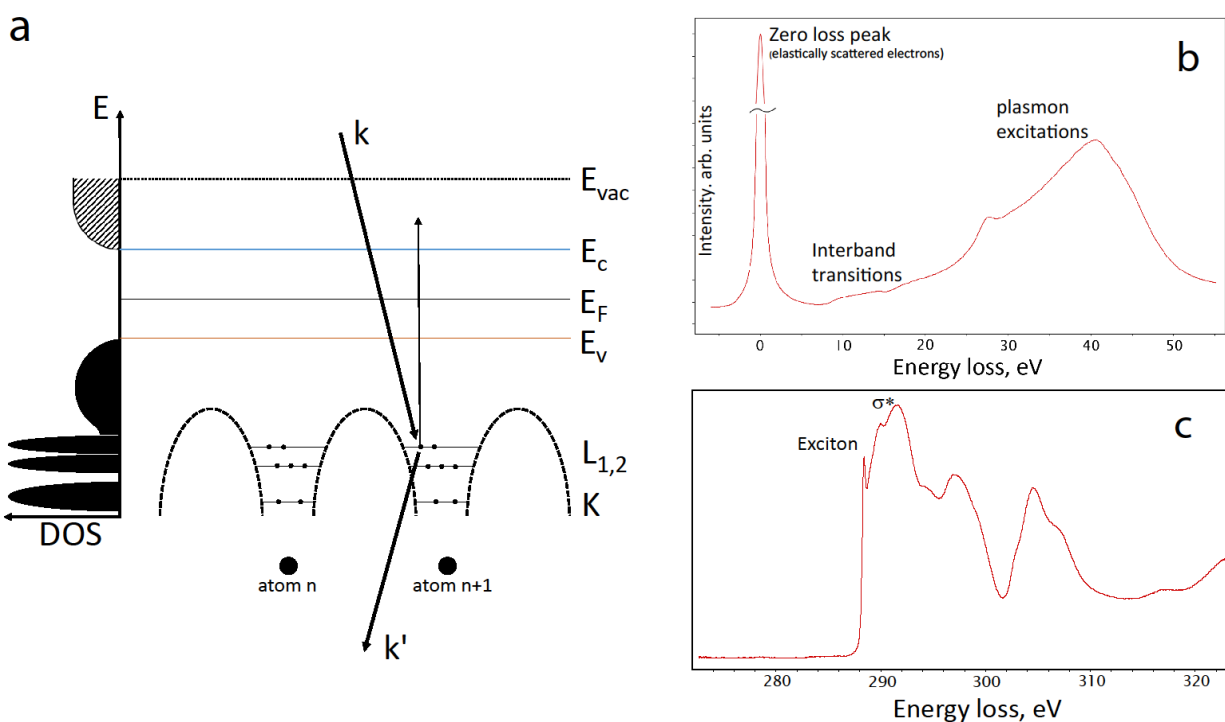


Figure 1.7. a. Scheme of inelastic excitation in the TEM. b. Typical low loss spectrum of CVD polycrystalline diamond. c. Typical core-loss spectrum of CVD polycrystalline diamond.

The core-loss part of the spectrum carries information about the composition of the sample which appears as sharp ionization edges raising above a decreasing background. Their onset energy approximately corresponds to the binding energy of the atomic inner shell and their shape possesses a fine structure which is influenced by the energy and occupation of the final states and can be used as a fingerprint to distinguish, for example, different allotropic forms of carbon or the oxidation state of a transition metal ion. Elemental quantification is also possible by correctly estimating the area under the ionization edge with the removed background which in most cases in the core-loss region can be approximated with a power law function as shown further.

Basic description of the equipment

Energy resolution in the electron microscope is mostly constrained by the quasi-monochromatic electron source and by the limited performance of the current generation of electron spectrometers. The second issue can be partly overcome by going to lower acceleration voltages where the spectrometer appears to perform better. The first issue can be solved by using cold FEGs with smaller energy spread (see table 1.3) but this still will not bring the energy resolution below a few hundreds of meV. To achieve better energy resolution and avoid complications connected to cold FEGs, a monochromator which disperses the electrons by velocity, can be placed right after the gun. The most common design of monochromator is a Wien filter with perpendicular magnetic and electrical fields which at the same time both lay in the perpendicular direction to the path of the primary beam. Those primary electrons which travel parallel to the optical axis with velocity $= \frac{E}{B}$, will continue their path undisturbed, electrons which possess a

Introduction 2. Transmission Electron Microscopy

different velocity will acquire a cycloid motion and can be stopped with an aperture. The central part of this spread consists of electrons with almost equal velocity; by selecting this part with a slit aperture it is possible to obtain a more monochromatic beam and achieve an energy resolution of approximately 100 meV.

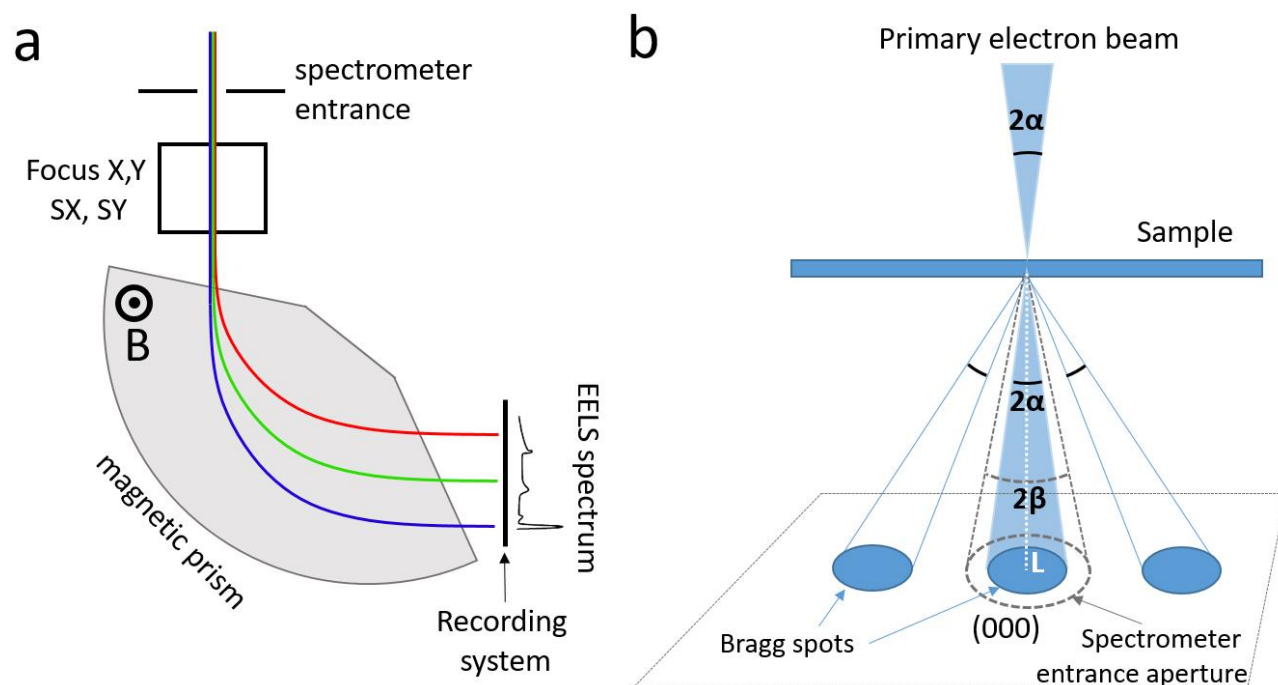


Figure 1.8. a. Approximate scheme of the post-column filter. b. Diagram showing convergence semi-angle α and collection semi-collection angle β in STEM or diffraction mode. The spectrometer entrance lays in the diffraction plane shown at (b).

Two different types of EELS spectrometers are most commonly used in the microscope – one is an in-column filter installed between the sample and detector (the so-called Ω -filter) and another one is a post-column filter. Both of them include a set of correctors for spectrometer aberrations, a magnetic prism (figure 1.8.a) which provides energy dispersion and a recording system, which includes a scintillator, CCD camera and Peltier cooler for the camera. In EMAT a post-column filter is installed on all microscopes equipped with EELS spectrometer. It can operate in two main modes – energy filtered TEM (EFTEM) and EELS mode. In EFTEM mode, the spectrometer selects only those electrons within a certain energy loss range determined by the width and position of an energy selecting slit aperture. Using a set of lenses, the magnified and energy filtered version of the image at the spectrometer entrance is formed at the spectrometer CCD. This can either be a real-space image or energy filtered diffraction pattern. EFTEM mode allows quickly to obtain the distribution of certain elements in the sample but it lacks energy resolution which is limited by the precision of the energy selecting slit and spatial resolution, which is compromised by the presence of chromatic aberration.

In EELS mode the electrons which enter the spectrometer are collected and dispersed by energy obtaining EELS spectra along the energy-dispersive axis. This is usually done in STEM or

Introduction 2. Transmission Electron Microscopy

diffraction mode allowing to calculate the acceptance angle from the size of the entrance aperture. Diffraction mode can be used to collect the average signal from a relatively large region determined by limiting the illuminated area. It can help to increase the signal to noise ratio or to reduce the beam damage by distributing the beam illumination. STEM mode is used to obtain the information on the local scale, even with atomic resolution for the core-loss signal. In diffraction and STEM mode, special care should be taken to choose the right collection angle β . As a rule of thumb it is commonly accepted that the best signal to noise ratio is obtained when β lays in the range of 2-4 θ_E [81] due to the strong directionality of inelastic scattering outlined below. θ_E is the characteristic scattering angle and approximately equals to the energy loss divided by twice the initial energy $E/2E_0$.

Note that convergence angle α and collection angle β are actually *semi*-angles (figure 1.8.b) but they are commonly referred to without using this prefix. In STEM mode the spectrometer entrance aperture is usually placed in the diffraction plane of the microscope collecting the main part of the convergent beam diffraction pattern (CBED) with (000) reflection in the center. The convergence angle can be calibrated from the scattering angle θ between (000) and (hkl) reflections which is twice a Bragg angle θ_B and can be calculated from Bragg's law adopted for the geometry of the electron microscope $\lambda = d\sin\theta$ with $\theta = \lambda/d$ in paraxial conditions, where λ is wavelength of the primary beam electrons and d is a lattice spacing. This angle can be estimated from the distance between the centers of the (000) and (hkl) Bragg reflections in case of small convergence angles when the diffracted disks do not overlap like, for example, on figure 1.8.b. In modern microscopes values of $\alpha \approx 20$ mrad are frequently used providing atomic spatial resolution. This means that CBED disks are in most practical cases intersecting each other for most materials and at most acceleration voltages. In this case the microscope can be switched into diffraction mode (sometimes, just by simply tuning intensity knob and changing the condenser lens current) and a pure diffraction pattern which is now formed at the same plane as CBED can be used to measure the Bragg angle. For calibration of the very small angles laying in the μrad range the regularly spaced gratings could be used, for instance, TEM grids. The collection angle β depends on the radius of the spectrometer entrance aperture R which is typically a fixed parameter. Then $\beta = \frac{\alpha R}{L\theta}$, where L is the camera length, which can be varied over a wide range.

Basic description of inelastic scattering

To continue further with EELS we need to describe the inelastic scattering event first. Expanding the elastic case, we add a term to the Rutherford cross-section introducing the inelastic part [79,66]:

$$\frac{d\sigma}{d\Omega} = \frac{4\gamma^2 Z}{a_0^2 q^4} \left\{ 1 - \frac{1}{[1+(qr_0)^2]^2} \right\}, \quad (1.16)$$

where $\gamma^2 = \left(1 - \frac{v^2}{c^2}\right)^{-1}$, a_0 - Born radius, $r_0 = a_0 Z^{1/3}$ - screening radius for a Wentzel potential in a Thomas-Fermi model which corrects the Rutherford model for the screening of the nuclear field by the atomic electrons. The scattering vector \mathbf{q} determines the momentum transfer between the initial momentum of the electron \mathbf{k}_0 and final momentum \mathbf{k}' (momentum transferred to the atom) and can be approximately written as [81]:

Introduction 2. Transmission Electron Microscopy

$$q^2 \approx k_0^2(\theta^2 + \theta_E^2), \quad (1.17)$$

Where the length of initial momentum vector $k_0 = \frac{2\pi}{\lambda} = \frac{\gamma m_0 v}{\hbar}$ and the characteristic scattering angle $\theta_E = \frac{E}{\gamma m_0 v^2}$ or $E/2E_0$ in a non-relativistic approximation. Combining (1.16) and (1.17) we obtain:

$$\frac{d\sigma}{d\Omega} = \frac{4\gamma^2 Z}{a_0^2 k_0^4} \frac{1}{(\theta^2 + \theta_E^2)^2} \left\{ 1 - \left[\frac{\theta_0^4}{\theta^2 + \theta_E^2 + \theta_0^2} \right] \right\}, \quad (1.18)$$

where the cut-off angle $\theta_0 = (k_0 r_0)^{-1}$ is related to screening effects.

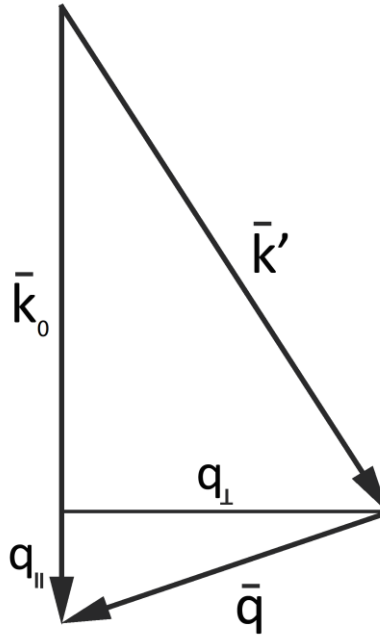


Figure 1.9. Vectorial relations between the components of the inelastic scattering event.

The expression (1.18) brings a few consequences such as proportionality of the inelastic scattering cross-section to a Lorentzian function of type $\sim 1/(\theta^2 + \theta_E^2)$ in the range of $0 < \theta < \theta_E$, so in the range of most angles and after $\theta > \theta_0$ the proportionality drops roughly to $1/\theta^4$. This also means that most of the inelastic events happen in the θ_E range for thin samples (for thicker samples multiple scattering can occur and cause deviations from this rule). This makes the inelastic events rather forward scattering into a small cone around the initial direction. This fact is exploited in spectrometers as they are usually placed at the end of the column, with an entrance aperture meant to collect the transmitted primary beam and the inelastically scattered electrons distributed in a narrow solid angle around it.

Bethe theory

Introduction 2. Transmission Electron Microscopy

Another way to describe inelastic scattering can be approached with the help from quantum mechanics outlined in the revised Bethe theory [82]. It considers the change of initial wave function ψ_0 of the atomic electron to a final state ψ_n after inelastic interaction in the first Born approximation, basically assuming only single scattering events for each atom. The system can be described with the fast electron wave $|k\rangle$ and the atom in its ground state $|0\rangle$. The fast electron can interact with the atom exciting it to the state $|n\rangle$ and losing at the same time some of its momentum to $|k'\rangle$:

$$|\mathbf{k}_0, 0\rangle \Rightarrow |\mathbf{k}', n\rangle, \quad (1.19)$$

Determining the coordinates between the electrons 1...N of the atom and the nucleus as $r_1 \dots r_N$, and r_e as a coordinate between the nucleus and observer, the both states of the system can be described as:

$$\langle \mathbf{r} | \mathbf{k}_0, 0 \rangle = \frac{1}{L^{3/2}} e^{-i\mathbf{k} \cdot \mathbf{r}_e} \psi_0(\mathbf{r}_1, \mathbf{r}_2, \dots, \mathbf{r}_N). \quad (1.20)$$

$$\langle \mathbf{r} | \mathbf{k}', n \rangle = \frac{1}{L^{3/2}} e^{-i\mathbf{k}' \cdot \mathbf{r}_e} \psi_n(\mathbf{r}_1, \mathbf{r}_2, \dots, \mathbf{r}_N), \quad (1.21)$$

where the plane wave is normalized in a box with dimensions L . Vector $\mathbf{r} = (\mathbf{r}_e, \mathbf{r}_1, \mathbf{r}_2, \dots, \mathbf{r}_N)$ determines a position in a $3(N+1)$ -dimensional space.

Regarding the atom as a perturbation, we can describe the probability of excitation in a solid angle Ω as:

$$\begin{aligned} \frac{d\sigma}{d\Omega} &= \frac{k'}{k_0} L^6 \left| \frac{m_0}{2\pi\hbar^2} \langle \mathbf{k}', n | V | \mathbf{k}_0, 0 \rangle \right|^2 = \\ &= \left(\frac{m_0}{2\pi\hbar^2} \right)^2 \frac{k'}{k_0} \left| \int d^3r_e e^{i\mathbf{q} \cdot \mathbf{r}_e} \prod_{i=1}^N \int d^3r_i \psi_n^*(\mathbf{r}_1, \mathbf{r}_2, \dots, \mathbf{r}_N) V(r) \psi_0(\mathbf{r}_1, \mathbf{r}_2, \dots, \mathbf{r}_N) \right|^2. \end{aligned} \quad (1.22)$$

where ψ_n^* - is a complex conjugation of the final wave function; $V(r)$ is the potential of the interaction; $V(r)$ describes the electrostatic interaction potential between an incident fast electron and an atom (basically, it is the negative potential energy of the incoming electron in the field of the atom):

$$V(r) = -\frac{Ze^2}{4\pi\epsilon_0 r_e} + \frac{1}{4\pi\epsilon_0} \sum_{i=1}^Z \frac{e^2}{|\mathbf{r}_e - \mathbf{r}_i|}. \quad (1.23)$$

The first part denotes Coulomb interaction of the fast electron and the nuclei with charge Ze and the second - interaction of a fast electron with all N electrons of the atom with the coordinate r_i . Neglecting phononic excitations, we can assume that the first part turns into zero for inelastic scattering after integration (1.22) due to orthogonality of the initial and final wave functions. This means that inelastic scattering only involves the interaction with atomic electrons and $\langle \mathbf{k}', n | V | \mathbf{k}_0, 0 \rangle$ can be rewritten as:

$$\langle \mathbf{k}', n | V | \mathbf{k}_0, 0 \rangle = \frac{1}{L^3} \prod_{i=1}^N \int d^3r_i \psi_n^* \psi_0 \int d^3r_e e^{i\mathbf{q} \cdot \mathbf{r}_e} \left[\sum_i^Z \frac{e^2}{|\mathbf{r}_e - \mathbf{r}_i|} \right]. \quad (1.24)$$

Making a substitution $\mathbf{r}_e' = \mathbf{r}_e - \mathbf{r}_i$:

Introduction 2. Transmission Electron Microscopy

$$= \frac{1}{L^3} \prod_{i=1}^N \int d^3 r_i \psi_n^* \psi_0 \sum_i^Z e^2 \int \frac{d^3 r'_e e^{iq \cdot (r'_e + r_i)}}{|r'_e|}. \quad (1.25)$$

Integrating $\int \frac{e^{iq \cdot r'_e}}{r'_e} d^3 r'_e = \frac{4\pi}{q^2}$, we obtain:

$$= 4\pi \frac{1}{L^3} \prod_{i=1}^N \int d^3 r_i \psi_n^* \psi_0 \sum_i^Z \frac{e^2}{q^2} e^{iq \cdot r_i}. \quad (1.26)$$

The cross-section for inelastic scattering can be now written as:

$$\frac{d\sigma_n}{d\Omega} = \left(\frac{4Z^2}{a_0^2 q^4} \right) \frac{k'}{k_0} |\varepsilon_n(\mathbf{q})|^2, \quad (1.27)$$

where the first part is attributed to the Rutherford cross-section for elastic scattering and the final part $|\varepsilon_n(\mathbf{q})|^2$ is called an *inelastic form factor* and denotes the square of the modulus of the transition matrix element:

$$\varepsilon_n(\mathbf{q}) = \frac{1}{Z} \langle n | \sum_i^N e^{iq \cdot r_i} | 0 \rangle, \quad (1.28)$$

where Z is atomic number. The inelastic form factor determines the deviation from the Rutherford scattering case caused by interaction of the fast electron with atomic electrons. It characterizes only the target atom or material but does not depend on the velocity of incident electrons.

To further simplify the expression for inelastic scattering cross-section we can introduce the following definition of the generalized oscillator strength (GOS). In a general form it expresses the optical oscillator strength describing absorption of photons by an atom and is closely related to the inelastic form factor:

$$f_n(\mathbf{q}) = \frac{E_n |\varepsilon_n(\mathbf{q})|^2}{R (qa_0)^2}, \quad (1.29)$$

where $R = 13.6$ eV is the Rydberg energy and E_n is the energy loss due to inelastic transition.

EELS spectra are a continuous function of energy in most cases so it makes sense to define a GOS per unit energy loss $\frac{df}{dE}$. Then inelastic scattering event which depends on energy and solid angle Ω can be expressed through a double differential cross-section:

$$\frac{d^2\sigma}{d\Omega dE} = \frac{4\gamma^2 R k'}{E q^2 k_0} \frac{df}{dE}(\mathbf{q}, E), \quad (1.30)$$

In case of $q \rightarrow 0$ the GOS can be considered as a dipole oscillator strength. Applying the conditions of small scattering angles and small energy loss with comparison to the initial energy of an electron, we can approximate momentum transfer with $q^2 = k_0^2(\theta^2 + \theta_E^2)$. The condition for small \mathbf{q} -s where $e^{iq \cdot \mathbf{r}}$ can be substituted with $1 + \mathbf{q} \cdot \mathbf{r}$ is called *dipole region* and in this region $\frac{df}{dE}$ almost does not depend on q and θ . Now equation (1.30) can be written as:

$$\frac{d^2\sigma}{d\Omega dE} = \frac{4\gamma^2 R}{E k_0^2} \left(\frac{1}{\theta^2 + \theta_E^2} \right) \frac{df}{dE}. \quad (1.31)$$

Introduction 2. Transmission Electron Microscopy

The outlined Bethe theory works quite well for describing the scattering from a single atom, for instance, in a gaseous specimen or for inner shell excitations. However, it does not predict the scattering for outer shell excitations in solids due to the presence of collective excitations (such, as plasmons and band structure effects) and due to the fact that valence-electron wavefunctions are modified by the chemical bonding.

Measuring dielectric properties with EELS

Another approach to describe the scattering probability of a primary electron in a material is based on solving the Maxwell equation for a moving charge (electron) passing through a medium with a certain dielectric function ε . The solution can be modified for the exact conditions of the experiment, for instance, shape of the sample, retardation effects etc. [83] which is to be shown further on. Based on this approach, Ritchie [84] suggested a formula which can be used to describe scattering from the outer shells in solids [79].

Dielectric function

The dielectric function determines the response of a material to an external perturbation in the electric field. Assuming isotropic linear material, the dielectric constant ε is defined in terms of the electric field E , the resulting polarization P and the so-called electric displacement vector field D :

$$D = \varepsilon_0 E + P = \varepsilon \varepsilon_0 E, \quad (1.32)$$

where $\varepsilon_0 = 8.85 \cdot 10^{-12}$ F/m – the absolute permittivity of vacuum which remains constant for all the frequencies of the external field. The dielectric function of typical materials depends on frequency as the local charges dynamically respond through polarization of the material. The response of the material arises after the application of an external harmonic field which can be expressed as the real part of a complex exponential function. Because of this, the dielectric function is usually given as a complex function of the angular frequency of this external field ω to be able to express a phase difference ϕ between *stimulus* and response:

$$D_0 e^{-i(\omega t + \phi)} = \varepsilon(\omega) E_0 e^{-i\omega t}, \quad \text{or} \quad \varepsilon(\omega) = \frac{D_0}{E_0} e^{-i\phi}, \quad (1.33)$$

where D_0 and E_0 are the amplitudes of displacement and electric field, respectively and ϕ is the phase angle between them. This complex dielectric function can naturally be separated into real and imaginary parts:

$$\varepsilon(\omega) = \varepsilon'(\omega) + i\varepsilon''(\omega) = \frac{D_0}{E_0} (\cos \phi + i \sin \phi). \quad (1.34)$$

The dielectric function is usually measured by irradiating a material with monochromatic light with different wavelength and determining the refractive index n and absorption coefficient k for each wavelength. The real part of dielectric function is $\varepsilon' = n^2 - k^2$ and the imaginary part $\varepsilon'' =$

Introduction 2. Transmission Electron Microscopy

2nk. In case of electron beam irradiation, the dielectric function also depends on the scattering vector \mathbf{q}^1 but for paraxial conditions the optical value $\varepsilon(0, \omega)$ can be used.

Ritchie formula

The derivation for electron scattering by an infinite medium given by Ritchie states that a transmitted electron with coordinate \mathbf{r} , constant velocity \mathbf{v} and represented by a point charge $-e\delta(\mathbf{r} - \mathbf{v}t)$, creates an electrostatic potential $\phi(\mathbf{r}, t)$ within the medium which depends on time t and coordinate \mathbf{r} by a Poisson equation:

$$\varepsilon_0 \varepsilon(\mathbf{q}, \omega) \nabla^2 \phi(\mathbf{r}, t) = 4\pi e \delta(\mathbf{r}, t), \quad (1.35)$$

so that the potential in Fourier space will be:

$$\phi(\mathbf{q}, \omega) = -\frac{8\pi^2 e}{\varepsilon_0 \varepsilon(\mathbf{q}, \omega)} \frac{\delta(\mathbf{q} \cdot \mathbf{v} + \omega)}{q^2}, \quad (1.36)$$

where

$$\phi(\mathbf{r}, t) = \frac{1}{(2\pi)^4} \int d\mathbf{q} \int d\omega \exp[i(\mathbf{q} \cdot \mathbf{r} + \omega t)] \phi(\mathbf{q}, \omega). \quad (1.37)$$

The transmitted electron which travels in the direction z faces the opposite electrostatic response of the medium which is called a stopping power. The energy loss per unit path can be expressed as the work done by the induced electric field, which is the elementary charge multiplied by the potential gradient in the z -direction $\frac{dE}{dz} = e \frac{d\phi}{dz}$. Then the energy loss per unit path in the medium will give:

$$\frac{dE}{dz} = e \left. \frac{d\phi}{dz} \right|_{r=vt} = -\frac{e}{v} \mathbf{v} \cdot \nabla \phi \Big|_{r=vt}. \quad (1.38)$$

The scattering vector \mathbf{q} can be separated into q_{\perp} and q_{\parallel} and immediately integrated over its parallel component. The stopping power then can be written as:

$$\frac{dE}{dz} = \frac{2\hbar^2}{\pi a_0 m_0 v^2} \iint \frac{q_{\perp} \omega \operatorname{Im} \left[-\frac{1}{\varepsilon(\mathbf{q}, \omega)} \right]}{q_{\perp}^2 + (\omega/v)^2} dq_{\perp} d\omega. \quad (1.39)$$

As can be seen from the equation (1.39), the imaginary part of $1/\varepsilon$ describes the complete response of the material to the fast electron. The stopping power can be connected to the double differential cross-section of EELS as:

$$\frac{dE}{dz} = \iint n_a E \frac{d^2 \sigma}{d\Omega dE} d\Omega dE. \quad (1.40)$$

where the angular frequency is $\omega = E/\hbar$ and n_a is the number of atoms in the sample for normalization.

Combining two expressions (1.40), (1.39) and considering only small scattering angles when $q_{\perp} \approx k_0 \theta$ and $\Omega \approx 2\pi \theta d\theta$, the double differential cross-section for EELS can be written as:

$$\frac{d^2 \sigma}{d\Omega dE} \approx \frac{\operatorname{Im}[-1/\varepsilon(0, E)]}{\pi^2 a_0 m_0 v^2 n_a} \left(\frac{1}{\theta^2 + \theta_E^2} \right). \quad (1.41)$$

¹ For isotropic materials. Dielectric function of anisotropic materials even depends on \mathbf{k}_0 and \mathbf{k}' .

Introduction 2. Transmission Electron Microscopy

As mentioned before, at small angles the dielectric function almost does not depend on \mathbf{q} and can be substituted with the optical one ($q=0$). This assumption holds for materials with weak anisotropy, such as diamond. Highly anisotropic materials, for example, graphite or hexagonal boron nitride give different dielectric response for different directions and, therefore, depend in a stronger manner on \mathbf{q} [85].

The real part of the relative permittivity can be calculated through the Kramers-Kronig relation as shown further. This can help to obtain the dielectric function on a local scale which is out of reach for optical methods. *Vice versa*, comparison of the low loss EELS with the optical data can help with the interpretation of the experiment as retardation losses (see below) might have unwanted impact on the EELS spectra and compromise the retrieval of the dielectric function.

Kramers-Kronig relation

For a single scattering case without retardation losses, the energy loss $S(E)$ can be described by the dielectric function for $q=0$ as [86]:

$$S(E) = \frac{2I_0 l}{\pi a_0 m_0 v^2} \text{Im} \left[-\frac{1}{\varepsilon(E)} \right] \int_0^\beta \frac{\theta d\theta}{\theta^2 + \theta_E^2} = \frac{I_0 l}{\pi a_0 m_0 v^2} \text{Im} \left[-\frac{1}{\varepsilon(E)} \right] \ln \left[1 + \left(\frac{\beta}{\theta_E} \right)^2 \right], \quad (1.42)$$

where I_0 is the integral intensity of the ZLP peak, l is sample thickness. The Kramers-Kronig (KK) relation can be used to express the real part of $1/\varepsilon$:

$$\text{Re} \left[\frac{1}{\varepsilon(E)} \right] = 1 - \frac{2}{\pi} P \int_0^\infty \text{Im} \left[-\frac{1}{\varepsilon(E')} \right] \frac{E' dE'}{E'^2 - E^2}. \quad (1.43)$$

P is a Cauchy principal part of the integral, avoiding the pole at $E=E'$. Therefore, the full dielectric function can be obtained as:

$$\varepsilon(E) = \varepsilon'(E) + i\varepsilon''(E) = \frac{\text{Re}[1/\varepsilon(E)] + i \text{Im}[-1/\varepsilon(E)]}{\{\text{Re}[1/\varepsilon(E)]\}^2 + \{\text{Im}[-1/\varepsilon(E)]\}^2}. \quad (1.44)$$

This relation should be used with care on the experimental data as usually multiple scattering, retardation losses and surface light-guided modes can influence the loss function and modify its shape making the retrieval of the dielectric function problematic. Also, the equation (1.43) requires the EELS spectrum till infinity energy loss which is not feasible. The spectrum can be extrapolated with the function AE^{-r} which resembles the EELS background [79].

Retardation losses in EELS

Besides the dielectric response of the material, fast electrons which travel through samples in TEM can cause unwanted effects such as excitation of surface guided modes and Cherenkov radiation. These unwanted losses are usually referred to as retardation losses. They can have an impact on the experimental spectra complicating the retrieval of, for instance, the band gap value of a material.

Surface guided modes appear in thin samples (for simplicity let's consider the case of a thin foil) when an electron of the primary beam excites collective oscillations of surface electrons. These oscillations are longitudinal waves of surface charge density which can propagate along the interface between the thin foil and vacuum or between the dielectric-conductor interface. The two

Introduction 2. Transmission Electron Microscopy

modes on both sides of the film are connected with a coupling that depends on the thickness of the sample.

The other unwanted loss type is linked to Cherenkov radiation which can happen if the primary electrons travel in a medium faster than light in this medium, so when the condition $v > c/\sqrt{\varepsilon'(E)}$ or, simply, $v > c/n$ is satisfied. Consequently, it is almost impossible to avoid Cherenkov losses for materials with a high refractive index at standard acceleration voltages in TEM. Retardation losses can be estimated numerically for a thin sample making use of the Kröger equation [87] which modifies formula (1.41) by adding a retardation part [88]:

$$\frac{d^2\sigma}{d\Omega dE}(E, \theta) = \left(\frac{1}{\pi a_0 m_0 v^2}\right) \text{Im} \left[\frac{l\mu^2}{\hat{\varepsilon}\phi^2} - \frac{2\theta^2(\hat{\varepsilon}-1)^2}{k_0\phi_0^2\phi^2} (A + B + C) \right], \quad (1.45)$$

This expression was derived by solving Maxwell's equation with appropriate boundary conditions. Kröger formula estimates the differential probability of energy loss, including volume and surface losses, transition radiation, and retardation effects, in a specimen of thickness l for different scattering angles θ and given acceleration voltages. The electron is assumed to be a point charge incident upon the foil with the energy loss so small while passing through it, that the electron velocity can be kept constant. The specimen is assumed to be a thin foil with a dielectric function $\hat{\varepsilon}$ covered from both sides with an infinite dielectric $\hat{\eta}$ (here $\hat{\eta}$ taken as 1 for vacuum). Complex conjugate of the dielectric function is $\hat{\varepsilon} = \varepsilon' - i\varepsilon''$. And

$$\phi^2 = \lambda^2 + \theta_E^2, \quad (1.46)$$

$$\phi_0^2 = \lambda_0^2 + \theta_E^2, \quad (1.47)$$

$$\lambda^2 = \theta^2 - \hat{\varepsilon}\theta_E^2(v/c)^2, \quad (1.48)$$

$$\lambda_0^2 = \theta^2 - \theta_E^2(v/c)^2, \quad (1.49)$$

$$\mu^2 = 1 - \hat{\varepsilon}(v/c)^2, \quad (1.50)$$

The Kröger equation contains separate parts responsible for Cherenkov excitation in bulk (the first term in the square brackets), surface plasmon excitation (term A), and guided light modes in a plan parallel specimen (B+C).

$$A = \frac{\phi_{01}^4}{\hat{\varepsilon}} \left(\frac{\sin^2 d_e}{L^+} + \frac{\cos^2 d_e}{L^-} \right), \quad (1.51)$$

$$B = \frac{v^2}{c^2} \lambda_0 \theta_E \phi_{01}^2 \left(\frac{1}{L^+} - \frac{1}{L^-} \right) \sin(2d_e), \quad (1.52)$$

$$C = -\frac{v^4}{c^4} \lambda_0 \lambda \theta_E^2 \left(\frac{\cos^2 d_e \tanh(\lambda d_e / \theta_E)}{L^+} + \frac{\sin^2 d_e \coth(\lambda d_e / \theta_E)}{L^-} \right), \quad (1.53)$$

where

$$d_e = \frac{lE}{2\hbar v}, \quad (1.54)$$

$$L^+ = \lambda_0 \varepsilon + \lambda \tanh\left(\frac{\lambda d_e}{\theta_E}\right), \quad (1.55)$$

$$L^+ = \lambda_0 \varepsilon + \lambda \coth\left(\frac{\lambda d \varepsilon}{\theta_E}\right), \quad (1.56)$$

$$\phi_{01}^2 = \theta^2 + \theta_E^2 [1 - (\varepsilon - 1)(v^2/c^2)], \quad (1.57)$$

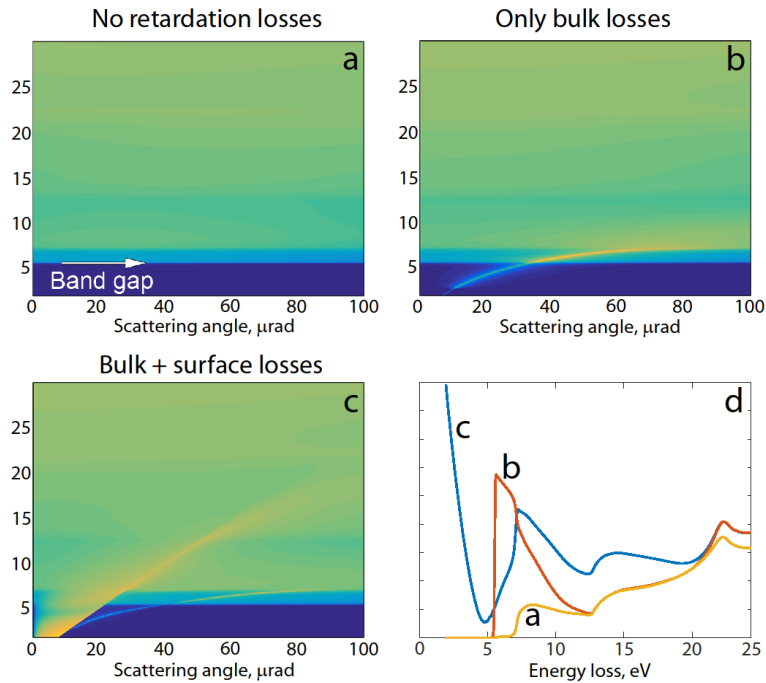


Figure.1.10. Simulated probability of scattering distribution for primary electrons with 60 keV in a diamond film of 50 nm (a) without retardation losses, (b) with only bulk retardation losses attributed to the Cherenkov radiation in bulk and (c) for all the losses including surface plasmon and guided surface modes. (d) Simulated spectra for cases a-c obtained by summing up the angular distribution. Note that retardation losses substantially modify the losses in the vicinity of the band gap onset can easily lead to a wrong interpretation of the band gap in a material.

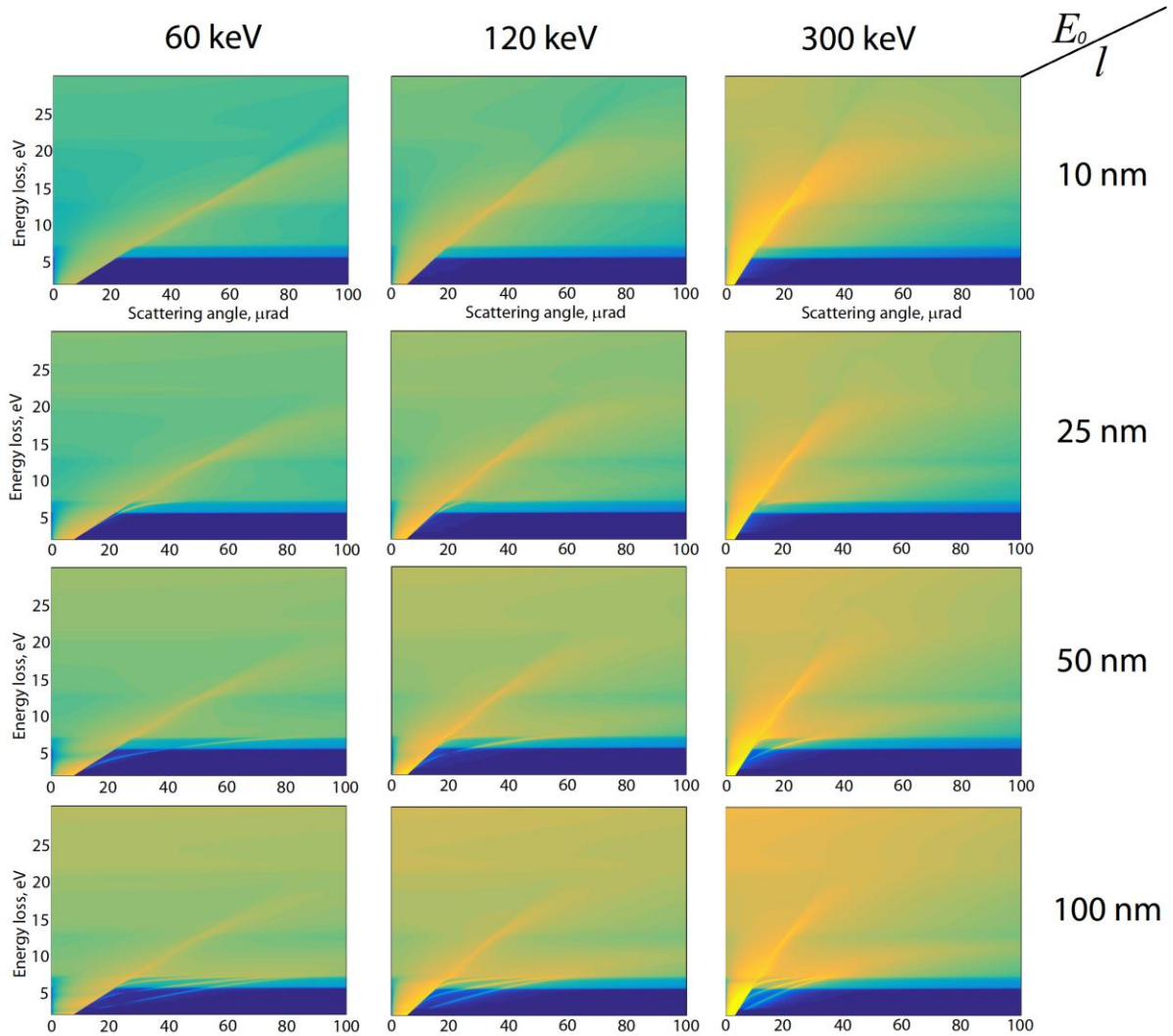


Figure.1.11. Inelastic scattering probability of primary electrons at different acceleration voltages E_0 or the diamond film with different thickness l calculated from the Kröger equation. All retardation losses are taken into account.

Measuring band structure with EELS

Band structure

Valence and conduction energy bands in a crystalline solid can be calculated from Bloch waves, which give a solution for a single-electron Schrödinger equation in a periodic potential [89]:

$$\psi_{nk}(\mathbf{r}) = e^{i\mathbf{k}\cdot\mathbf{r}} u_{nk}(\mathbf{r}), \quad (1.58)$$

where \mathbf{k} is a wavevector. For each \mathbf{k} , there are n solutions to the equation (1.58) which determines the number of energy bands. Each of the energy levels forms a smooth band described by the dispersion relation $E_n(\mathbf{k})$ or $E_n(k_x, k_y, k_z)$ for electrons in band n . All energy bands of a homogeneous

Introduction 2. Transmission Electron Microscopy

crystal can be described within the first Brillouin zone (BZ) represented by a polyhedron in wavevector space. The first BZ is equivalent to the unit cell in real space and is enough to represent the whole crystal in reciprocal space. Special symmetry points and lines of the first BZ are given labels such as Γ , Δ , Λ , Σ (see figure 1.12). The bands can be visualized by plotting $E(k)$ for a given direction in the BZ.

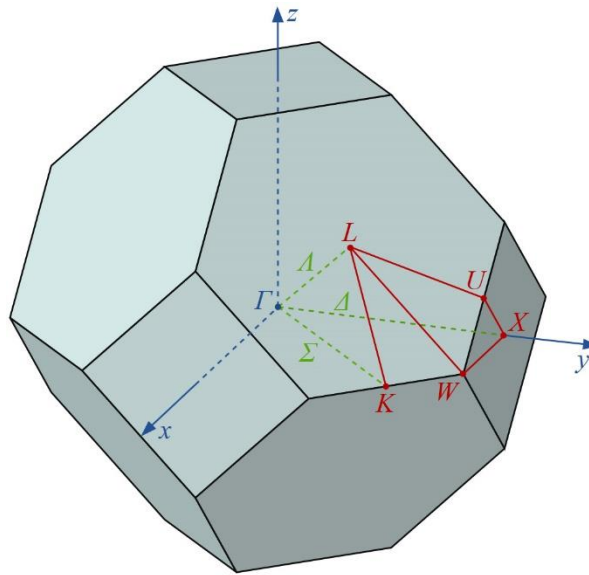


Figure.1.12. First Brillouin zone of a FCC crystalline lattice¹.

EELS measurements

It is possible to measure the energy of interband transitions with EELS as long as the acquired spectra would be free from retardation losses. The first and most obvious measures which can be taken to reduce Cherenkov radiation are to use lower acceleration voltages and thinner samples. This approach can work for low refractive index materials [90] but fails for the ones with high refractive index such as Si and diamond as standard TEM instruments can rarely go below 60 keV. It is important to note that even if it is possible to go below the Cherenkov threshold, the surface losses will remain [91]. As can be seen from the Kröger formula, all the retardation losses appear in a microradian range of angles for typical TEM acceleration voltages, therefore they can be avoided by collecting spectra off-axis [92] or, in other words, by simply shifting the spectrometer entrance which is usually placed in the diffraction plane outside the (000) reflection and collecting only inelastic electrons with a momentum transfer larger than those of the retardation losses (see Chapter 3). This method successfully has proven its efficiency on a variety of samples such as GaAs films [93], SiO₂ [94], diamond [95,96] and has been applied in this work as well.

Another way to avoid retardation losses is to collect the spectra in an aloof setting [97], meaning an electron travels a few nanometers away from the sample. This works due to the delocalization of the low loss signal caused by the long range Coulomb interaction when an electron beam 'feels' the sample not only at the illuminated position but also around it. Delocalization of

¹ By Inductiveload [Public domain], from Wikimedia Commons

Introduction 2. Transmission Electron Microscopy

inelastic signal can be determined as a radius of the scattering probability in real space containing 50% of all inelastically scattered electrons It can be estimated by the formula [79]:

$$L_{50} = 0.5\lambda/\theta_E^{3/4}. \quad (1.59)$$

The aloof signal, however, is weak; the method also requires special sample preparation cutting the sample in a way that the beam can scan close the region of interest without touching it. The main challenge in this case lays in creating a sample edge without altering the sample structure which is extremely difficult to do, especially for multilayered samples.

As a sanity check the spectra obtained by one of the three methods above can be compared with the imaginary part of $1/\varepsilon$ from the optical dielectric function (if known) which approximates, as mentioned before, the loss part of EELS spectra without retardation losses and assuming the dipole approximation holds. Though, it is worth to remember that the shape of the low loss spectra even without retardation losses changes for different collection angles as the momentum transfer deviates from zero.

After obtaining a spectrum free from unwanted losses, the next challenge comes in the interpretation of features in the low loss region as they, in first approximation, represent joint density of states between valence and conduction band (assuming absence of surface plasmon losses). There are a few consequences that should be pointed out:

- The initial and final energy of transition cannot be obtained without some prior-knowledge about the band structure.
- The initial and final points in the Brillouin zone of the transition are unknown as well.
- Only transitions with momentum transfer laying in a certain range are acquired. This range is determined by the convergence and collection angles, Bragg angles and the position of the spectrometer according to the diffraction reflexes. This matter will be explained in more detail in the Chapter 4. For now, one point should be highlighted – in order to obtain good momentum resolution and to acquire only certain features in the band structure microscope should be set to a special operating conditions (e.g. small convergence and collection angles).
- However, in most cases for bulk dielectric or semiconductor materials the direct band gap should be clearly interpretable as it appears as the first spectrum onset after the ZLP.

Core-loss EELS

Above ~ 50 eV EELS spectra contain only losses connected to the excitations of core levels of atoms – ionization edges. The energy of the initial electrons is more than enough to excite all possible transitions from inner shells of an atom. Following an inelastic event the electrons from inner shells are excited to the empty states above Fermi level and primary electrons lose an energy equal to the energy of the excitation from a certain level, travel towards the spectrometer. As it was mentioned before, inelastic scattering happens in a very narrow angular range so almost all inelastic electrons are collected with a collection angle of approximately 100 mrad. The nomenclature of EELS is taken from the standard one used in X-ray absorption and other techniques. Edges are marked with the shell from which transition occurred: *K, L, M, N, O...* Higher levels like *L* or *M* are distinguished in two groups depending from which orbital excitation occurs.

Introduction 2. Transmission Electron Microscopy

For example, L_1 marks the transitions from $2s$ level and $L_{2,3}$ from $2p$. The closer the shell to the nucleus the higher the energy that is required to excite the electron from this shell, also the heavier the atom the stronger it attracts the electrons, therefore for every atom and every orbital the excitation energy is different and can be identified with EELS.

The minimum energy to excite an electron from the inner shell is called the energy onset. The probability to excite the atomic electrons is highest when the energy of the incoming electrons equals this energy onset. If the energy of an incoming electron is higher like in the case of EELS the probability decreases. As a consequence, lower acceleration voltages are generally more advantageous in EELS experiments as the cross-section becomes higher. This also explains the general 'sawtooth' shape of the EELS edges simulated from the atomic model (for example, the Hartree–Slater central-field model [98]), with an intense starting peak at the energy onset and gradual decrease afterwards. However, the shape of the real spectra is approximately a direct visualization of the angular momentum projected local density of unoccupied states broadened by lifetime and microscope.

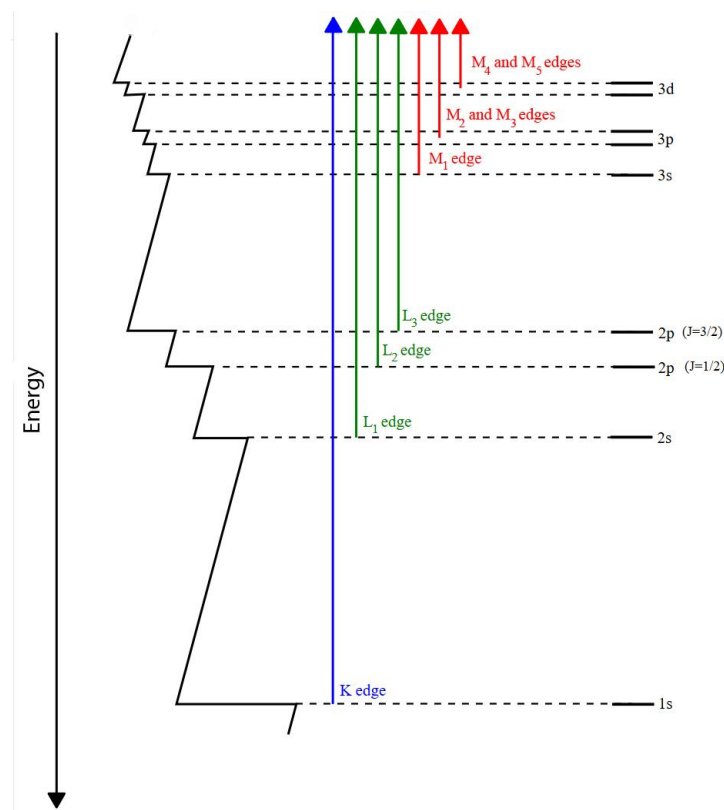


Figure 1.13. Nomenclature of the energy levels in atom corresponding to the EELS edges¹.

¹ Atenderholt at English Wikipedia [CC BY-SA 3.0 (<https://creativecommons.org/licenses/by-sa/3.0>) or GFDL (<http://www.gnu.org/copyleft/fdl.html>)], via Wikimedia Commons.

Introduction 2. Transmission Electron Microscopy

Atoms surrounding a target atom in a solid strongly influences the shape of the edge. A core electron ejected with an energy above 50 eV can be considered as a free electron which spherical wave function elastically interacts in a constructive or destructive way with the reflected waves from the neighboring atoms. This creates oscillations of intensity after the energy onset over the range of several hundred eV if no other edge is present after, forming so-called extended energy-loss fine structure (EXELFS). This fine structure can give information about chemical bonds, and allows to distinguish the same element in different allotropic modifications, determine the coordination of the atom.

The tails of valence and core excitations form the background in EELS spectra. It can commonly be described by an exponential function:

$$B(E) = aE^{-r}, \quad (1.60)$$

If the sample is thick, multiple scattering can occur and the primary electron will go through a few scattering events before leaving the sample. This effect usually results in multiple plasmon excitations but can also influence the background of core-loss spectra due to the electrons which lost their energy to excite, for example, a plasmon excitation and then excited a core state. Multiple scattering can be expressed as a convolution of core-loss spectra $C(E)$ without multiple scattering and $L(E)$ is experimental low loss spectra and taken into account by deconvolving the initial core-loss spectra with this experimental low loss spectrum [99]:

$$S(E) = C(E) * \left[\frac{L(E)}{I_0} \right], \text{ therefore } C(E) = I_0 \mathcal{F}^{-1} \left[\frac{\mathcal{F}(S(E))}{\mathcal{F}(L(E))} \right], \quad (1.61)$$

where $S(E)$ is the experimental core-loss spectra and I_0 is the maximum intensity of ZLP peak. However, this method suffers from the noise amplification. Deconvoluted single scattering spectrum $C(E)$ contains a lot of high frequency components due the fact that the Fourier components of $L(E)$ get smaller for increasing frequencies and the ratio amplifies the high frequency components of $L(E)$ and $S(E)$ creating a lot of noise.

Issues related to the multiple scattering can be solved using a different approach. For many applications, such as quantification, there is no need to calculate the deconvoluted spectrum. Multiple scattering can be taken into account by fitting the experimental core-loss spectrum with the model which describes single scattering convoluted with the low loss spectrum. For example, the experimental spectrum with two edges can be fitted with:

$$S(E) = (aE^{-r} + p_1\sigma_1 + p_2\sigma_2) * L(E). \quad (1.62)$$

The background which can cause artefacts in the model, does not have to be included in the convolution and the fitting model (1.62) becomes:

$$S(E) = f(E) + (p_1\sigma_1 + p_2\sigma_2) * L(E), \quad (1.63)$$

where $f(E)$ is the new model for the background. As long as experimental background decays smoothly finding $f(E)$ should not be difficult. This procedure is implemented in the EELSmodel software [100].

Introduction 2. Transmission Electron Microscopy

Quantification of the core loss edges can be performed by calculating the area below the edge with subtracted background. One exponential function cannot describe the background for the whole EELS spectra, therefore for every edge the background should be subtracted by fitting a sufficient interval of background just right before the edge. The ratio between element a and element b can be expressed as:

$$\frac{N_a}{N_b} = \frac{I_a(\beta, \Delta_a) \sigma_b(\beta, \Delta_b)}{I_b(\beta, \Delta_b) \sigma_a(\beta, \Delta_a)} \quad (1.64)$$

where I is integral under the edge, β is collection angle, Δ is energy interval chosen for integration. The formula (1.64) considers only single scattering, hence multiple scattering effects should be taken into account beforehand. The effects related to multiple scattering can also be partly canceled out if large enough integration intervals are chosen. In EELS model one can use similar expression to obtain the element ratio, but with multiple scattering already taken into account:

$$\frac{N_1}{N_2} = \frac{p_1 \sigma_2(\beta, \Delta_2)}{p_2 \sigma_1(\beta, \Delta_1)} \quad (1.65)$$

When the core-loss intensity is integrated over an energy window Δ that is wide enough to include most of the extended X-ray absorption fine structure (EXAFS), the corresponding cross section $\sigma(\beta, \Delta)$ is little affected by the chemical environment of the excited atom, and can therefore be calculated using an atomic model. Cross-sections for each atom can be calculated by the Hartree-Slater method [79]. Generalized oscillator strengths obtained from these cross-sections, can be parameterized as a function of energy loss and scattering angle. Parametric cross-sections for a wide range of atomic number Z , initial acceleration voltage E_0 and collection angle are calculated from the GOS and implemented, for instance, in the Gatan Digital Micrograph software.

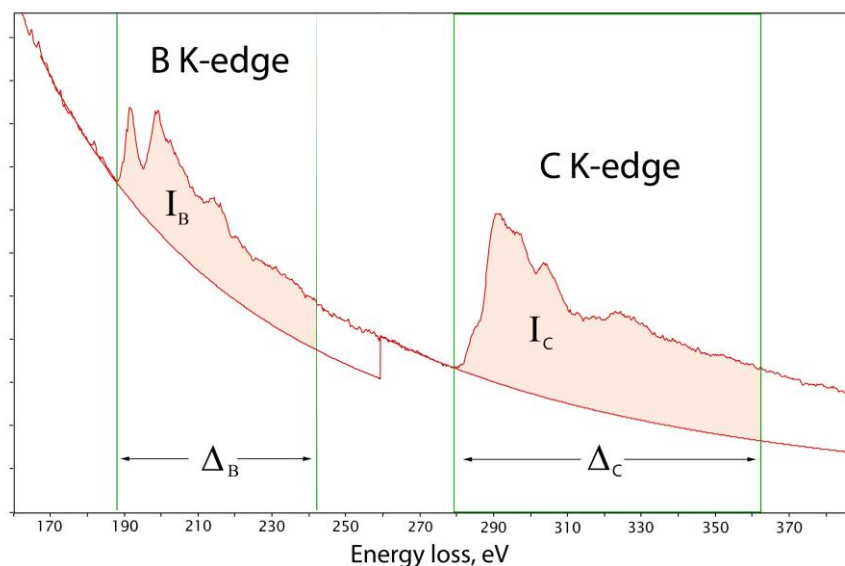


Figure 1.14 . Example of a core-loss EELS spectra with two edges – boron K-edge and carbon K-edge with subtracted background. Signal window approximately shows the Δ for quantification.

Chapter 2. Application of TEM on novel diamond based materials

In this chapter the study of novel diamond based materials synthesized at IMO, Hasselt University, is discussed with focus on the TEM characterization. The first section goes over diamond and boron nitride nanocomposite materials for field emission electron sources. The second part presents the investigation of a CVD diamond layer grown at unusually low temperature. This research resulted in four articles:

- K.J. Sankaran, D.Q. Hoang, S. Kunuku, S. Korneychuk, S. Turner, P. Pobedinskas, S. Drijkoningen, M.K. Van Bael, J. D'Haen, J. Verbeeck, K.C. Leou, I.N. Lin, K. Haenen, Enhanced optoelectronic performances of vertically aligned hexagonal boron nitride nanowalls-nanocrystalline diamond heterostructures, *Sci. Rep.* 6 (2016) 1–11. doi:10.1038/srep29444.
- K.J. Sankaran, D.Q. Hoang, S. Korneychuk, S. Kunuku, J.P. Thomas, P. Pobedinskas, S. Drijkoningen, M.K. Van Bael, J. D'Haen, J. Verbeeck, K.-C. Leou, K.T. Leung, I.-N. Lin, K. Haenen, Hierarchical hexagonal boron nitride nanowall–diamond nanorod heterostructures with enhanced optoelectronic performance, *RSC Adv.* 6 (2016) 90338–90346. doi:10.1039/C6RA19596B.
- D.Q. Hoang, S. Korneychuk, K.J. Sankaran, P. Pobedinskas, S. Drijkoningen, S. Turner, M.K. Van Bael, J. Verbeeck, S.S. Nicley, K. Haenen, Direct nucleation of hexagonal boron nitride on diamond: Crystalline properties of hBN nanowalls, *Acta Mater.* 127 (2017) 17–24. doi:10.1016/j.actamat.2017.01.002.
- S. Drijkoningen, P. Pobedinskas, S. Korneychuk, A. Momot, Y. Balasubramaniam, M.K. Van Bael, S. Turner, J. Verbeeck, M. Nesládek, K. Haenen, On the Origin of Diamond Plates Deposited at Low Temperature, *Cryst. Growth Des.* 17 (2017) 4306–4314. doi:10.1021/acs.cgd.7b00623.

Diamond based materials for field emission electron sources

Field emission electron sources (cathodes) find their application not only as electron guns in microscopes but can also be used, for example, in microwave amplifiers, e-beam induced (X-ray) light sources, flat panel displays and travelling wave tubes [1 101]. Finding the right material for such sources is not a trivial task as it should meet a number of conditions, such as low turn-on electrical field [2], high current density and long life-time stability. The first requirement can be achieved by using materials with low or even negative electron affinity³ such as, for instance, aluminum nitride, hexagonal boron nitride [102] and diamond [103]. However, in many cases the use of such bulk materials is not advantageous due to their bad mechanical properties or complications with their integration into the current technology. A silicon substrate, widely used in semiconductor devices, can serve as an essential electron supply to a thin coating of material with a low electron affinity. A device which combines an easily handled substrate with a material suitable for field emission, has many advantages compared to a single bulk material. However, this combined material approach brings several new challenges in fabricating good performance composite nanomaterials with good durability suitable for real applications. All parts or layers of this device participate in electron emission process starting from the substrate which should provide a sufficient electron supply towards the high density individual emitting sites on the top, and therefore, besides the good quality of emitting material itself, the interface is also very important as it can compromise the electron transport due to the, for instance, bad conductivity.

Table 2.1. Comparison of various materials proposed as field emission sources.

Material	Turn-on field, V/m•10 ⁻⁶	Field enhancement factor, β	Life-time stability, min
Carbon nanotubes ¹⁰⁴	1.4	4350	33
Boron nitride nanotubes ¹⁰⁵	32.5	98	-
AlN nanocones ¹⁰⁶	4.8	1561	-
MoO ₃ nanobelts ¹⁰⁷	8.7	-	120
Hexagonal BN-NCD-Si ⁵¹	15.2	3057	248
Hexagonal BN-Si ⁵¹	35.5	560	27
In ₂ O ₃ -Ga ₂ O ₃ heterostructures ¹⁰⁸	6.45	4002	-
LaNiO ₃ -ZnO nanorod arrays ¹⁰⁹	8.6	673	-
ZnO-WO _x hierarchical nanowires ¹¹⁰	3.6	2490	-
Hexagonal BN-diamond nanorods-Si ¹¹¹	6.0	5970	> 435 > 132 (in Ar ⁺ plasma)

¹ Specialized tubes used to amplify radio frequency (RF) signals in the microwave range by absorbing power from an electron source.

² The minimum external electrical field at which electron emission current density of the material reaches 0.1 A/m². Different approach to determine it can be taken by calculating the intersection of straight lines extrapolated from the high-field and low-field segments of Fowler-Nordheim plots.

³ Electron affinity is defined here in terms of the solid state physics and denotes an energy obtained by moving an electron from vacuum just outside the semiconductor to the bottom of the conduction band just inside the semiconductor.

Chapter 2. Application of TEM on novel diamond based materials

Ideally, the emitting material should also deliver high and stable field-emission currents overtime which is quite difficult to achieve. For instance, carbon nanotubes are not suitable to get either high emission current or stable electron emission at a high emission current [112,113].

In the IMO lab at Hasselt University, a range of new materials for field emission has been recently developed. They are based on diamond and/or hexagonal boron nitride grown on top of a Si substrate. TEM helped to characterize these materials and to reveal the factors influencing their performance. The first synthesized material [51] is a multilayered structure consisting of a Si substrate, an intermediate nanocrystalline diamond layer (NCD) and a top layer of hexagonal boron nitride. The NCD layer was grown on mirror polished (100)-oriented silicon (Si) wafers using an ASTeX 6500 series MPECVD reactor described in the introduction chapter. Nanodiamond seeds were homogeneously distributed over the substrate before the deposition.

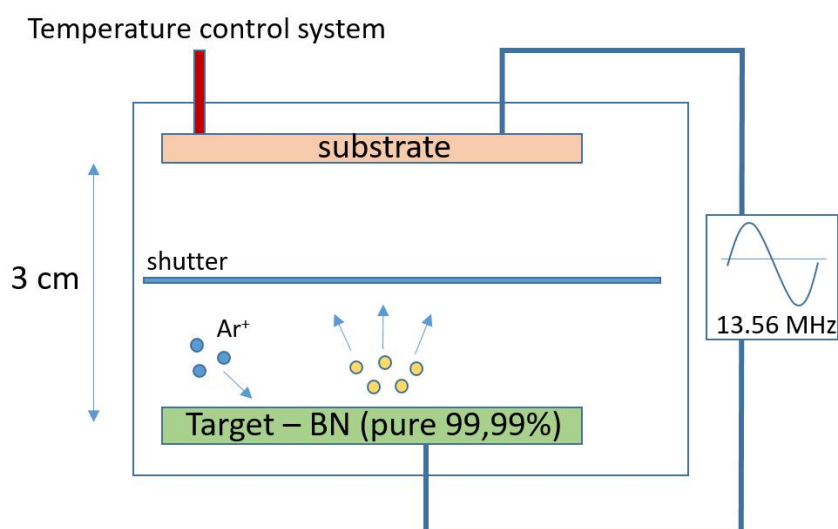


Fig.2.1. Scheme of a radio-frequency sputtering technique. The target was made from the 3 inch-diameter pyrolytic BN ceramic plate with 99.99% purity and separated from a substrate by 3 cm. The pressure in the chamber was kept at 2.1×10^{-2} mbar and the optimal fabrication gas mixture was chosen as Ar(51%)/N₂(44%)/H₂(5%) with the cathode power of 75 W.

In the second step, hexagonal BN nanowalls were grown on the NCD films by a home-built unbalanced 13.56 MHz radio frequency (RF) sputtering technique. In this technique a voltage high enough to ignite the Ar plasma in the chamber of the reactor, is applied between a cathode (target) and an anode (substrate) separated by a few centimeters. Argon ions bombard the surface of the target leading to the sputtering off the target material in a fine spray. A fraction of the ions from the target is getting deposited on the substrate during this process. If the target is made from a non-conductive material, than after some time the surface of the target builds up positive charge, making it unfeasible for further bombardment. Alternating RF potential can assist in removing the charge by creating the oscillations of the electrons in the alternating field which maintain the constant discharge of the target. During the positive half-cycle the electrons reach the surface of the target and remove the charge, during the negative - ions bombardment continues, and the sputtering of the target material happens.

Chapter 2. Application of TEM on novel diamond based materials

This material demonstrates good emission properties and long life-time outperforming many other materials suggested as field emission sources (table 2.1). For comparison, hexagonal boron nitride was also deposited on the Si substrate right away, without NCD interlayer. Prior to the BN deposition Si substrate was cleaned by the standard RCA procedure [114] but without the optional stage of removing the native silicon oxide SiO_x layer of about 2 nm. This structure shows much worse field emission properties than the one with the intermediate diamond layer (table 2.1): it exhibits a higher turn-on field, shorter stability and lower field enhancement factor β [115] which was estimated as $\beta = -6.8 \cdot 10^3 \phi^{3/2} / m$, where m is the slope of the Fowler-Nordheim curves plotted as $\log (J_e/E^2)$ versus $(1/E)$ where J_e is the emission current and E the applied field, and $\phi = 6.0 \text{ eV}$ [116] is a work function for hexagonal BN. Fowler-Nordheim theory [117] describes the field emission process when in the presence of an applied electric field, electrons tunnel through a barrier, such as a thin dielectric layer between p-n- junction in a semiconductor device or, like in this case, a surface of a semiconductor.

TEM, ADF-STEM and BF-STEM imaging helped to understand the reason behind such difference in field emission performance. The imaging was performed either making use of probe-corrected FEI Titan³ TEM or of the Jeol JEM 3000F both operating at beam energies of 300 keV. The interpretation of the figure 2.1 suggests that the growing process of the BN on top of the Si first went through an amorphous and turbostratic stages of BN growth which agrees with the observations from the literature [118]. In a turbostratic phase of BN (tBN) the layers are arranged in a haphazard manner. This phase reveals some crystallinity through the visible (002) basal planes which are randomly oriented with respect to the substrate (figure 2.1). This phase provides nucleation sites for the hexagonal BN (hBN) nanowalls where the basal planes are aligned almost perpendicular to the substrate surface.

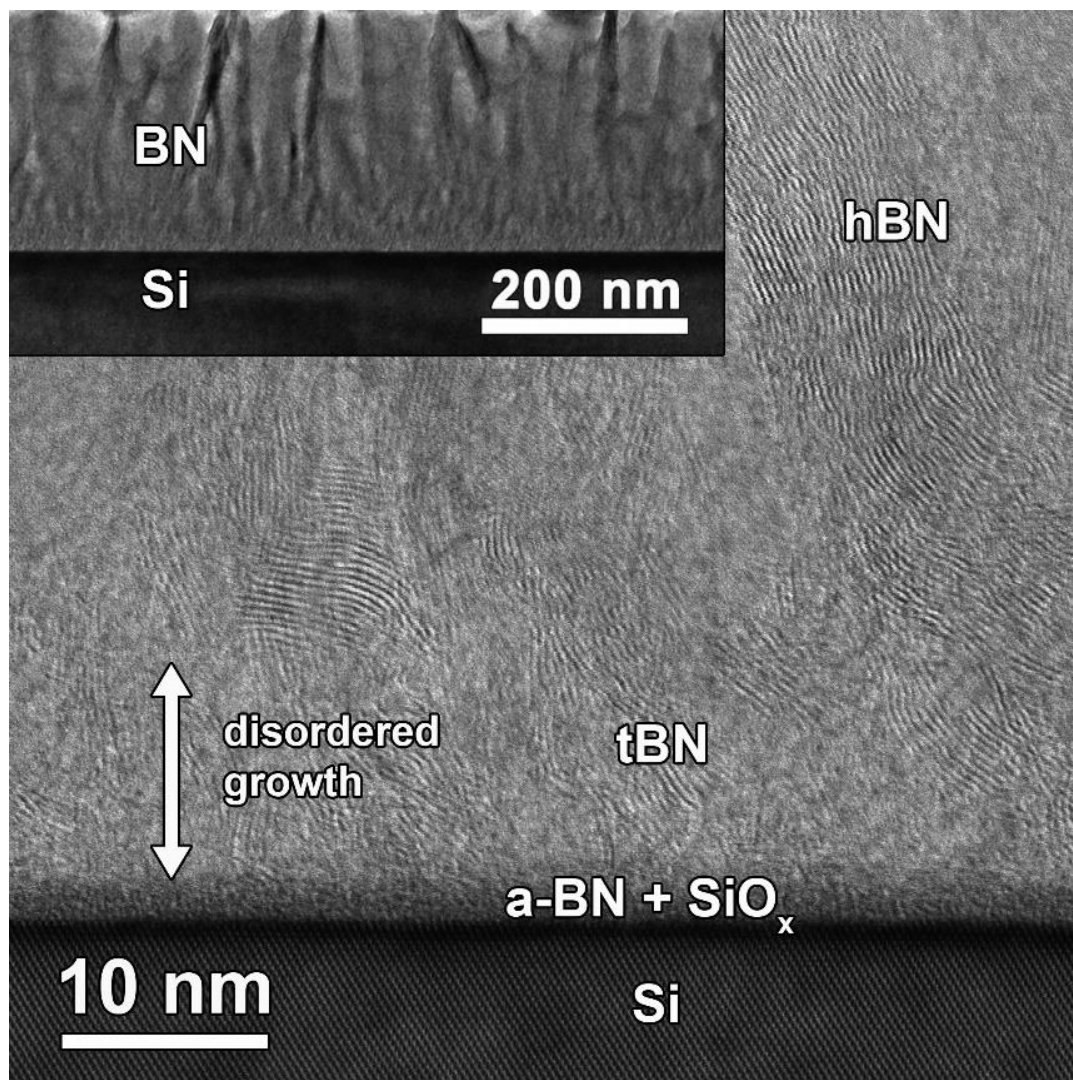


Figure 2.1. High resolution BF-TEM image of the BN nanowalls grown on top of the Si substrate by RF sputtering process. a-BN states for amorphous BN and tBN for turbostratic stage of BN growth. Image is obtained on a JEOL JEM-3000F operating at 300 kV.

On the other hand, BN nanowalls deposited on the diamond interlayer grow mostly in an arranged way with (002) planes aligned perpendicular to the surface of the NCD layer. As mentioned above, the adequate electron supply from the Si substrate towards emitting sites (hBN) is crucial for a good field emitter. Non-optimal resistivity of the amorphous or turbostratic boron nitride can compromise the electron supply. The absence of this phase can be the cause to the superior properties of the structure with the intermediate diamond layer (figure 2.2). The direct growth of hexagonal BN on the diamond surface lowers the resistivity of the interfacial layer and therefore, assists in electron transport towards the tips of the BN nanowalls where field emission can take place.

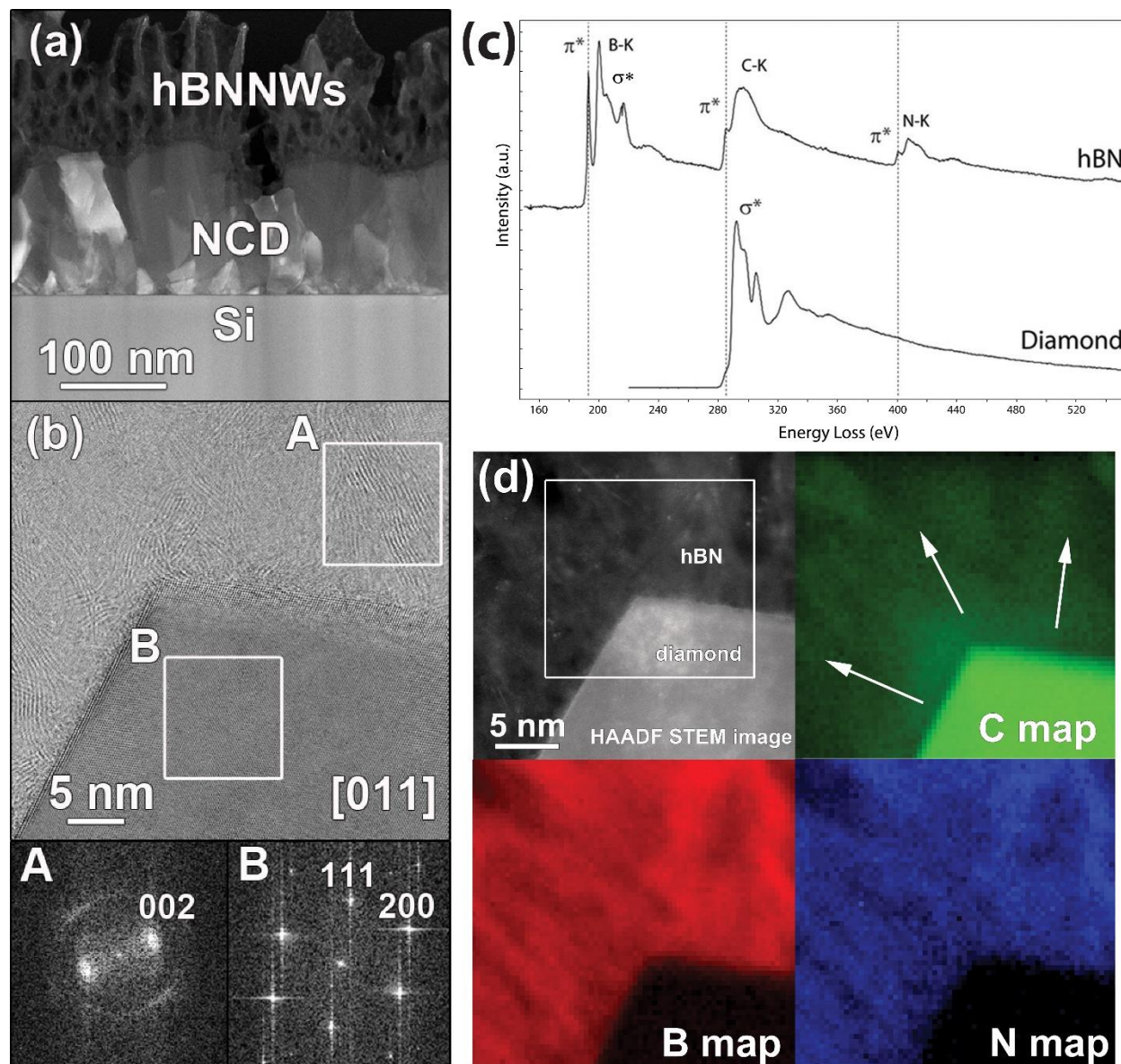


Figure 2.2. (a) Overview ADF-STEM image of the NCD-hexagonal BN structure grown on a Si substrate. (b) High resolution BF-STEM image showing the interface between a diamond grain and hexagonal BN nanowalls with diffractogram insets taken at the regions A (hexagonal BN) and B (diamond grain). (c) EELS spectra extracted from the hexagonal BN (top) and diamond grain (bottom). (d) EELS maps showing the distribution of carbon, boron and nitrogen.

A possible mechanism for the hexagonal BN nucleation on the diamond surface has been suggested in the following work by D.Q. Hoang *et al.* [119]. As mentioned above, no sign of disordered growth of the BN on top of the NCD layer was observed. The proposed mechanism for the BN nucleation which is quite similar to the diamond CVD growth, can shed light on this matter. As a result of the CVD process (see first chapter), the NCD surface is terminated with hydrogen to prevent cross-linking and to stabilize the sp^3 nature of the carbon bonds during diamond growth.

Hydrogen is also present during the physical vapor deposition process of BN. Radicals of boron can substitute the hydrogen atoms dangling at the surface of the NCD and this way create a nucleation site for the BN ring. Two nitrogen radicals can further attach to the boron followed by another two boron radicals and the last nitrogen to finalize a ring structure (figure 2.3). The vertical orientation of the BN nanowalls in accordance to the surface of NCD grains can, therefore, also be explained by the orientation of this first boron atom. During further growth, all BN nanowalls start to elongate perpendicular to the substrate despite originating from different diamond facets which are not parallel to the Si substrate. This suggests that the direction of the incoming ion flux which is mostly directional toward substrate, also has an effect on the BN orientation.

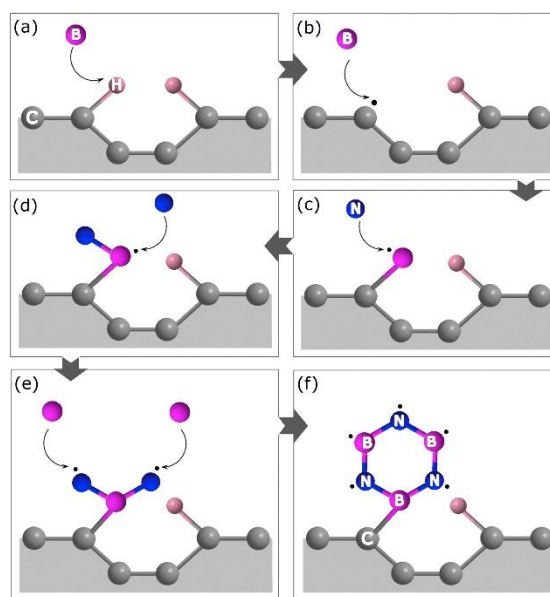


Figure 2.3. Sketch of the proposed nucleation mechanism of the hexagonal BN nanowalls on the diamond surface [119].

STEM-EELS mapping was carried out using conventional settings for core-loss acquisition with a convergence angle of 20 mrad, a collection angle of 36 mrad an acceleration voltage of 300 kV at an FEI Titan³ equipped with a Gatan Enfium Spectrometer for EELS. The shape of the B K-edge is typical for a well-crystallized hexagonal boron nitride [120,121] with a pronounced π^* -peak laying at 189 eV followed by a σ^* -peak. The C K-edge spectrum extracted from the diamond grain correlates well with the σ^* -peak of diamond, and indicates sp^3 -hybridized carbon. Fitting to a linear combination of reference spectra also reveals the presence of a sp^2 -coordinated amorphous carbon phase characterized by a π^* -peak at 285 eV and with a featureless σ^* -peak [122]. This phase spreads from the surface of the diamond grain towards the BN nanowalls. The presence of amorphous carbon at the interface region is possibly induced by carbon incorporation and dynamic recoil ion mixing in an early stage of boron nitride deposition. This phase, possibly, assists in the electron transport towards emitting sites by providing better conductivity.

The electron field emission properties of the successful combination of diamond/hexagonal BN can be further increased by modifying the shape in order to provide higher aspect ratio. 1D materials such as carbon nanotubes, GaN, Si, SiC, NiSi, ZnO, ZnS, CdS, graphene and AlN [123] have shown potential for electron emission due to their high aspect ratios. Nevertheless, in some cases, 1D structures are not sharp enough to produce high local electrical fields. On the other hand, stacks of sheets of 2D materials with many sharp edges can also exhibit strong local electrical fields. Researchers in Hasselt University attempted to combine the advantages of 1D materials represented as an array of diamond nanorods with their high aspect ratio and 2D like hexagonal BN walls deposited on the surface of the nanorods in order to provide high local electrical fields [111].

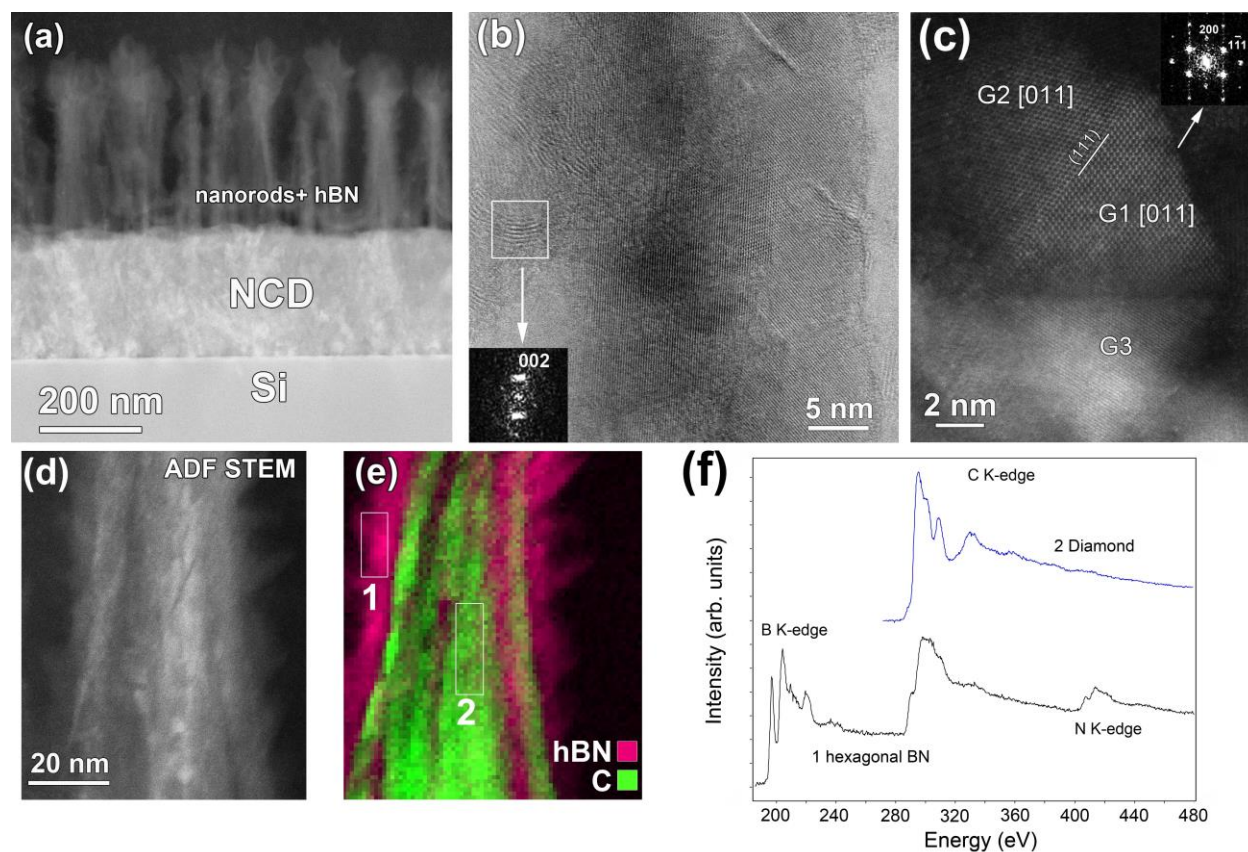


Figure 2.4. (a) Overview ADF-STEM image of the structure consisting of diamond nanorods covered with hexagonal BN on top of the NCD diamond layer grown on the Si substrate. (b) High resolution BF-STEM image of the nanorod with hexagonal BN nanowalls grown on its surface. (c) High resolution ADF-STEM image of the nanorod consisting of nanometer sized diamond grains. (d) ADF-STEM image of the area for STEM-EELS mapping. (e) STEM-EELS map showing the distribution of hexagonal BN and carbon phases. (f) EELS spectra extracted from regions 1 (hexagonal BN) and 2 (diamond) marked at (e).

This structure was synthesized in a multistage process. Firstly, an NCD layer was deposited on a Si substrate in the same manner as for the previous sample. Then the as-grown NCD layer was immersed in a pseudo-stable suspension of nanodiamond particles of approximately 8-10 nm in

size in deionized water and sonicated for 10 min to seed the particles on the NCD surface and to further serve as a mask for a reactive ion etching (RIE) process. After masking, the NCD was etched using the RIE process in O₂ gas at an RF power of 200 W for 30 min. Finally, hexagonal BN was deposited on the diamond nanorods by a home-built unbalanced 13.56 MHz radio frequency (RF) sputtering technique.

The obtained material demonstrates great electron field emission properties: a low turn-on field, high field enhancement factor β and long life-time stability (table 2.1), even in the harsh Ar⁺ plasma environment (the intensity of the plasma initiated by the field electron emission, was stable over 139 min). Overview ADF-STEM image shows that nanorods are completely covered in BN flakes. A closer look at the high resolution images clearly indicates that the hexagonal BN starts to grow directly on the surface of the diamond nanorods without passing through intermediate stages of amorphous or turbostratic growth. The images also reveal the multigrained structure of the nanorods consisting randomly oriented diamond grains with the size about 5-30 nm.

According to the STEM-EELS mapping results, the hexagonal BN phase homogeneously distributes around the nanorods forming nanowalls almost perpendicular to the surface of the rods. The spectrum extracted from these nanowalls is typical for a highly crystallized hexagonal BN phase with the B K-edge typical for sp²-coordinated BN. The carbon K-edge spectrum extracted from the nanorods has a σ^* -peak typical for sp³-hybridized carbon in diamond with a small π^* -prepeak at 285 eV indicating the presence of some sp²- hybridized carbon. It's important to note that this peak is more pronounced than in the case of the continuous NCD layer. Like in the previous structure, the sp²-coordinated carbon is also detected in the hexagonal BN nanowalls. X-ray photoelectron spectroscopy (XPS) and Fourier-transform infrared spectroscopy (FTIR) data confirmed the presence of the B-N, B-C and C-N bonds. This may suggest that, the deposition process of the BN can introduce this carbon rich phase in the nanorods in the same way as for the first structure. Besides the higher aspect ratio, one of the possible explanations to the improved electron field emission characteristics of this material compared to the standard layer by layer structure can lay, presumably, in the presence of the amorphous carbon phase in the grain boundaries of the rods which conducts electrons to the BN flakes more efficiently than diamond.

Diamond plates deposited at low temperature

The recently developed method of linear antenna MPECVD (see chapter 1) has offered the opportunity to grow diamond layers at much lower temperatures than with standard MPECVD. A diamond layer with an unusual plate-like morphology has been synthesized by the research group at the University of Hasselt [124] using spectacularly low deposition temperatures in the range of 320 °C – 410 °C despite previous reports claiming the need for the temperatures above 850 °C [125,126]. The obtained diamond layer demonstrates good crystallinity and very low amount of amorphous carbon. The peculiar morphology which was never observed before for the linear antenna deposition method, and the composition of the layer was characterized by STEM, EDX and EELS technique

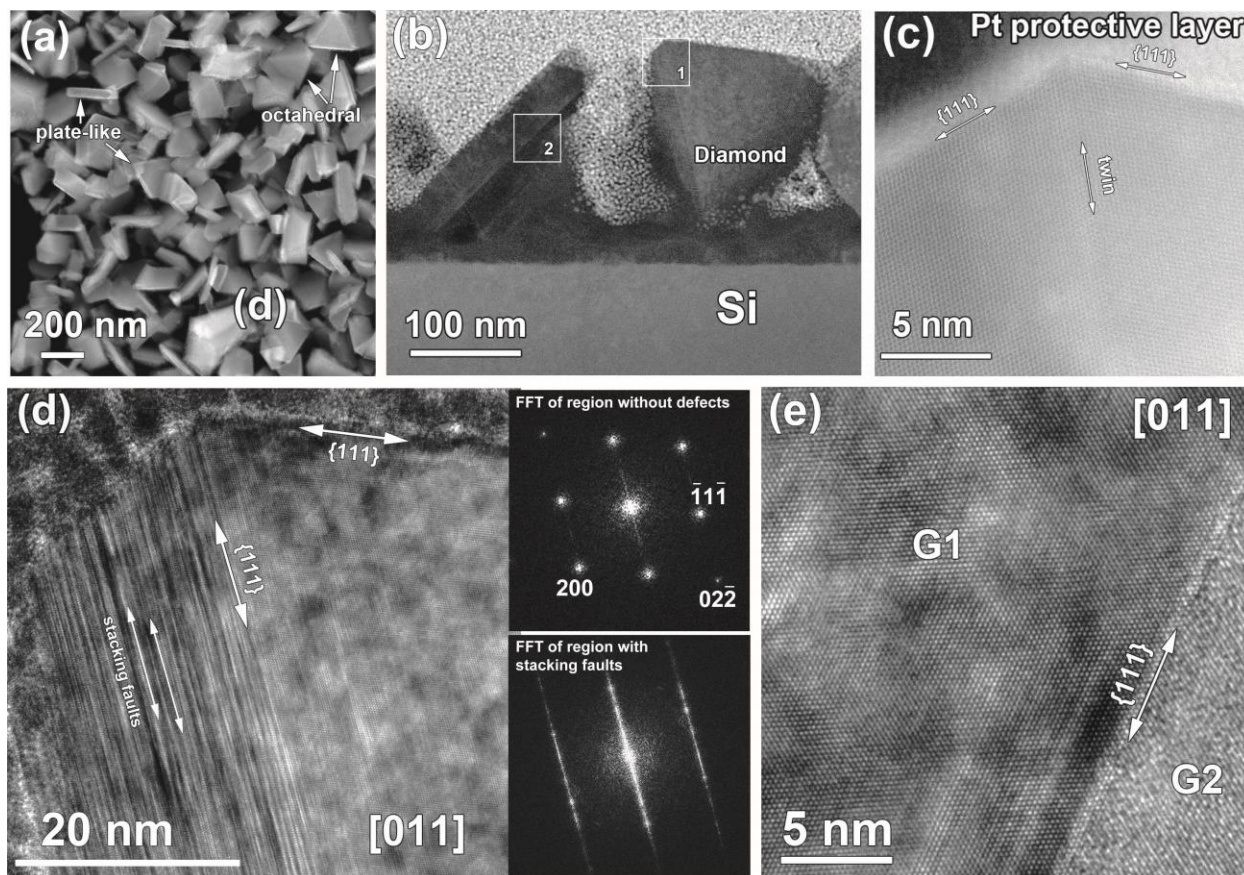


Figure 2.5. (a) Overview ADF-STEM image of the plan-view TEM lamella prepared from a diamond layer grown with the linear antenna MPECVD method indicating plate-like and octahedral grains. (b) Overview ADF-STEM image of a cross-section view TEM lamella. (c) High resolution ADF-STEM image of the edge of the grain terminated with $\{111\}$ planes and separated by a twin crystalline defect. (d) High resolution BF TEM image of region 1 marked in (b) demonstrating the edge of the grain. Insets show diffractograms of the region without defects (top) and the region with stacking faults (bottom). (e) High resolution BF TEM image of the region 2 marked in (b) showing a grain boundary.

In agreement with what was observed with scanning electron microscopy (SEM), ADF-STEM images of the plane-view TEM lamella prepared from the diamond layer show randomly oriented diamond grains consisting of two morphologies: plate-like and octahedral (figure 2.5 b). Plate-like grains have a high length to thickness; their thickness is generally quite uniform along the grain. Octahedral and plate-like morphology of the particles visualized with SEM and TEM together with $\langle 111 \rangle$ edges of the particles observed with high resolution (S)TEM allow to suggest that the diamond grains are mostly terminated by $\{111\}$ facets (figure 2.5). They also can contain $\{111\}$ twin boundaries (figure 2.5 c). Overview ADF-STEM images of the plan-view and cross-section TEM lamellas show that the nanocrystalline diamond layer is relatively porous after 18 hours of growth, however it evolves into a dense NCD layer after 64 hours. As can be seen from the BF TEM image (figure 2.5 e), the neighboring grains are connected by $\{111\}$ planes with a sharp grain boundary,

an evidence of the good crystallinity of the film. An image taken at the edge of another grain (figure 2.6 d) exposes a high amount of stacking faults which create typical lines in the Fast Fourier transform (FFT) of this region. Stacking faults alternate the stacking sequence in atomic layers in diamond creating, instead of the cubic close packing ABCABC, a hexagonal close packing ABAB. Sometimes, such hexagonal packing in diamond is referred as a new phase – lonsdaleite [127]. However, the discussion of whether the new hexagonal phase really exists or the cubic diamond crystal can be considered highly defective, is still ongoing [128]. A diffractogram taken at the region without defects is representative for a cubic diamond crystal in [011] orientation.

EDX analysis carried out on a large area of the plan-view sample, revealed the presence of Si at the edges of the diamond grains (figure 2.6). To determine the source of Si, another sample was grown by the same method but on a molybdenum substrate. Si was again detected in this sample, therefore, the most probable source of this impurity is the quartz tubes used in the CVD chamber. An EELS analysis was carried out to determine the quality of the diamond film and proved its high crystallinity. The carbon K-edge spectra (figure 2.7) contain typical features for sp^3 -coordinated carbon in diamond with a very low amount of sp^2 -hybridized bonds, distributed mostly at the grain boundaries.

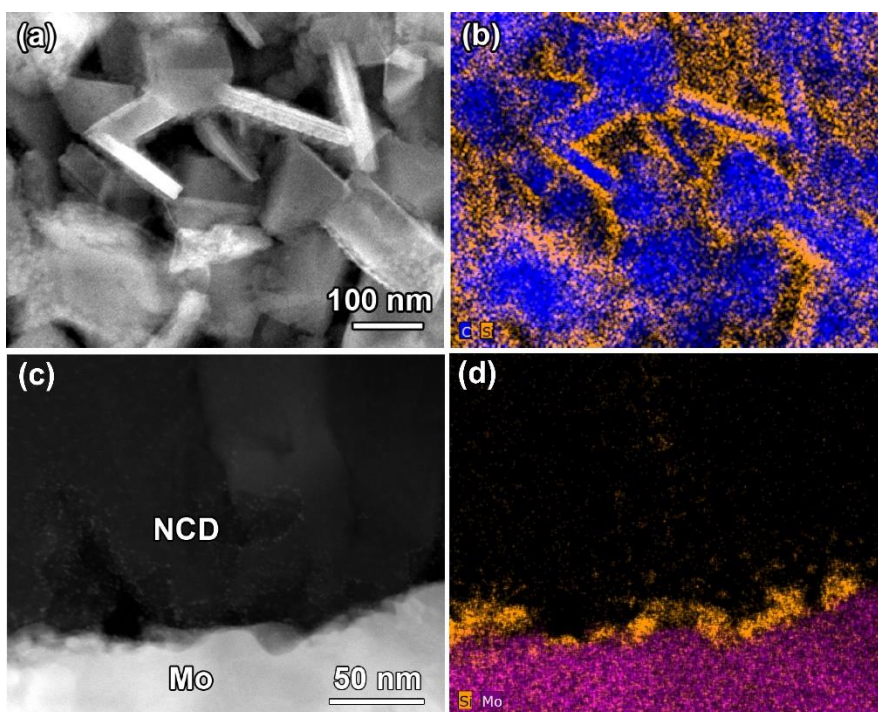


Figure 2.6. (a) HAADF image of a plan-view sample prepared from the NCD layer which was deposited on a Si substrate. (b) EDX map of (a) (blue: carbon and yellow: silicon) showing the presence of silicon on the diamond grains. (c) HAADF image of a cross-section sample prepared from the NCD layer deposited on a Mo substrate. (d) EDX map showing the distribution of Si (yellow) on Mo (purple) from the substrate.

Stacking faults which appear at the start of the growing process can be the cause for anisotropic plate-like morphology, since they create self-perpetuating growth steps. According to

the literature [129], two or more stacking faults can lead to the formation of hexagonal plates. However, the exact mechanism of development of the stacking faults is still unclear. The hexagonal shape can also be obtained due to the faster relative growth rate of the {100} planes with respect to the slower growth rate of the {111} planes [130]. Based on literature reports and observations on the current sample, three mechanisms for the plate-like morphology were proposed by the Hasselt group:

1) First one starts from the early stages of the nucleation process involving the impurities such as Si which can come from the quartz tubes in the CVD chamber or Al, the material used in the walls of the CVD chamber. Impurity atoms can serve as a nucleation sites for fullerene particles [130] which, due to their hexagonal structure, induce the formation of the hexagonal stacking in diamond instead of cubic and cause the formation of the stacking faults. Once formed, a stacking fault keeps growing and regenerating itself.

2) The selective blocking of growth of one of the planes with respect to others by the capping layer formed by impurity, was suggested as the second proposed mechanism. The {111} plane is more reactive at lower temperatures than {100} and more likely to be bonded with the Si atoms.

3) The third suggested mechanism initiates from the impurity-enhanced etching of the {111} planes compared to the {100} planes due to the higher surface energy of the {111} plane. One of the possible ways of etching can be described by the beta-scission reaction where firstly, a SiH₃ radical bonded to the carbon at the diamond surface, loses a hydrogen by reacting with the atomic hydrogen, and secondly, the methylenesilane molecule could be released into the plasma leaving a radical at the diamond surface [131].

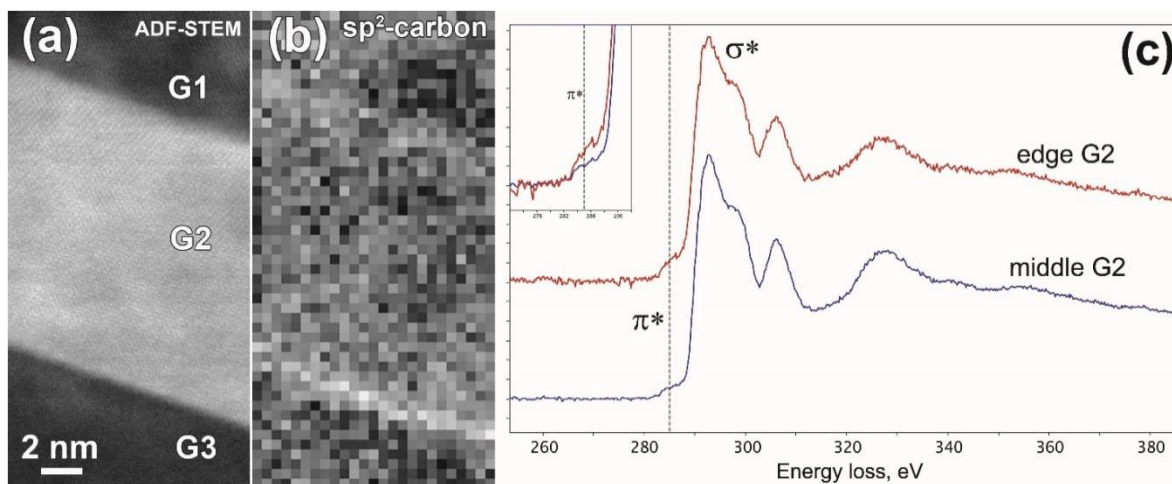


Figure 2.7. STEM-EELS mapping of the diamond plate-like grain. (a) ADF-STEM image of the area chosen for the EELS mapping showing the interface between three grains: G1, G2 and G3. (b) STEM-EELS map showing the distribution of sp²-carbon phase. (c) EELS spectra extracted from the edge (top) and the middle (bottom) of the grain G2 showing the slight amorphization of the grain.

Conclusions

1) Novel combination of the hexagonal boron nitride nanowalls grown on top of the nanocrystalline diamond layer suggested for large field emitting devices, was investigated by means of STEM and EELS. The enhanced field emitting properties of this material compared to the one where BN was grown directly on the Si substrate, were explained by direct formation of the hexagonal BN on the diamond surface without going through the turbostratic stage making the electron transport from the Si substrate towards the emitting sites on the BN nanowalls easier. The field emitting properties of this successful combination were improved even more by fabricating a material with higher aspect ratio - an array of diamond nanorods covered with boron nitride. The STEM and EELS studies of this material revealed that the hexagonal BN phase like in the previous case, grows directly on the surface of the diamond nanorods.

2) Nanocrystalline diamond layer obtained by linear antenna MPECVD method at low deposition temperatures (320 - 410 °C), was studied by the means of TEM. High resolution STEM and EELS investigations revealed the good crystallinity of the diamond layer despite the low temperatures of the synthesis. Unusual plate-like morphology observed before only for the high temperature synthesis, was studied by means of STEM and three possible mechanisms of its formation were suggested.

Chapter 3. Direct visualisation of the platelet structure in natural Ia diamonds by STEM and EELS

In this chapter we discuss the structure of the platelet defect in natural diamond determined with the help of state-of-the-art imaging techniques in STEM and novel image processing algorithms. This defect is present in 98% of all natural diamonds but its structure has remained a mystery for almost half a century. This research was presented at two conferences:

- Hasselt Diamond Workshop, SBDD XXI.
Poster presentation: 'Direct visualisation of the nitrogen platelet structure in natural Ia diamonds by ADF-STEM'. Svetlana Korneychuk, Stuart Turner, Artem Abakumov, Alexey Bosak, Jo Verbeeck. Hasselt, Belgium, March 9-11, 2016.
- The 16th European Microscopy Congress EMC 2016.
Poster presentation: 'Determination of the platelet structure in natural diamond by ADF-STEM'. Svetlana Korneychuk, Stuart Turner, Artem Abakumov, Alexey Bosak, Jo Verbeeck. Lyon, France, 28 August - 2 September 2016.

Overview of the platelet research

As mentioned in the introduction chapter, natural diamonds contain various intrinsic and extrinsic defects, including carbon interstitials, colour centres, dislocations, platelets and voidites²⁴. One of the most common defects present in the majority of natural diamonds is a semi-planar structure called a *platelet* which forms only in nitrogen-rich *Ia* type of diamond. This suggests that only certain combination of parameters in the Earth's Mantle, such as pressure, temperature and time can lead to the formation of this defect. Understanding of the platelet structure can shed light on the geological processes behind it. Various studies of the platelet [34,132-136] throughout the long history of diamond research did not completely clarify the structure of this defect.

Platelets were first visualized by means of TEM in the 1960s [132]. They are semi-planar structures widely present in *Ia* natural diamonds [24] with irregular ellipsoidal shape randomly oriented along $\langle 100 \rangle$ planes. *Ia* diamond is rich with aggregated forms of nitrogen, mostly A centres [137] formed by two nitrogen atoms and B centres [138] which consist of four neighbouring N atoms around the vacancy.

Nearly at the beginning of the platelet discovery nitrogen aggregation was considered as a main mechanism of the platelet formation [139]. Nevertheless, following research confronted this presumption. Nitrogen concentration in the platelet detected by EELS in the 1980s barely reached 4 % [32,33] which is not sufficient to be the only substitutional element. The following research showed that platelets can also be produced artificially by annealing *IaA* diamond [140,141] leading to the aggregation of A centres into B centres and platelets. The measured concentration of N in the platelets varies in the literature and depends on the geological origin of the gemstone.

Nowadays, one of the currently accepted models of a platelet proposed first by Humble [142] and then extended by Fallon *et al.* [33] is as an array of carbon interstitials with or without nitrogen inclusions. In the following works by Goss *et al.* [34,143] many possible platelet models are outlined. The recent work by Bosak *et al.* [135] proposes the lattice periodicity of the platelet defect from diffuse scattering intensities. The last work from 2018 on platelets [72] suggests a structure similar to the one which was reported by us in 2016 [144]. Remarkably, platelet-like structures are also found in Ge [27] and Si [145].

In this chapter we show how TEM which is well known for its capability to directly determine the structure of materials down to the atomic scale and one of the preferred techniques for the study of defects and localised structures, helped us to solve this puzzle. A couple of decades ago, while the interest for this defect was increasing, one of the limiting factors to visualize the platelet was the spatial resolution of TEM. Nowadays aberration-corrected microscopes [146] allow to resolve the atomic structures with 0.5-0.7Å resolution and can give fresh insights to this heavily studied object.

Visualisation of the platelet

Platelets are randomly distributed throughout the diamond crystal along $\langle 100 \rangle$ crystallographic planes. These defects create strain in the crystal giving rise to diffraction contrast in ADF STEM images (fig.3.1). Viewed in [001] or [011] orientation, platelets appear as bright regions with irregular ellipsoidal shape or, in another projection, as short bright stripes with a

length of 5-50 nm (fig.3.1), though platelets with dimension of more than 1 μm have been reported [133].

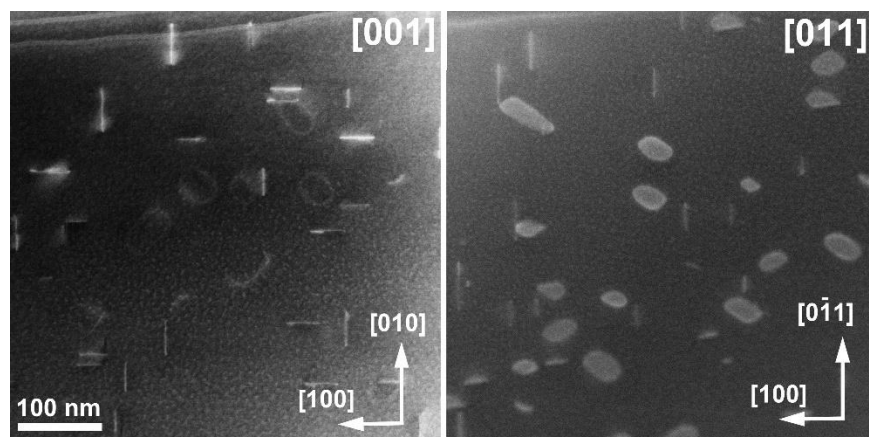


Fig.3.1. Overview ADF-STEM images of the platelets observed in [001] and [011] orientations of a Ia natural diamond crystal.

In order to investigate this platelets more deeply, a few TEM lamellas were prepared by standard focused ion beam (FIB) milling procedure from different parts of the Ia natural diamond of unknown geological origin. The atomic structure of the platelet was studied by high resolution ADF-STEM imaging. The imaging was carried out on the FEI Titan³ transmission electron microscope operated at 300 keV equipped with a probe aberration corrector. This acceleration voltage was chosen in order to get the best possible spatial resolution required for small interatomic distances of diamond. A convergence angle α of 21 mrad and a collection angle of the annular detector of 25-60 mrad were used. The obtained transferred information estimated from diffractograms (figure 3.3) is with 0.7 \AA slightly better than the nominal resolution of the probe corrected Titan microscope – in STEM at 300 keV.

Examination of more than 50 platelets revealed only two atomic configurations – one with an evident glide plane along the defect and the second with a mirror plane. A few examples are presented in figure 3.2. Due to the small interatomic distances of diamond and weak scattering, the structure in the middle of the platelet is challenging to visualize, especially for the configuration with glide plane symmetry. Despite good stability of diamond under the electron beam, the defect also showed a tendency to damage after a few scans with the electron dose of about $10^6 \text{ e}^-/\text{\AA}^2$ which is standard for beam stable inorganic materials in high resolution STEM mode [147].

In order to find the best way to visualize the platelet, we tested a few imaging techniques. One of the ways to get better signal to noise ratio and correct for scanning artefacts is to acquire a stack of images with fast dwell time and then obtain the total image by combining them. Collected images were processed in a few steps: firstly, they were aligned, corrected for the scanning distortions and then summed up into the final image making use of the Smart Align software [78]. Two different regimes were tested: with higher (figure 3.2a) and lower (figure 3.2b) electron doses per frame: $1.7 \cdot 10^5 \text{ e}^-/\text{\AA}^2$ and $8.2 \cdot 10^4 \text{ e}^-/\text{\AA}^2$. The dose was calculated with the assumption that the current value was equal to 50 pA. Due to the difficulty of estimating the real current value, the given numbers for the dose should be considered as approximate but valid for the relative comparison

between each other. In case of higher dose, the number of frames was limited to 10 due to sample contamination and damage. The use of slightly lower dose allowed to increase the number of frames to 25 without destroying the platelet. The stack of images acquired even with lower dose could not be reconstructed in the software due to the very low signal to noise ratio.

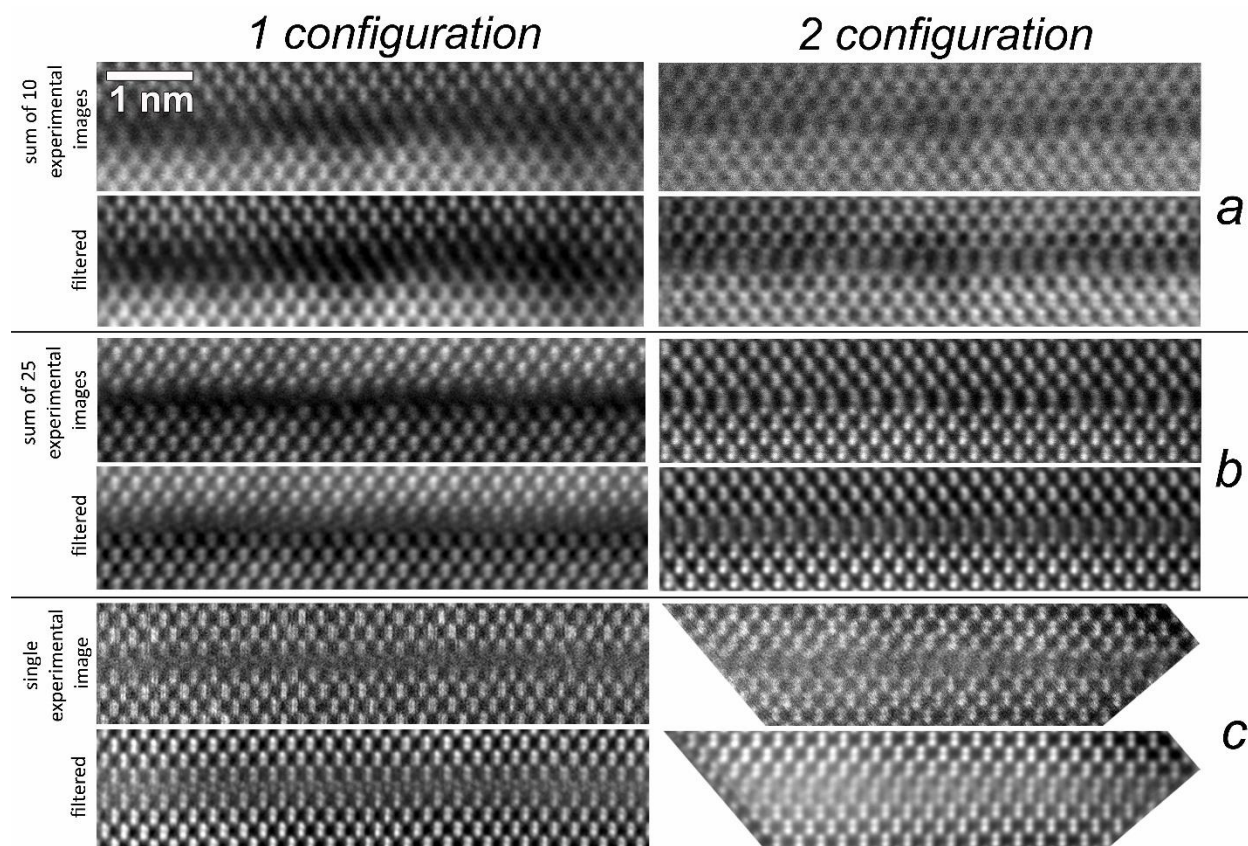


Figure 3.2. Comparison of different imaging methods of the platelet. (a) Sum of ten ADF-STEM images obtained with high dwell time each $1.7 \cdot 10^5 \text{ e}/\text{\AA}^2$. Noise filtered images are presented below the summed images. (b) Sum of 25 ADF-STEM images obtained with low dwell time each $8.2 \cdot 10^4 \text{ e}/\text{\AA}^2$. Noise filtered images are presented below the summed images. (c) ADF-STEM images acquired with standard conditions $1.3 \cdot 10^6 \text{ e}/\text{\AA}^2$ and $7.3 \cdot 10^5 \text{ e}/\text{\AA}^2$.

This method provided quite successful results for the second configuration of the platelet but mostly failed to determine the structure in the middle of the first configuration due to the beam damage, already occurring after a couple of frames. Multiple scanning also caused a bending of the platelet which resulted in the difference in ADF-STEM contrast on both sides of the defect (figure 3.2 a and b). Some hints of the structure of the first configuration can be found in the noise filtered images which are presented below each experimental image on the figure 3.2. They are obtained by Fourier filtering of the experimental images by selecting every pronounced reflection. However, this kind of filtering can only help to get a preliminary idea on the atomic configuration as the masking procedure can easily introduce artefacts.

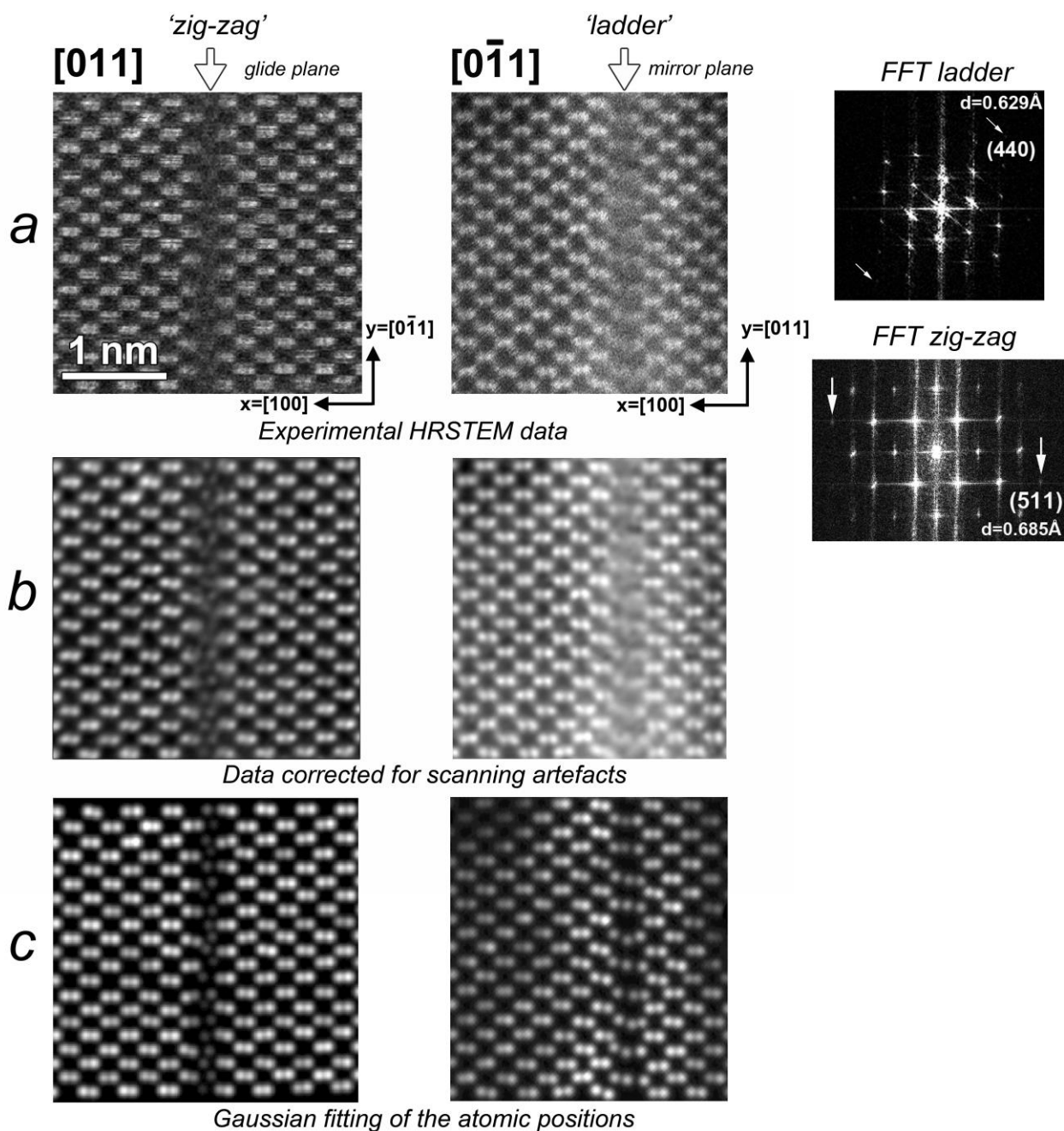


Fig. 3.3. a. Experimental high resolution ADF-STEM images of two observed configurations of the platelet defect – zig-zag and ladder. b. Experimental images corrected for scanning artefacts with the image processing technique based on neural networks [77] trained on the STEM data. c. 2D Gaussian fitting of the atomic positions done for experimental images (a).

Summarizing, the technique with image stacks provided the consistent data for both observed configurations, and thereby, reassured us of the existence of only two platelet configurations.

Finally, we found that the best way to image the internal structure of the first configuration is to acquire one single image with the dose higher than for one frame in an image stack. This allows to distinguish the atomic structure and still not to damage it with multiple scans (figure 3.2c). The visualisation of the second configuration with this standard technique also provides relatively good results, however noisier than a summed image obtained from a stack. The dose was approximately equal to $1.3 \cdot 10^6 \text{ e}^-/\text{\AA}^2$ for the image of the first configuration and $7.3 \cdot 10^5 \text{ e}^-/\text{\AA}^2$ for the second (image 3.3 c).

A '*zig-zag*' of atomic columns with weaker intensities can be seen in the first configuration (fig. 3.3 a) and a '*ladder*' where each '*step*' is formed by a number of atomic columns aligned in a straight line, is observed at the second configuration (fig. 3.3 b). In order to remove scanning artefacts and obtain a clearer image of both *zig-zag* and *ladder* configurations a novel image processing technique developed at EMAT and based on convolutional neural networks [148] trained on the STEM data, was applied to the experimental images. The result with corrected scan noise artefacts and reduced background is shown in figure 3.3 b. As follows from the FCC lattice (figure 3.5a,b), the *zig-zag* and *ladder* configurations can be transformed into each other by rotating the diamond lattice for 90° degrees along the defect.

This led us to the logical presumption that only one atomic structure of platelet exists and, due to the random distribution throughout the diamond crystal, this defect can be observed in two different atomic projections at inequivalent $[011]$ and $[0\bar{1}1]$ directions in the FCC diamond crystal (fig. 3.4a). To support this claim a consistent crystallographic model of the platelet is required which we attempt to create by retrieving the atomic positions from high resolution STEM (HRSTEM) images combined with DFT modeling of the internal platelet structure.

Determination of the platelet structure

High resolution STEM images can be modelled by fitting the intensity in the bright spots (which correspond to the atomic columns) to two-dimensional Gaussian distributions [149] together with a background fit. This approach was applied here making use of the StatSTEM software which was developed in EMAT [73]. The fitting procedure increases the accuracy of atomic position definition and helps to avoid false matches in uncertain cases of weak spots. The experimental images of the platelets with glide and mirror symmetry planes and corresponding fitted images are present at the figure 3.3. The defined centers of the 2D Gaussian distributions were used to create the projected atomic coordinates for the two observed cases. The *zig-zag* configuration is confidently fitted prescribing to each scattering intensity in the *zig-zag* one atomic column. Atomic density at each *step* of the *ladder* projection can be interpreted as a linear row of atomic columns and described best assuming three atomic columns in each *step*. The uncertainty in the middle of this projection can arise from the very small projected distance of $60 \text{ pm} \pm 6 \text{ pm}$ between atomic columns which lays at the very limit of the resolution of STEM aberration-corrected microscopes at the moment.

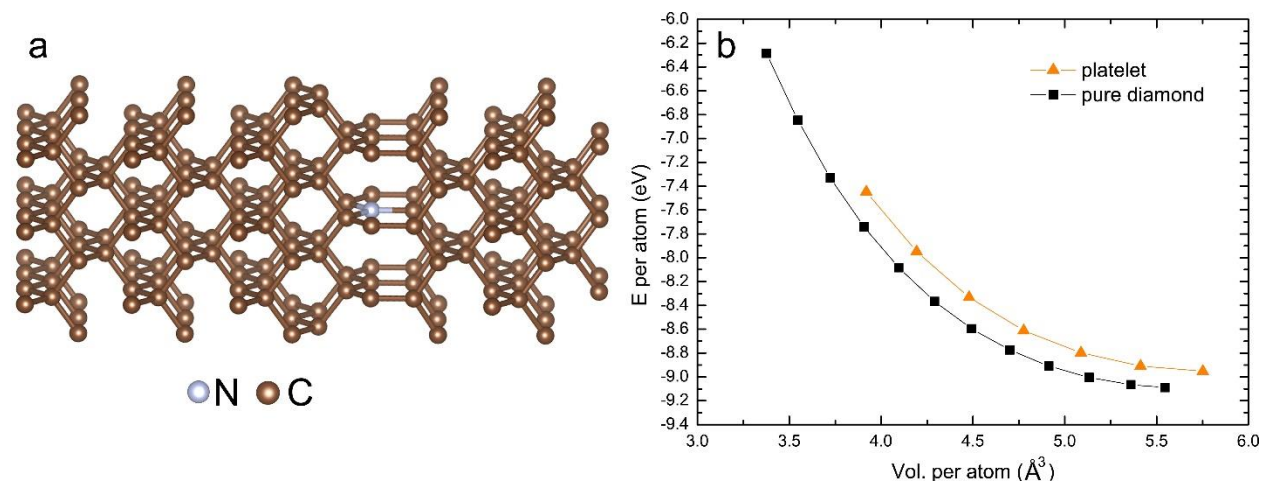


Figure 3.4. a. Proposed structure of the platelet obtained from combining DFT with constraints from the TEM experiment. b. Dependence of the energy per atom on the pressure expressed through the volume per atom for a platelet and pure diamond. The graph is plotted till the minimum energy per atom vs volume per atom for diamond⁷⁷ and the platelet.

As mentioned above, *zig-zag* and *ladder* cases can be represented as two projections of the same structure viewed at 90° with respect to the other (fig. 3.4 b). A number of models can lead to these atomic projections, and the internal atomic arrangement is impossible to retrieve only by high resolution STEM imaging in 2 directions. A projection in [001] zone axis would not provide any additional information hiding the defect structure. Another orientations would not be resolvable due to the very small projected distances in certain orientations. Thus, we used DFT calculations to select the most probable crystallographic model of the platelet that is in accordance with TEM observations.

Starting from a few possible configurations we developed a stable model of the platelet (figure 3.4a). Density-functional band-structure calculations were performed in the VASP package [150,151] with the PBE exchange-correlation potential [152] and the k-mesh containing up to 64 points in the first Brillouin zone. Atomic positions were relaxed until residual forces remained below 0.01 eV/ \AA . The formation energies were determined by comparing with bulk diamond and, in the case of nitrogen defects, with solid N_2 . The unit cell was taken with the size as presented at the figure 3.4a. With the same number of atoms for the defect and a pure diamond, the energy of the platelet is just slightly higher than for the diamond crystal (figure 3.4b) and the addition of one nitrogen atom in the substitutional position lowers it by a minor amount of 0.02 eV per atom. This model is quite similar to the one proposed by Lang [139] but without assuming all the atoms in the chain being nitrogen. The simulations also show that the defect should have metallic nature, a finding which goes along with the low 'band gap' of 1.7 eV of the platelet calculated by studying its luminescence [153].

However, the proposed model would lead only to the *ladder* configuration. To agree with a *zig-zag* crystallographic projection the platelet should contain a few parts were this model is inverted (figure 3.5c). This means that flat chains of atoms in the middle of the defect should randomly switch from right to left orientation or *vice versa* along one 'step' of the *ladder* or at

different ‘steps’. If the transition happens along one chain, a connection point can be the host for nitrogen atoms in the platelet as drawn at the figure 3.5c. This crystallographic model also explains the shifting atomic intensities in the middle of a *ladder* projection (especially, seen at the figure 3.2 a and b) and varying intensity of atomic columns along the *zig-zag* projection. ADF STEM simulations carried out with the QSTEM software [154] maintain the proposed crystallographic model and agree with the experimental images (fig. 3.5 d).

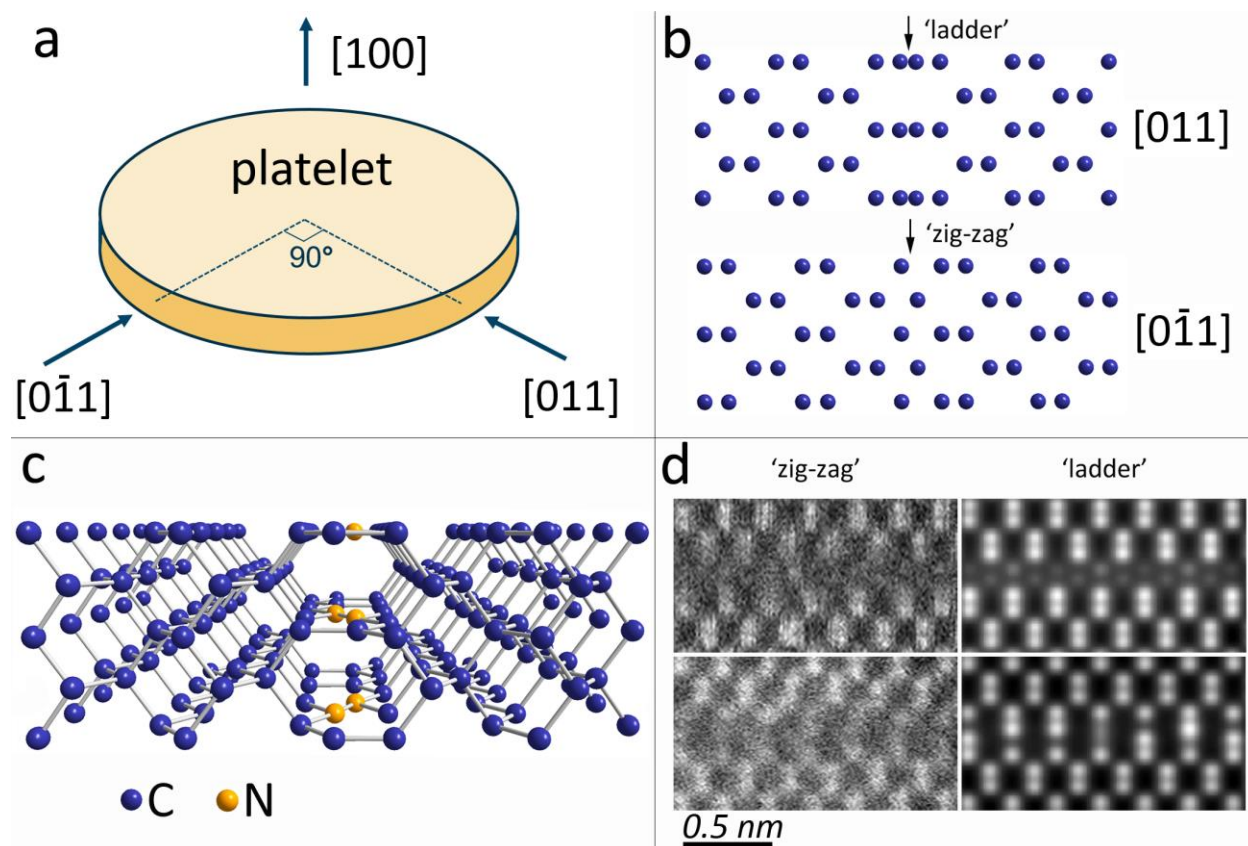


Fig. 3.5 a. Scheme of the platelet in a natural diamond crystal. b. Ladder and zig-zag projections on the platelet observed at inequivalent crystallographic directions [011] and [0-11]. c. Suggested model of the platelet with flat atomic chains switching position from left to right in each ‘step’ of the ladder. d. Experimental and simulated images of the platelet plane. Simulation were carried out for the model (c) with randomly changing chains of atoms.

Role of nitrogen in the platelet investigated by STEM EELS

We also investigate the role of nitrogen in the platelet structure by using the STEM EELS technique. EELS experiments were as well carried out on the FEI Titan³ transmission electron microscope operated at 120 keV and equipped with Gatan Quantum EELS spectrometer with a convergence angle α of 21 mrad and a collection angle β of the spectrometer equal to 75 mrad. The obtained EELS map clearly shows the presence of nitrogen exactly in the platelet plane (fig. 3.6c).

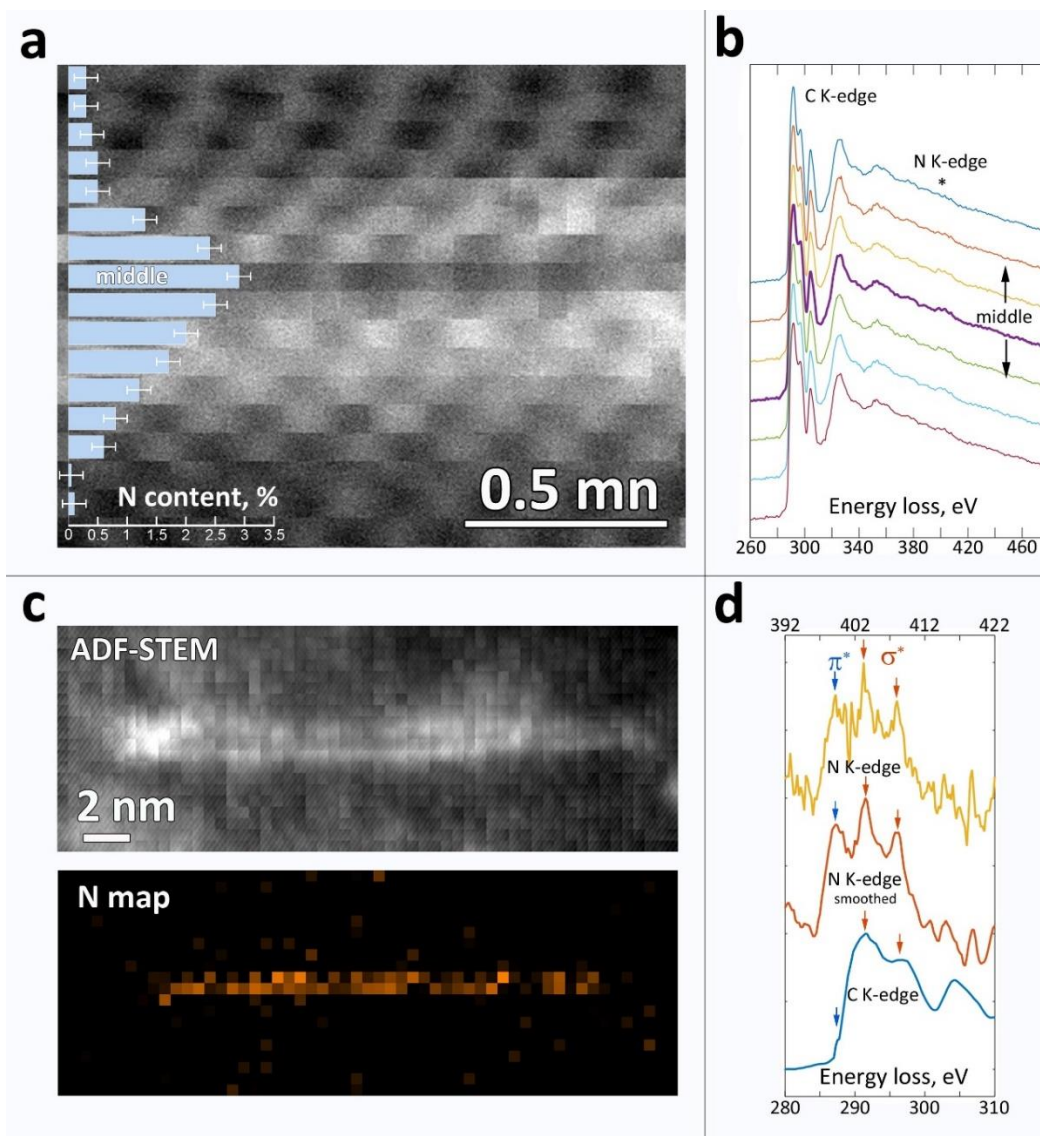


Figure 3.6. *a. Nitrogen concentration in the platelet defect estimated with a spatial resolution of one dumbbell width. b. Spectra of carbon and nitrogen K-edges extracted from each horizontal layer from (a). c. EELS map of nitrogen distribution along the whole platelet. d. Spectra of normalized carbon and nitrogen K-edges extracted from the middle of the defect plane.*

The distribution of nitrogen (fig. 3.6a) calculated along the defect with the spatial resolution of one diamond dumbbell indicates the highest presence of nitrogen equal to 3 atomic % exactly in the middle of the platelet. The nitrogen concentration vanishes in approximately three dumbbell layers. The higher nitrogen concentration present directly at the defect is a clear evidence of its involvement in the platelet structure. Varying concentrations of nitrogen in the platelets detected by us (table 3.1) and in the literature [32,33] suggest a stochastic character of nitrogen participation

in the platelet structure. Most probably, different conditions during diamond formation in the mantle causes changes in the migration of nitrogen [17] which initiate the platelet formation.

Table 1*. Concentration of nitrogen in the platelets measured with EELS.

Nº of platelet	1	2	3	4	5	6	7
N, atom. %	3.4	3.3	2.1	4.0	3.0	3.2	2.0

* Concentration of N was calculated exactly in the defect plane with the width of one dumbbell. The quantification was performed in the EELSMODEL software [155]. EXELFS of the carbon K-edge overlaps with nitrogen K-edge and complicates correct quantification of N. Therefore, the correct values of N in the platelet were obtained by subtracting the 'false' value of N calculated far outside the platelet from the ones obtained on the platelet.

The shape of nitrogen K-edge EELS spectra can give a hint on its coordination in the platelet structure. By comparing the carbon and nitrogen spectra extracted precisely from the defect plane (fig. 3.6 d), one can see that they repeat each other with a few differences. For example, the main peaks of the carbon K-edge related to the σ -bonds in sp^3 -hybridized carbon matches two second peaks of the nitrogen spectra. Also, the small pre-peak in the carbon spectrum responsible for the π^* -bond in sp^2 -hybridized carbon can be correlated with the first peak of the nitrogen K-edge spectra. We suggest that nitrogen is embedded into the diamond lattice and has more sp^2 -like configuration. The shape of the nitrogen spectrum is also close to the spectrum of a single substitutional N_s center as simulated by Turner *et al.* [156] with a pronounced π -component. This proves the substitutional nature of the nitrogen in the platelet and matches with previous research done on its coordination by EELS [157].

Conclusions

We developed a consistent model for platelet defects in diamond, which structure has remained a mystery for almost half a century. We conclude that the platelet has only one atomic configuration, and due to the random orientation in the crystal, it can be observed in two different projections at inequivalent crystallographic directions [011] and [0 $\bar{1}$ 1]. By combining state-of-the-art imaging with novel image reconstruction algorithms, we propose a consistent model of the platelet and support it with DFT calculations. We also contributed to the discussion on the role of nitrogen in the platelet showing its clear involvement in the defect structure and suggesting its possible coordination from EELS and DFT.

We believe that the obtained results can help to better understand and interpret the rich IR absorption and photoluminescence spectra of natural diamonds. The proposed model can also be used to adjust and test the parameters of platelet- and, therefore, diamond formation in the mantle of Earth and shed light on the geological processes behind it.

Chapter 4. Band gap measurement of diamond and other high refractive index materials with off-axis EELS using an annular aperture

In this chapter band gap measurements of semiconductors and insulators with EELS in TEM are discussed in detail, and a simple technique based on the use of an annular (Bessel) aperture is suggested. The technique suppresses the 'parasitic' losses such as Cherenkov losses and surface-guided light modes which complicate the retrieval of the correct band gap value, by enforcing a momentum transfer selection with the Bessel aperture. The suggested approach is experimentally demonstrated and provides good signal to noise ratio and interpretable band gap signals on reference samples of diamond, GaN and AlN while offering spatial resolution in the nm range.

This research is presented in a first author article:

S. Korneychuk, B. Partoens, G. Guzzinati, R. Ramaneti, J. Derluyn, K. Haenen, J. Verbeeck, Exploring possibilities of band gap measurement with off-axis EELS in TEM, *Ultramicroscopy*. in press (2018). doi:10.1016/j.ultramic.2018.03.021.

and in two conferences:

- Hasselt Diamond Workshop, SBDD XXII.
Oral presentation: 'Band gap measurements of diamond materials with EELS using electron Bessel beams'. Svetlana Korneychuk, Rajesh Ramaneti, Yan Zhou, Julian Anaya, Paulius Pobedinskas, Joff Derluyn, Huarui Sun, James Pomeroy, Ken Haenen, Martin Kuball, Johan Verbeeck. Hasselt, Belgium, March 8-10, 2017.
- 13th Multinational Congress on Microscopy
Oral presentation: 'Measuring band gaps of semiconductors by off-axis EELS with Bessel aperture'. Svetlana Korneychuk, Giulio Guzzinati, Rajesh Ramaneti, Paulius Pobedinskas, Joff Derluyn, Ken Haenen, Johan Verbeeck. Rovinj, Croatia September 24-29, 2017.

Band gap measurements with EELS in TEM

As mentioned in the introduction chapter, electron energy loss spectroscopy in transmission electron microscopy provides information about the local dielectric properties of materials including band gap information in semiconducting materials. EELS has an advantage over conventional techniques for band gap measurement by providing much better spatial resolution and the possibility to locally map the band gap, for example, in a multilayered heterostructure [158-161].

So far however, low loss EELS is not widely used for band gap measurements due to the presence of parasitic unwanted losses which are usually superimposed to the band gap signal. These unwanted losses occur e.g. through retardation effects via the emission of Cherenkov radiation [162,163] and the excitation of surface-guided light modes. The challenges of measuring the band gap in the TEM are well understood and have been discussed in great detail [88,91,92,96,164,165] with many propositions on how to overcome them [90,94,97,166,167].

Fortunately, according to the simulations based on the Kröger formula [87] which is given in the introduction chapter and describes low loss inelastic scattering in a plan parallel sample geometry, all the unwanted losses happen at very low scattering angles and can, in principle, be avoided by not recording scattering events in that angular range [92,168]. In this chapter we explore how a hollow cone illumination scheme allows to eliminate the undesired signals and to accurately measure the bandgap in high-refractive-index semiconductors, while retaining a high spatial resolution, the key characteristic of the TEM. Below we experimentally demonstrate that the proposed setup indeed provides excellent suppression of the unwanted loss signals at both high (300 keV) and low (60 keV) beam energies while at the same time strongly suppressing the zero loss peak. This suppression drastically simplifies the retrieval of the band gap signal and significantly improves the signal to noise ratio.

Besides spatial resolution, there is another important difference setting EELS apart from optical techniques. While for photons the momentum transfer to the material making a transition from the valence to conduction band is approximately equal to zero and negligible, in EELS the transfer of momentum between the fast electron and the sample can be substantial [169].

This provides the possibility in EELS to obtain information about all possible interband transitions with the attractive opportunity to deliberately select certain transitions while excluding others. The role of this momentum transfer selection in the proposed setup will be clarified and prospects for applications are outlined.

Experimental set-up

The unwanted Cherenkov and surface losses are characterized by only a small momentum transfer, as becomes obvious when numerically evaluating the Kröger formula [88]. Indeed, these unwanted inelastic interactions produce scattering angles in the μrad range (see fig.4.1b,c), while Bragg scattering typically occurs in the order of mrad for electrons in the 100's keV range. This opens the possibility of avoiding the unwanted part of inelastic scattering by placing the spectrometer entrance aperture off-axis with respect to the unscattered electron beam in the diffraction plane. To first approximation, we can model the intensity distribution in this diffraction

plane as a convolution of (i) the inelastic scattering cross section, assuming a homogeneous medium with a given dielectric function, (ii) the elastic scattering contribution consisting of Bragg peaks due to the atomic structure of the material and (iii) the angular distribution of the incoming electron beam. For plane wave illumination, this results in a series of Bragg spots that are broadened by inelastic scattering. This broadening now contains a small contribution from Cherenkov radiation and a larger one from inelastic scattering, therefore off-axis spectral recording can easily avoid the lowest angles thus suppressing the unwanted Cherenkov effect [96,170,171]. With convergent beam illumination, we obtain better spatial localization, as the probe is now focused on the sample, but lose momentum resolution as different scattering features are now becoming harder to disentangle especially if also the convergent beam electron diffraction (CBED) discs start to overlap and off-axis spectral detection becomes problematic.

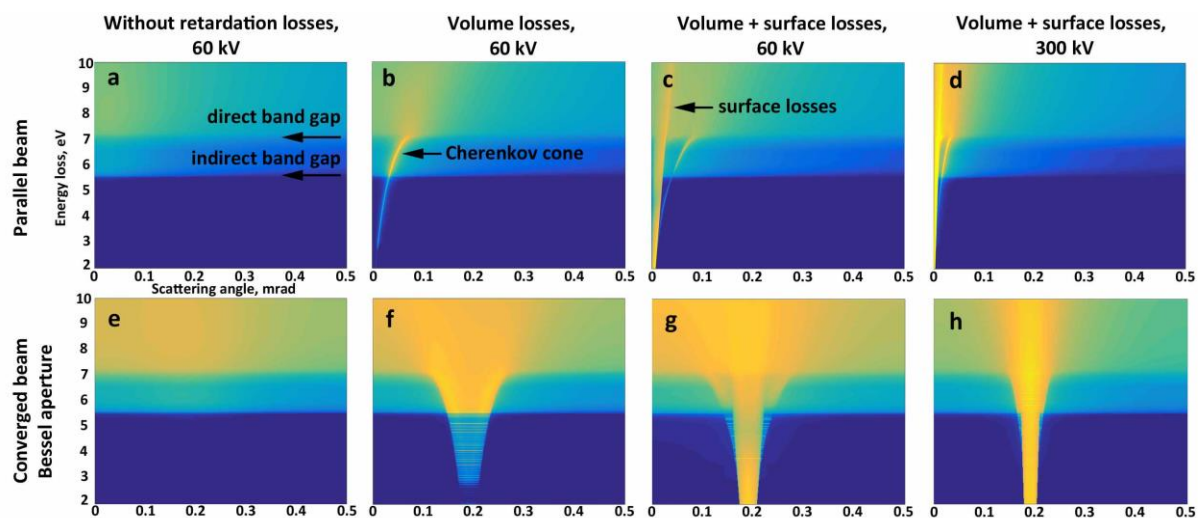


Fig.4.1. Simulated double differential inelastic cross section for a plan parallel diamond thin film (50 nm) at a beam energy of 60 keV and 300 keV as a function of energy loss E and scattering angle θ based on the Kröger equation [172]. Illumination with either a parallel beam or a Bessel beam (0.2 mrad opening angle) is simulated including either only the non-relativistic loss function $\text{Im}(1/\epsilon)$ (a, e), including relativistic effects (b, f) and including surface effect (c, d, g, h). Note the presence of clear Cherenkov and surface losses at scattering angles only below 0.1 mrad and even lower for 300 keV electrons. Using the Bessel beam, shifts these unwanted losses to the opening angle of the beam and creates a region around the center which is free of these unwanted excitations. Stripes at the simulation are caused by numerical artifacts due to noise in the tabulated dielectric function.

A solution can be found by using an annular aperture (fig.4.2a) in the condenser plane of the microscope. This kind of aperture creates an approximation to an electron Bessel beam [61-63,173] and is accordingly called a Bessel aperture. This aperture creates ring-shaped CBED pattern due to the conjugation of condenser and diffraction planes in STEM mode, resulting in an assembly of rings in the diffraction plane as sketched in Figure 4.2.

Chapter 4. Band gap measurement of diamond and other high refractive index materials with off-axis EELS using an annular aperture

By selecting the appropriate camera length (CL) and convergence angle, the central (000) reflection can be made to surround the spectrometer entrance aperture, thus selecting only these scattering events within a certain range of momentum transfers (fig.4.2d).

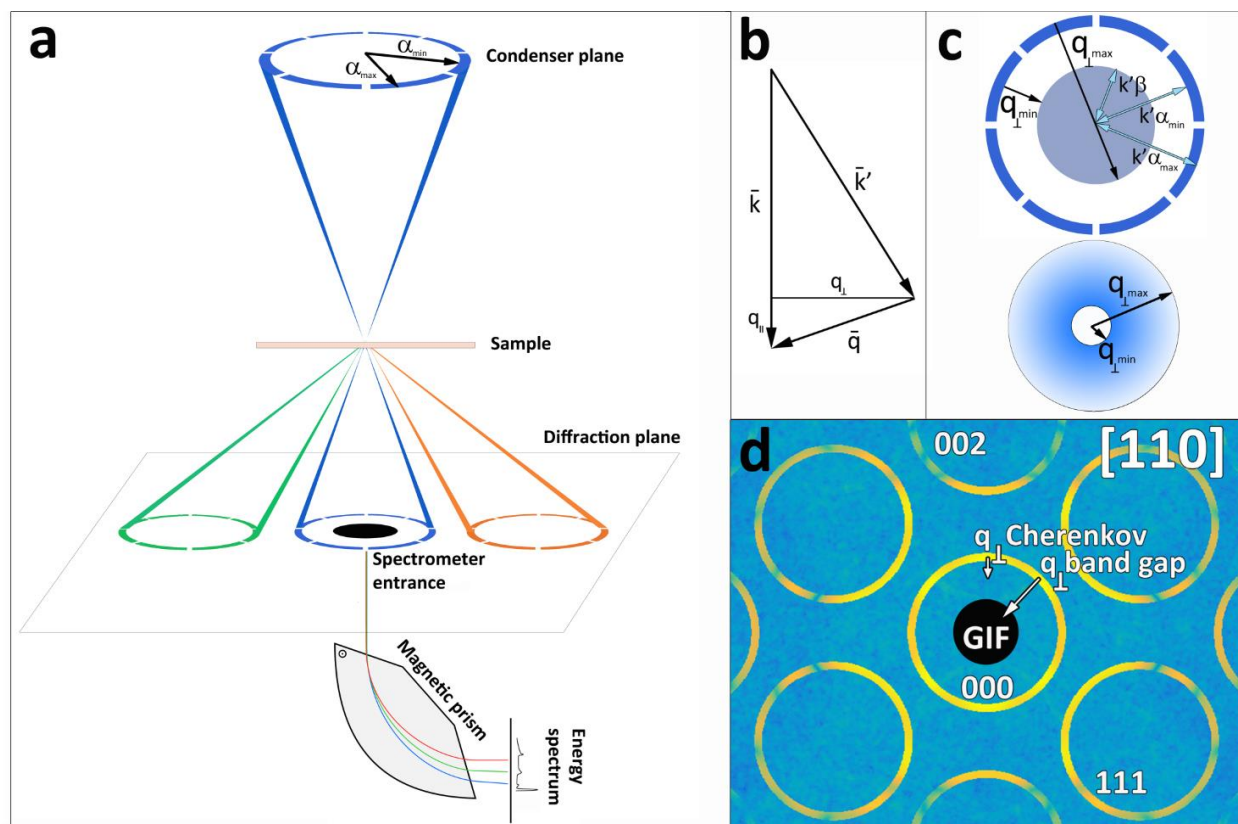


Fig.4.2. *a. Schematic diagram of the off-axis experiment with a Bessel aperture. b. Vector plot of the transfer of momentum in inelastic electron scattering. c. Limits imposed to this transfer of momentum when placing the entrance aperture (central disc) of the spectrometer in the center of the Bessel aperture. d. Simulated CBED pattern [174] of diamond [110] with a Bessel aperture at 60 kV acceleration voltage and 10 mrad convergence angle showing the diffracted rings and the position of the spectrometer entrance aperture. Note how small momentum transfers stemming from Cherenkov radiation can't bring electrons into the spectrometer while larger momentum transfers originating from conventional inelastic losses do end up in the spectrometer. Note also that elastic scattering does not enter the spectrometer and therefore no zero loss peak is expected in the spectrum.*

It is important to highlight that using this Bessel aperture, the scattering distribution will be altered in a fundamental way and can be described by the convolution of the double differential inelastic scattering cross section with the Bessel aperture function. Figure 4.1 e-h demonstrates the result where now the unwanted losses inside the band gap region of the material are shifted to the angles of the ring aperture. This area now contains a significant amount of retardation losses, and

Chapter 4. Band gap measurement of diamond and other high refractive index materials with off-axis EELS using an annular aperture

emerging from it, we can see the Cherenkov cone. The area in the center of the aperture appears free from Cherenkov losses and still contains information of interest on the band gap of the material as long as the opening angle of the ring remains very small with respect to q -dependent changes in the band structure. The figure has been computed for small angles in order to resolve the retardation losses better, while in practice slightly higher angles will be preferred due to the corresponding higher spatial resolution and convenience of staying in the same operating mode in our microscope set-up.

The Bessel aperture can provide an advantage over a standard off-axis with circular aperture for low loss STEM-EELS experiments by circularly averaging over the in-plane momentum transfer direction thus avoiding complications with possible anisotropic features [94].

A major advantage of the setup is the rejection of both the elastically scattered beam as well as the low angle Cherenkov and surface scattering. Indeed, removing the so-called zero loss peak from the spectrum has several advantages as the full dynamic range of the spectrometer can be used to record the loss signal, no subtraction of the zero loss peak is needed and the signal to noise ratio is greatly improved as the undesired (tail of the) elastic signal is suppressed, reducing background and the associated Poisson noise.

Therefore, to simplify the setup the convergence angle of the Bessel beam should be chosen smaller than the Bragg angles in the material in order to keep the rings from overlapping. The situation where they almost touch is considered ideal as it provides maximum suppression of both Cherenkov losses and elastic signal while preserving good spatial resolution, together with a collection angle chosen to be just smaller than the Bessel beam convergence angle. However, working at these conditions will inevitably blur some of the q -dependent band structure features which may or may not be desired, but for q -averaged band gap mapping this could be considered ideal. While the experiment can still be performed in case of overlapping rings, the proper positioning of the aperture between the various reflections and the interpretation becomes increasingly difficult together with reducing the circular averaging advantage.

On the other hand working at smaller opening angles will compromise the spatial resolution of the setup due to the diffraction limit of the probe size [175]. The non-overlap criterion will prevent true atomic resolution with this setup, but in the low loss regime, the spatial resolution is in any case likely dominated by delocalization of the inelastic scattering [169]. The advantage of this regime is that q -dependent transitions can be more carefully selected without the blurring effect that occurs for larger opening angles.

q selection

Unlike optical measurements, the transferred momentum q of the transition from valence to conduction band can be significantly different from zero in EELS experiments while the primary energy of the electron beam is more than enough to excite all possible interband transitions. This leads to a typical low loss spectrum which is very hard to disentangle into a meaningful band structure picture.

Working off-axis with the proposed Bessel setup on the other hand allows to post-select a small subset of the possible transitions by enforcing strict momentum transfer selection criteria,

which could make direct interpretation of the low loss EELS spectrum more manageable in terms of band structure. This post-selection acts only on the perpendicular component \mathbf{q}_\perp of the momentum transfer (fig. 4.2b) where the upper limit $\mathbf{q}_{\perp max}$ of the \mathbf{q}_\perp interval is determined by the sum of the maximum angle α_{max} of the Bessel aperture and the maximum spectrometer entrance aperture angle β as $q_{\perp max} = k' \sin\theta \approx k'\theta = k_0 \sqrt{1 - 2\theta_E} (\alpha_{max} + \beta)$, where forward momentum $k_0 = \frac{2\pi}{\lambda}$ and characteristic scattering angle $\theta_E \approx \frac{E}{2E_0}$ neglecting relativistic corrections [165]. The lower limit $\mathbf{q}_{\perp min}$ is given by the difference of the lowest angle in the Bessel aperture with the spectrometer entrance aperture as $q_{\perp min} = k_0 \sqrt{1 - 2\theta_E} (\alpha_{min} - \beta)$ (fig. 4.2c). The relation between q , θ and θ_E is given by:

$$q^2 = q_{\parallel}^2 + q_{\perp}^2 = k_0(1 - \sqrt{1 - 2\theta_E} \cos\theta + 1 - 2\theta_E) \approx k_0^2(\theta^2 + \theta_E^2). \quad (4.1)$$

A more detailed description of inelastic scattering vector geometry is outlined in [81].

Choosing an appropriate interval via tuning the Bessel aperture geometry with respect to the spectrometer collection aperture allows to select only those transitions that are of interest. The allowed \mathbf{q}_\perp vectors effectively form a donut with radius α and width β assuming the Bessel ring is very narrow compared to the entrance aperture. This ring effectively averages out anisotropic variations in the band structure which may or may not be an advantage depending on what information is desired. The transitions in the q-donut with lower \mathbf{q}_\perp will have higher intensity due to purely geometrical reasons – more of them can end up in the spectrometer entrance than transitions with higher \mathbf{q}_\perp .

In order to understand the effect of this \mathbf{q} selection on the low loss spectra, we have to compute the joint density of states (JDOS) and then we need to add the typical EELS cross section considerations for low loss excitations.

In order to shed light on this rather complicated combination of factors, we demonstrate the effect on a toy model band structure consisting only of two parabolic bands (fig. 4.3a), following arguments laid out for $\mathbf{q}=\mathbf{0}$ transitions in [176,177].

Let's assume that a transition from the valence to conduction band occurs with initial wave vector \mathbf{k}_i and final wave vector \mathbf{k}_f . The conduction band dispersion relation is given as:

$$E_{cb} = E_c + \frac{\hbar^2 k_f^2}{2m_e}, \quad (4.2)$$

where E_c is the bottom of the conduction band energy and m_e is the conduction electron's effective mass. For the valence band the dispersion relation is:

$$E_{vb} = E_v - \frac{\hbar^2 k_i^2}{2m_h}. \quad (4.3)$$

where E_v is the top of the valence band energy and m_h is the hole's effective mass.

The energy transferred from the fast electron to the sample (energy loss) will then be:

$$E = E_{cb} - E_{vb} = E_{bg} + \frac{\hbar^2}{2} \left(\frac{k_i^2}{m_h} + \frac{k_f^2}{m_e} \right), \quad (4.4)$$

where E_{bg} denotes the band gap energy.

Applying momentum conservation we get:

Chapter 4. Band gap measurement of diamond and other high refractive index materials with off-axis EELS using an annular aperture

$$\hbar \mathbf{k}_i + \hbar \mathbf{q} = \hbar \mathbf{k}_f, \quad (4.5)$$

or:

$$\mathbf{k}_f = \mathbf{k}_i + \mathbf{q}. \quad (4.6)$$

Then the expression (4.4) for energy loss can be rewritten as:

$$\frac{\hbar^2}{2} \left(\frac{k_i^2}{m_h} + \frac{(\mathbf{k}_i + \mathbf{q})^2}{m_e} \right) + E_{bg} - E = 0. \quad (4.7)$$

The number of transitions with this energy E is now given by the joint density of states (JDOS):

$$JDOS(E, \mathbf{q}) = 2 \int_{BZ} \frac{d\mathbf{k}}{(2\pi)^3} \delta \left(\frac{\hbar^2}{2} \left(\frac{k_i^2}{m_h} + \frac{(\mathbf{k}_i + \mathbf{q})^2}{m_e} \right) + E_{bg} - E \right). \quad (4.8)$$

To calculate this integral numerically, a Lorentzian representation of the δ -function can be used:

$$\delta(x) = \lim_{\epsilon \rightarrow 0} \frac{\epsilon/\pi}{x^2 + \epsilon^2}.$$

To test the numerical integration, the $\mathbf{q} \sim 0$ case can be considered. For this case, the JDOS can also be calculated analytically as follows (with $m_r = m_e m_h / (m_e + m_h)$):

$$JDOS(E, 0) = 2 \int_{BZ} \frac{d\mathbf{k}}{(2\pi)^3} \delta \left(\frac{\hbar^2 k^2}{2m_r} + E_{bg} - E \right) \quad (4.9)$$

$$= \frac{8\pi}{(2\pi)^3} \int k^2 dk \delta \left(\left(k - \sqrt{\frac{2m_r}{\hbar^2} (E - E_{bg})} \right) \left(k + \sqrt{\frac{2m_r}{\hbar^2} (E - E_{bg})} \right) \frac{\hbar^2}{2m_r} \right) \quad (4.10)$$

$$= \frac{1}{\pi^2} \frac{2m_r}{\hbar^2} \frac{1}{2\sqrt{\frac{2m_r}{\hbar^2} (E - E_{bg})}} \int k^2 dk \delta \left(\left(k - \sqrt{\frac{2m_r}{\hbar^2} (E - E_{bg})} \right) \right) \quad (4.11)$$

$$= \frac{1}{2\pi^2} \left(\frac{2m_r}{\hbar^2} \right)^{3/2} \sqrt{E - E_{bg}}. \quad (4.12)$$

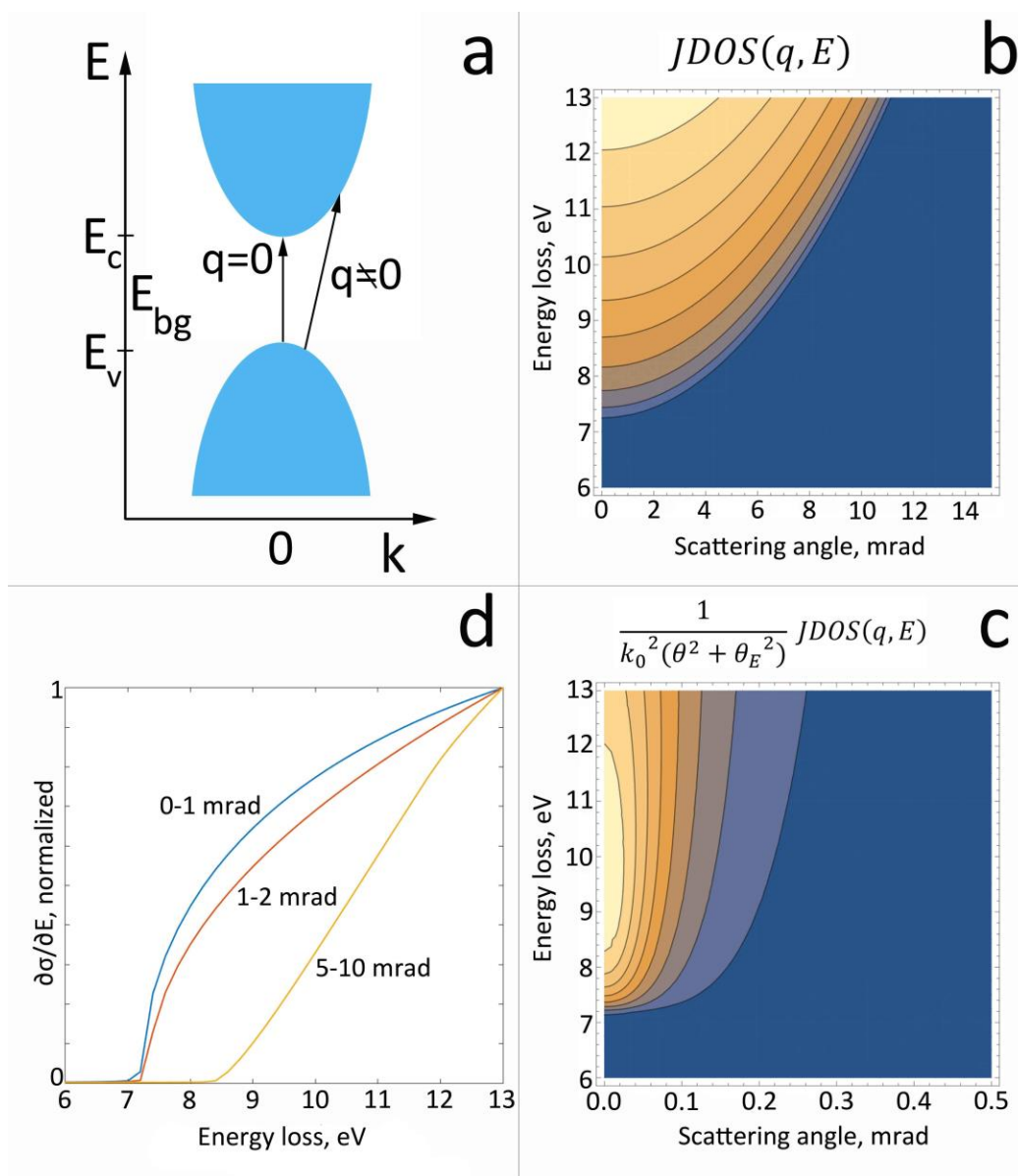


Fig.4.3. a. A schematic two band model for excitations in a material with two parabolic bands. **b.** JDOS dependence on the momentum transfer q (shown through the scattering angle $\theta \approx \frac{q}{k_0}$) calculated for the model. The value of E_{bg} was taken as 7.2 eV in accordance with the direct band gap of diamond. Effective masses similar to diamond were taken as $m_e=0.57m_0$ and $m_h=0.8m_0$ [178]. **c.** Simulation of the double differential EELS cross-section for all q . The Lorentzian distribution of inelastic scattering around low scattering angles is clearly visible and selects predominantly transitions close to $q=0$. **d.** Simulated EELS spectra extracted from (c) for different choices of q calculated using expression (4.13). Note that the onsets will shift towards higher values when increasing the selected q . This constitutes one more reason to use small convergence angles and stay well in the first Brillouin zone.

Chapter 4. Band gap measurement of diamond and other high refractive index materials with off-axis EELS using an annular aperture

The square root dependence of JDOS on energy is also given in literature and is typical for a 3D system [179,180].

We now find the EELS double differential scattering cross section in dipole approximation [181,182]:

$$\frac{\partial^2 \sigma}{\partial E \partial \Omega} \propto \frac{1}{k_0^2 (\theta^2 + \theta_E^2)} JDOS(E, q), \quad (4.13)$$

Taking into account the selected q-donut (fig.4.3) the total cross-section is given by:

$$\frac{d\sigma}{dE} = \int d\Omega \frac{\partial^2 \sigma(\theta)}{\partial E \partial \Omega} \propto \int_{\alpha_{min}-\beta}^{\alpha_{max}+\beta} \sin\theta d\theta \int_0^{2\pi} d\phi \frac{1}{k_0^2 (\theta^2 + \theta_E^2)} JDOS(E, q). \quad (4.14)$$

These cross sections are shown in Figure 4.3d, for the cases $[\alpha_{min} - \beta, \alpha_{max} + \beta] = [0 \text{ mrad}, 1 \text{ mrad}]$, $[1 \text{ mrad}, 2 \text{ mrad}]$ and $[5 \text{ mrad}, 10 \text{ mrad}]$. These simulations demonstrate that band gap value simulated for the on-axis case (0-1 mrad) matches the value obtained slightly off-axis (1-2 mrad), meanwhile the signal obtained at larger angles significantly shifts the band gap towards higher energies. This suggests that the best strategy for band gap measurements is to keep the distance between spectrometer entrance and Bessel aperture (basically, $\mathbf{q}_{\perp min}$) as small as possible though still avoiding the retardation losses. Also it's important to highlight that the smaller convergence angle is the more prominent the direct band gap onset will be due to the higher momentum resolution.

Results

The proposed method was tested on a multilayered semiconductor heterostructure containing nanocrystalline diamond (NCD), AlGa_N, Ga_N and Al_N layers. Two alternative conditions were applied to probe the effectiveness of the technique – using an acceleration voltage of 60 keV which should allow to minimize the Cherenkov losses and using 300 keV where the unwanted effects are expected to be much more pronounced. The energy resolution, given as the full width at half maximum of the zero loss peak is 150 meV. Ga_N, Al_N and AlGa_N being direct semiconductors with rather flat band structure are good objects to compare the band gap values estimated by EELS with the standard ones obtained by optical techniques that only 'see' the direct band gap.

Off-axis EELS measurements as proposed here can be influenced by several experimental details that need to be carefully considered. Starting out with an experiment without a sample already introduces a few peculiarities. As can be seen from Figure 4.4a, the intensity of the zero loss peak (ZLP) acquired in off-axis conditions with Bessel aperture is suppressed by more than 5 orders of magnitude as compared to the same experimental conditions when replacing the Bessel aperture with a standard round aperture. Nevertheless, a ZLP is still weakly present in the spectra while this was not expected.

Somehow, a fraction of the intensity ends up being scattered to the center of the ring in the diffraction plane which could be due to: inelastic phonon scattering, decoherence effects [183], transmission of electrons through the opaque region of the Bessel aperture or less than ideal focusing of the Bessel aperture in the diffraction plane. It turns out, that the dominant effect here is caused by a slight misalignment of the height of the Bessel condenser aperture which leads to a slightly defocused elastic image in the diffraction plane as shown in Figure 4.4c. A typical Arago or

Chapter 4. Band gap measurement of diamond and other high refractive index materials with off-axis EELS using an annular aperture

Poisson spot becomes visible in the center which brings elastic electrons back on the optical axis due to constructive interference effects [175]. This effect is particularly strong for smaller convergence angles. Ideally this effect would be corrected by mechanically lifting the aperture to a different position, but here we have to compensate this effect by slightly defocusing the diffraction lens and make the spot disappear by going to the far field conditions.

Another artefact comes from inelastic scattering to the surface plasmon in the 1 μm thick Au film that is used to fabricate the Bessel aperture. This results in a peak at 2.5 eV that is visible in Figure 4.4a.

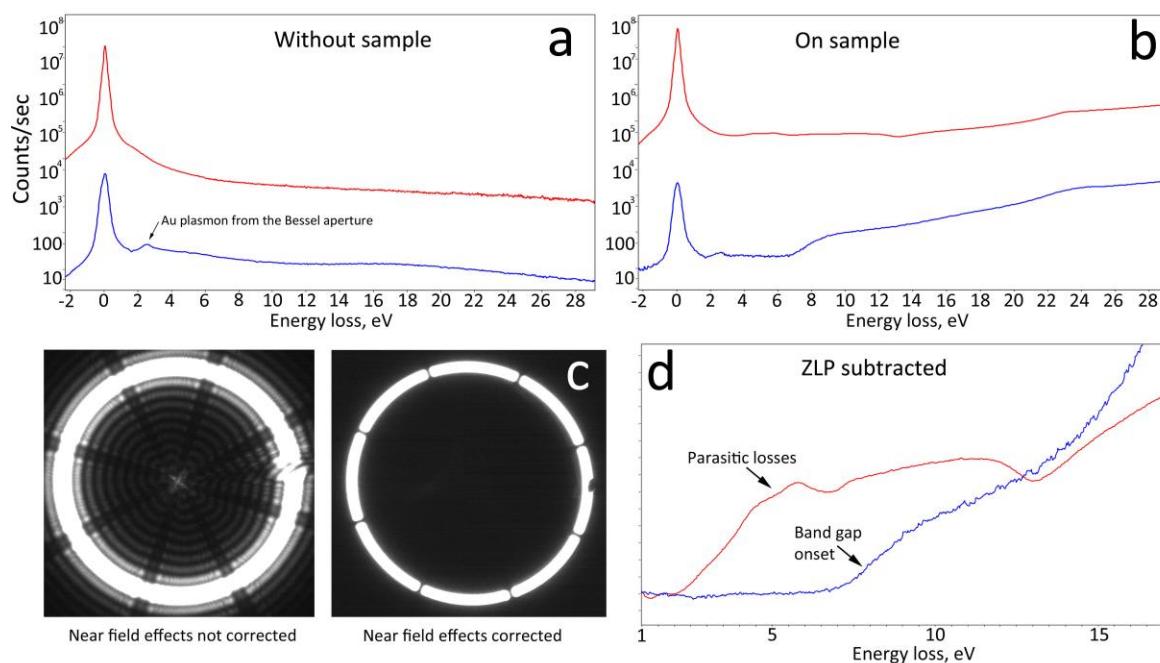


Fig.4.4. EELS spectra taken at 300 kV, 1.5 mrad convergence angle, 1s exposure in off-axis configuration with Bessel aperture (blue) and on-axis configuration with standard round aperture (red) a. without a sample. b. on nanocrystalline diamond. c. Diffraction pattern without sample without refocusing of the diffraction lens showing an Arago spot to appear in the center (left) and with corrected diffraction plane height (right) d. Background removed spectra from (b) by subtraction of the spectrum without a sample in (a). All the spectra are corrected for the same electron dose by taking into account the difference between the areas of the Bessel aperture and conventional round aperture.

Using the same experimental conditions on a polycrystalline diamond film resulted in spectra presented in Figure 4.4b. The 1.5 mrad convergence angle avoids the intersection of Bessel rings due to Bragg reflection occurring at ~ 10 mrad for diamond at 300 keV.

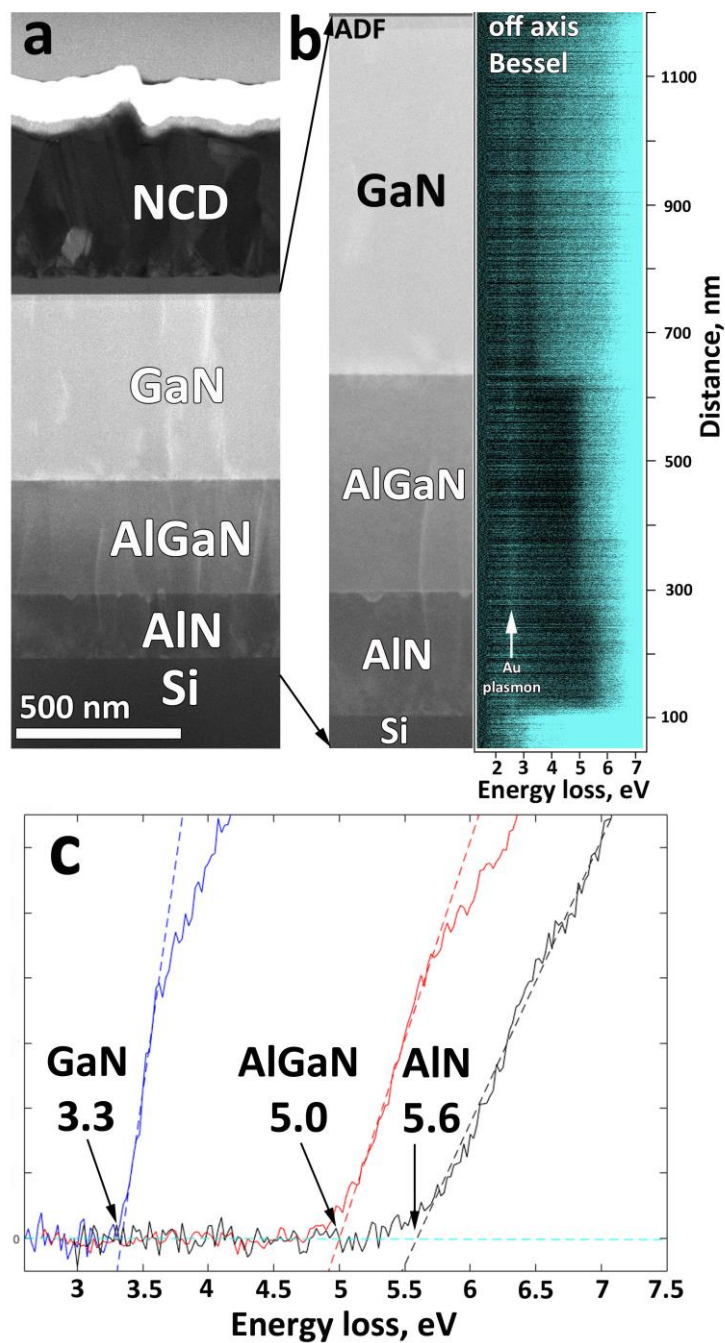


Fig.4.5. a. ADF-STEM image of a FIB lamella prepared from a multilayered heterostructure NCD-GaN-AlGaN-AlN sample. **b.** Background subtracted EELS line profile along the GaN-AlGaN-AlN layers performed in Bessel configurations at 60 keV and opening angle 8 mrad showing good spatial resolution and clear band gap onset. Au plasmon comes from the Bessel aperture. **c.** EELS low loss spectra extracted from the line profile (b) demonstrating band gap onsets for GaN, AlGaN and AlN layers with approximate fitting of band gap values.

Chapter 4. Band gap measurement of diamond and other high refractive index materials with off-axis EELS using an annular aperture

Comparing the intensity of the ZLP for the Bessel case with and without sample results in a very small reduction of the intensity due to absorption and scattering while quasi elastic phonon scattering [80] and other very low loss excitations apparently do not contribute significantly to this peak when compared to the case for the conventional round aperture.

In conclusion we observed that the dominant contribution is likely coming from a residual slight defocus of the diffraction plane, but the two orders of magnitude suppression of the ZLP is already a very welcome effect to significantly increase the reliability of the background removal step and to lower the dynamic range of the spectrum for recording on a detector.

Background subtracting the low loss spectra with the no-sample spectra (fig. 4.4d) shows a significant reduction of unwanted losses for the Bessel configuration even at 300 keV where the Cherenkov losses are typically very pronounced for diamond (fig. 4.1d,h). This experiment shows the effectiveness of the proposed technique even at high acceleration voltages and for high refractive index materials.

It's worth noting that even at 60 keV which is, sometimes, considered as a 'safe' acceleration voltage for band gap measurements, Cherenkov losses in high refractive index materials like diamond ($n=2.4$) cannot be completely eliminated (fig.4.1).

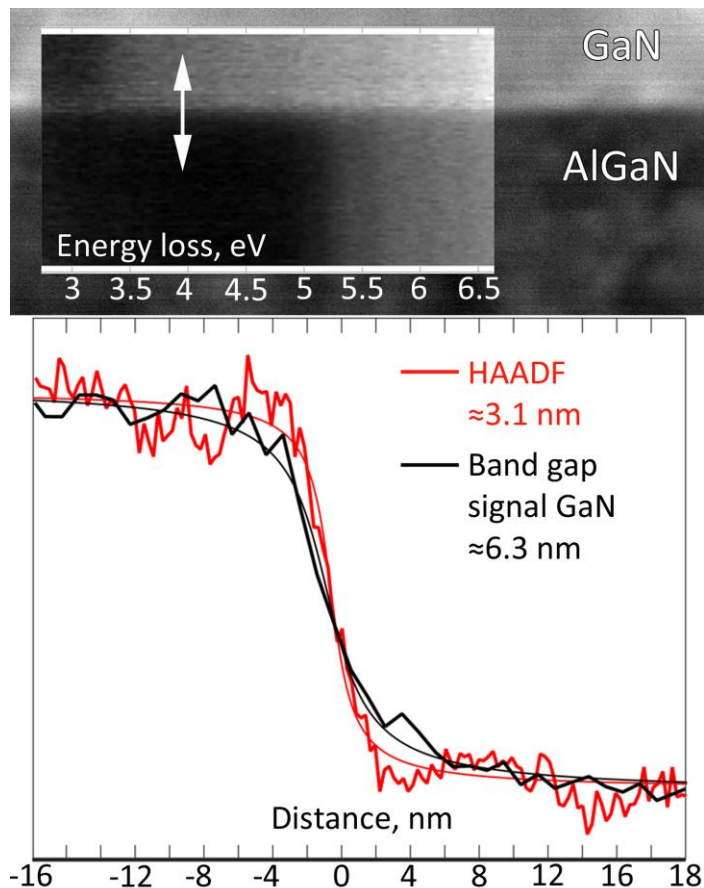


Figure 4.6. Comparison of the delocalization of HAADF and low loss EELS signals.

Diamond, being an indirect semiconductor represents a complication due to the presence of two band gaps – an indirect one at ~ 5.5 eV and a direct one at ~ 7.4 eV [178]. A simulated double differential inelastic cross section based on the tabulated dielectric function of diamond [8] clearly shows both band gap onsets (fig.4.1a). In the experimental spectra we can clearly identify only the direct band gap at 7.4 eV due to, the dominance of the scattering angles close to $q=0$ via the Lorentzian distribution of the inelastic scattering. This makes the result similar as for an optical measurement at $q=0$ for direct transitions. The indirect band gaps may be measured by selecting q in a specific range corresponding to the length and direction of this transition. This attractive possibility will be investigated in the next chapter, and here, we concentrate on eliminating the retardation losses and improving the direct band gap signal.

In order to demonstrate the main advantage of STEM-EELS for band gap measurements – spatial resolution– we obtained EELS line profiles over multilayered lamella (fig.4.5a) at 60 keV. A slightly higher convergence angle of 8 mrad is used in order to increase the spatial resolution while still avoiding Bragg reflections to overlap. The results are presented in Figure 4.5.

The proposed configuration gives an advantage in signal to noise ratio (SNR) when acquiring low loss spectra as the ZLP intensity is strongly suppressed making higher exposure times possible without saturating the detector. The same SNR can be achieved on axis only when adding up a significant amount of spectra with lower exposure times.

The background subtracted low loss spectra acquired when scanning over the epitaxial GaN, AlGaN and AlN layers demonstrates the mapping of clear band gap onsets at relatively high spatial resolution. As these materials are direct semiconductors with relatively flat band structures, the results for GaN are in good agreement with optical methods [184]. Lower band gap value for AlN and higher value for AlGaN can be the sign of Ga contamination for AlN and Ga depletion for AlGaN introduced during the synthesis. It has to be noted however that optical methods could not obtain the spatial resolution presented here (fig.4.6).

Spatial resolution of the experiment is determined for HAADF and low loss EELS signals by comparing both intensity profiles across the GaN-AlGaN interface. We want to point out that we chose to keep the convergence angle as low as 8 mrad at 60 kV and we deliberately apply coarse spatial sampling in view of the delocalized nature of the inelastic signal. The extracted intensity profiles are fitted with $y = a(\text{atan}(bx + c)) + d$ and the resolution is estimated as the distance on the axis x between 15% and 85% of the y function. The estimated experimental resolution for the HAADF signal is 3.1 nm and for the low loss EELS signal at 4 eV we find 6.3 nm. The expected delocalization for 4 eV loss is 5.5 nm calculated from $\Delta L = \frac{0.5\lambda}{\theta_E^{3/4}}$ [79]. The acquisition was performed with a Bessel aperture in off-axis configuration.

Reaching the polycrystalline diamond layer, however, the situation is more complicated and the resulting spectra are displayed in Figure 4.7a. Note that not in all grains of the polycrystalline sample a clear band gap signal is obtained. The reason for this is linked to different grain orientations leading to a complicated appearance of Bragg spots, causing changes in the length of $q_{\perp min}$ and $q_{\perp max}$ together with the shape of q -selection and, therefore, introducing directional effects and collecting the transitions with much higher values of q than for the direct band

transitions. This can lead, firstly, to a significant decrease of band gap signal and, secondly, to the shift of the band gap onset to higher values.

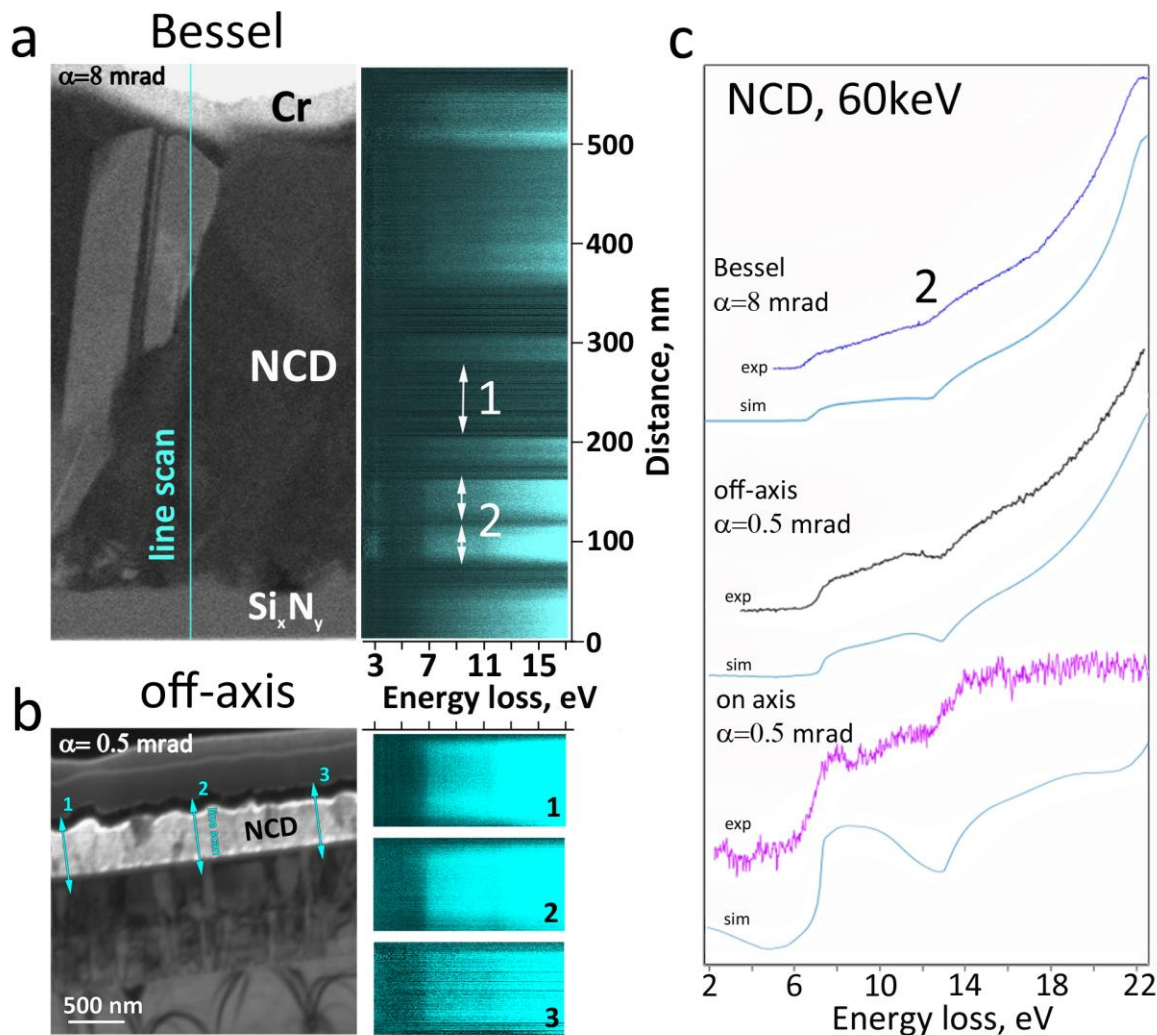


Fig.4.7. *a. EELS line profile over the NCD layer taken at 60 kV and with a Bessel aperture convergence angle of 8 mrad. b. EELS line profiles over the NCD layer acquired with the same acceleration voltage but with a much smaller convergence angle of 0.5 mrad in off-axis conditions with a conventional round aperture. c. Diamond spectra extracted from the line profiles with different experimental conditions accompanied with the corresponding simulated spectra retrieved from the Kröger equation. In case of the off-axis Bessel set-up, the band gap signal was extracted from the grains marked with 2. Note that at 8 mrad convergence angle not all the grains demonstrate clear band gap onsets due to diffraction effects and/or collected q -transitions selected too far from the direct band gap. The band gap onsets acquired using small convergence angles are much more consistent over the whole thickness of the polycrystalline diamond layer.*

Chapter 4. Band gap measurement of diamond and other high refractive index materials with off-axis EELS using an annular aperture

This effect can be overcome by choosing a smaller convergence angle of 0.5 mrad (fig 4.7b) but unfortunately in our current setup, the correction of the diffraction plane position leads to problems with the pivot points making the diffraction pattern shift when scanning the beam. Therefore, we opted for a standard off-axis setup where we used a conventional round aperture giving 0.5 mrad convergence angle and we shifted the central disc slightly away from the spectrometer entrance aperture. The results are presented in Figure 4.7c and show a band gap onset signal that is now independent of the grain orientation and with good spatial resolution over the whole extension of the NCD layer.

Conclusions

The data shown in this chapter demonstrates the efficiency of off-axis acquisition with Bessel aperture even at high acceleration voltages, as 300 keV, and for materials with high refractive index, like diamond. Following simple rules such as using relevant convergence angles and preventing the appearance of near-field effects, this technique can be performed at any microscope with a reasonable spectral resolution by simply exchanging a circular condenser aperture for a specifically designed ring aperture.

The interpretation in terms of a simple two band model gives insight in the momentum transfer selection and helps to choose the right acquisition parameters.

Chapter 5. Measurement of the indirect band gap of diamond with EELS

Continuing the ideas from the previous chapter, a simple method to measure the indirect band gap of diamond with off-axis EELS is demonstrated in the current chapter. The momentum space resolution achievable with EELS and the possibility of deliberately selecting specific transitions of interest are discussed. Using a two parabolic band model similar to the one described in the previous chapter, the predictions are extended from the direct band gap case to an indirect band gap. Finally, the emerging possibility to partly reconstruct the band structure with EELS exploiting our simplified model of inelastic scattering and support it with experiments on diamond, is pointed out.

This research has resulted in a first author publication which is currently under revision:

S. Korneychuk, G. Guzzinati, J. Verbeeck, Measurement of the indirect band gap of diamond with EELS in TEM, *Phys. Status Solidi (A)*, in press (2018), doi:10.1002/pssa.201800318.

and was presented on the conference:

Hasselt Diamond Workshop, SBDD XXIII.

Poster presentation: 'Exploring possibilities of band gap measurement with off-axis EELS in TEM'. Svetlana Korneychuk, Bart Partoens, Giulio Guzzinati, Rajesh Ramaneti, Joff Derluyn, Ken Haenen and Jo Verbeeck. Hasselt, Belgium, March 7-9, 2018.

Probing the band structure with EELS

The use of EELS to study dielectric properties is hampered by existing ambiguities in the data interpretation. There are two major challenges in low-loss EELS, parasitic losses, discussed before in great detail, and the second one being the deciphering of the spectra and linking each peak to its related transition in the 3D band structure. The difficulty lays in the nature of the process - an electron of the primary beam inelastically interacts with a specimen promoting electrons in the material to higher unoccupied levels. Therefore, in a first approximation, EELS spectra represent only the *joint* density of states between occupied and unoccupied levels. This is both valid for the core-loss (excitation of inner shell electrons) and low loss (e.g. interband transitions) spectral ranges and means that it is impossible to directly reconstruct the band structure just from the EELS spectra alone. The possible non-zero momentum transfer in EELS further considerably complicates the interpretation of the spectra. The only easily interpretable feature is the onset of a direct band gap - as it forms the shortest transition from the highest point of the valence band to the lowest point of the conduction band. The indirect band gap can also be measured by selecting the momentum transfer \mathbf{q} which corresponds to the indirect transition with the smallest energy loss as it was demonstrated for the case of Si [96].

In this chapter, we concentrate on exploring the limitations of EELS in terms of band structure investigation. As EELS spectra represent only the joint density of states, a reference to any absolute energy level is lacking and it is impossible to simultaneously recreate valence and conduction energy levels without some prior knowledge, for example, the energy of the highest point of the valence band. Despite this limitation, we aim to demonstrate here that EELS can still be used to measure the indirect band gaps in diamond as well as other specific transitions in the band structure. Continuing the topic of indirect band gap measurements, in this chapter we also demonstrate the importance of the momentum resolution for reliably obtaining the value of the indirect band gap, both experimentally and by simulating the indirect transition on the simple two-band model. We highlight the theoretical aspects which make possible to measure the indirect band gap with expected accuracy and bring attention to the applicability of the fitting parameters for indirect band gap onsets and other indirect transitions. We also point out to the emerging possibility to partly reconstruct the band structure.

Experiment

The best method to obtain the information about the local composition of the material is STEM-EELS mapping. However, high spatial resolution in this mode comes at the expense of a reduced resolution in the transferred momentum, related to the uncertainty principle. Poor momentum resolution means that we acquire information about many possible interband transitions at once, in each single spectrum. As the momentum change \mathbf{q} of an inelastically scattered beam electron is transferred to a momentum change in the sample, via e.g. an interband transition of the crystal electrons, and as the probability for inelastic scattering events decreases rapidly for increasing \mathbf{q} (as discussed further, see eq.15), indirect transitions requiring high momentum

transfer \mathbf{q} are often not detectable in the presence of other signals. Therefore, specific momentum transfer selection and good momentum resolution are required in order to pick up only certain specific transitions, for example, the indirect band gap in diamond. The question is then: how can this be achieved in the experiment? Let's illustrate the idea starting with the description of our experimental set-up. When a focused electron beam scans over the crystalline sample, it is diffracted by the crystal and forms a CBED pattern in the detection plane. The EELS spectrometer entrance is positioned in this plane and the momentum resolution is determined by the combination of the relative size of this entrance aperture expressed by the semi-collection angle β and the convolution with the semi-convergence angle of the probe α . There are a few consequences following from this set-up that should be pointed out:

(1) The CBED pattern can be approximated as a convolution of a conventional electron diffraction pattern of the sample with the incoming momentum distribution. Elastically scattered electrons are confined to the resulting diffracted CBED disks. Parasitic losses are, as has been shown before [86], present only in a narrow angular range from any elastically scattered electron direction, and hence are present only in a region of a few tens of μrad larger than the elastic CBED discs. Inelastically scattered electrons can scatter further outside the elastic regions, but the probability decreases rapidly with scattering angle as described by equation (1.31). Due to the high probability for multiple elastic scattering, and the low probability of multiple inelastic scattering we assume single inelastic scattering. This allows us to model the angular distribution as a convolution of the multiple elastic scattering CBED discs with the angular distribution of a single inelastic event.

(2) Momentum transfer \mathbf{q} has a parallel and perpendicular component (figure 5.1b). \mathbf{q}_\perp lays in the diffraction plane and can be determined through inelastic scattering angle as $\mathbf{q}_\perp = \mathbf{k}_0\theta$ and \mathbf{q}_\parallel relates to the energy loss and can be expressed as $\mathbf{q}_\parallel = \mathbf{k}_0\theta_E$, where θ_E is the so-called characteristic scattering angle [79]. Considering that losses of interest in this manuscript are in the few eV range, \mathbf{q}_\parallel is very small with respect to any features in the first BZ. For instance, for 10 eV loss and 80 keV acceleration voltage $\theta_E = \frac{E}{2E_0} = \frac{10 \text{ eV}}{160000 \text{ eV}} \approx 0.06 \text{ mrad}$ and Bragg angles, which determine important points of the BZ are of the order of several mrad, e.g. 20.3 mrad between the (000) and (111) reflections in a diamond sample oriented in the [110] zone axis at 80 keV. Having a fixed \mathbf{q}_\parallel and a free value of \mathbf{q}_\perp means the transitions, in reciprocal space form a horizontal plane (ignoring the curvature of the Ewald sphere), shifted slightly from the Γ point along the beam direction by exactly $\mathbf{k}_0\theta_E$. Since this shift is so small with respect to the main features of the BZ, we choose to neglect it. Furthermore, the parallel component is dominant only in case of $\theta < 2\theta_E$ [185] which means that for most interband transitions of our interest, where the scattering angles are of the same order as the Bragg angles $q_\perp \gg q_\parallel$. Therefore, exploring indirect band gap transitions we can concentrate on the perpendicular component of \mathbf{q} which lays in plane with the CBED disks and spectrometer entrance.

(3) The combination of statements (1) and (2) means that in CBED each point in the first BZ is convoluted with a momentum uncertainty disk with a diameter of 2α .

(4) Our resolution over the transferred momentum $\mathbf{q}_\perp = \mathbf{k}'_\perp - \mathbf{k}_{0\perp}$ is determined by the uncertainties over the orthogonal components of the initial and final momentum. Since the incident beam possesses a convergence semi-angle α , we will have an uncertainty over the initial transverse

momentum $\delta\mathbf{k}_{0\perp} = \alpha k_0$. On the other hand, the finite angular size β of our detector entrance collects electrons with a variety of final transverse momenta $\delta\mathbf{k}'_{\perp} = \delta k_0$. The resulting \mathbf{q}_{\perp} resolution can therefore be estimated as a quadratic sum $\delta\mathbf{q}_{\perp} = \sqrt{\delta\mathbf{k}_{\perp}^2 + \delta\mathbf{k}'_{\perp}{}^2} \approx \sqrt{\alpha^2 + \beta^2} k_0$. As a measure of quality of this momentum resolution, it is useful to express this quantity as relative to the momentum transfer of Bragg scattering.

(5) Since, as discussed above, a 2D plane from the 3D JDOS is selected including the center and perpendicular to the beam direction, we can select one point from this plane to identify a specific value of \mathbf{q}_{\perp} in both length and direction. Our spectrometer acquires all transitions that meet the selected \mathbf{q}_{\perp} , regardless of the exact initial and final states of the sample. While this hampers a straightforward reconstruction of the band structure, there is an exception where the initial and final states are well known: the band gap. There is indeed only one combination of initial and final states yielding the minimum energy: the highest point of the valence band, at the Γ -point, and the lowest point of the conduction band. This transition becomes clearly identifiable once we select the proper momentum transfer.

(6) As following from the statement (5), indirect and direct band gap transitions can be probed deliberately with EELS if the momentum resolution and selection is chosen adequately. We can further suggest that, for example, in the case of diamond there is only one single clear and isolated maximum in the band structure [186], leading to a high density of occupied states in that point. This means that the majority of scattering will originate from this Γ point. This further simplifies the interpretation and opens an interesting possibility to deliberately measure the energy difference between the highest point of the valence band (which is dominant as discussed above) and arbitrarily chosen points in the conduction band (not necessarily the bottom of the conduction band).

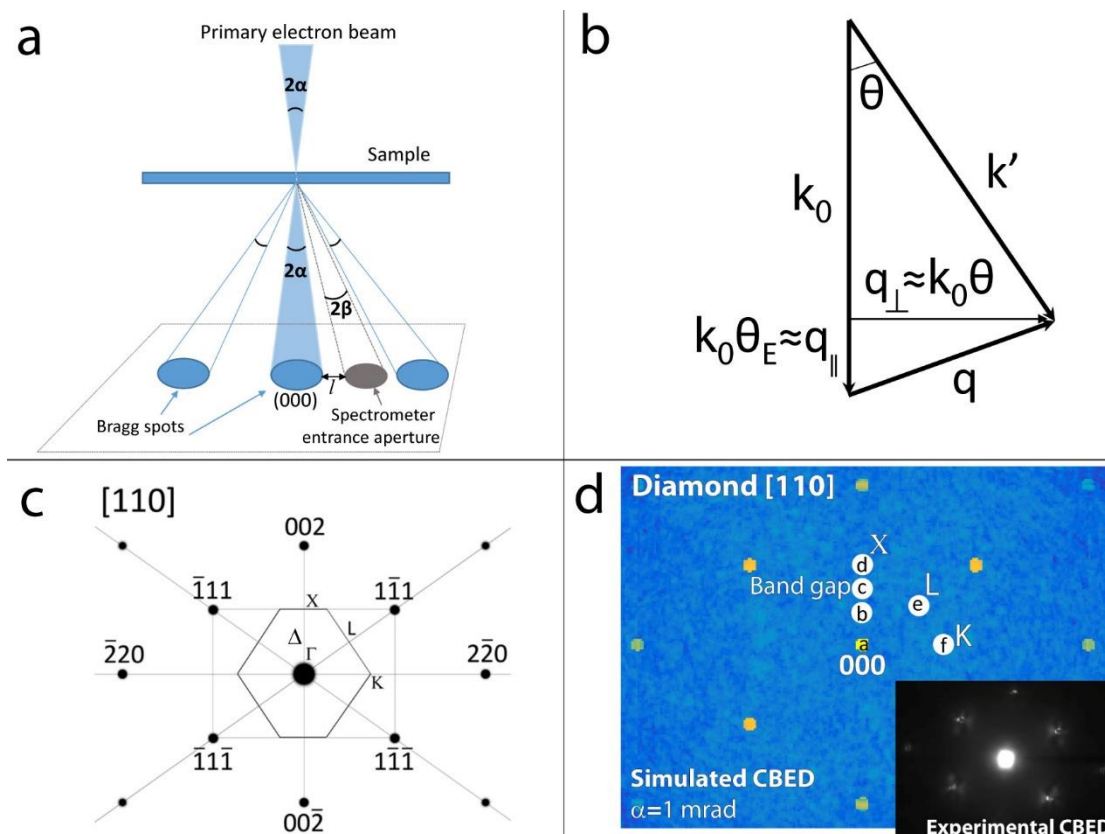


Figure 5.1 a. Scheme of the experiment in STEM mode. A convergent electron beam is directed on the sample, where it undergoes elastic (Bragg) and inelastic scattering. A spectrometer with a small acceptance angle collects scattered electrons close to a chosen scattering angle. α and β indicate the convergence and acceptance semi-angle respectively. b. Vectorial relations between initial momentum k of the electron of the primary beam, final momentum k' and momentum transfer q . c. Scheme of the boundaries of the slice of the first BZ in case of parallel beam illumination marking the main symmetry points Γ , X , K and L of interest and the symmetry line Δ between Γ - X . d. The simulated [174] CBED pattern of diamond in $[110]$ crystallographic orientation at 80 keV with a thickness of 35 nm and convergence angle $\alpha=1$ mrad used in the experiment. The white circles with radius $\beta=1.2$ mrad show the different positions of the spectrometer entrance aperture used in the experiment. Inset shows the experimental CBED pattern. Letters a-f correspond to the spectra at figure 5.4 b and c.

Model

In the previous chapter we used as an illustrative tool the simple band structure model consisting of two parabolic bands showing how momentum selection through off-axis EELS acquisition can influence the signal of the direct band gap. We concluded that the best strategy to obtain a good estimate of the value of the direct band gap is to keep the off-axis shift as small as possible while still avoiding the angular range where the retardation losses (Cherenkov and surface guided modes) are relevant. However, for the indirect band gap, the situation is different as we need to deliberately select the appropriate momentum transfer q_{\perp} corresponding to the indirect

transition with lowest energy loss. The momentum transfer is in any case large enough that we do not have to worry about parasitic losses. The downside, however, is that the probability of scattering, and therefore the signal to noise ratio, decreases significantly with \mathbf{q}_\perp and the shape of the band gap onset will change substantially as well.

To demonstrate how this combination of factors influences the indirect band gap signal, we extend the simple 2 parabolic band model with a shift of the conduction band by a vector \mathbf{s} from $\mathbf{k}=\mathbf{0}$ in momentum space (fig.5.2). We want to point out that in the real band structure of diamond there are six such symmetrical band minima related to the indirect band gap but in our experiment we select only one of those by deliberate momentum selection. Therefore, the choice of only one conduction band shifted by the vector \mathbf{s} would already contain the essential ingredients to understand the experiment. In a first approximation (see equations 5.15 and 5.16), EELS spectra are proportional to the JDOS as both an occupied initial and an unoccupied final state should be available for the inelastic transition to happen.

We attempt to calculate it for the system described above with momentum transfer $\mathbf{q}_\perp \neq 0$. We base our calculations on the well-known example of JDOS for parabolic dispersion relations in 3D system where [187]:

$$JDOS = \frac{\partial \rho}{\partial E} = \frac{\partial \left(\frac{k^3}{3\pi^2} \right)}{\partial E} = \frac{1}{2\pi^2} \left(\frac{2\mu}{\hbar^2} \right)^{3/2} \sqrt{E - E_{bg}}, \quad (5.1)$$

with ρ – volume density of states, μ - reduced mass and E_{bg} – band gap value.

Thus, to obtain the JDOS with $\mathbf{q}_\perp \neq 0$ we only need to find the expression for a wave vector \mathbf{k} shown by the steps below.

Using the same formalism as for the case of direct band gap [95] we can write that an indirect transition from valence to conduction band will have the energy:

$$E = E_{cb} - E_{vb} = E_{bg} + \frac{\hbar^2}{2} \left(\frac{k_i^2}{m_h} + \frac{(\mathbf{k}_f - \mathbf{s})^2}{m_e} \right), \quad (5.2)$$

where E_{cb} is the minimum energy level of the conduction band, E_{vb} – maximum energy level of the valence band, E_{bg} - energy of the band gap, \mathbf{k}_i - initial wave vector, \mathbf{k}_f - final wave vector, m_h and m_e - hole and electron effective masses.

Taking into account the momentum conservation:

$$\hbar \mathbf{k}_i + \hbar \mathbf{q}_\perp = \hbar (\mathbf{k}_f - \mathbf{s}), \quad (5.3)$$

or:

$$\mathbf{k}_f = \mathbf{k}_i + \mathbf{q}_\perp + \mathbf{s}, \quad (5.4)$$

we can rewrite equation (1) as:

$$\frac{\hbar^2}{2} \left(\frac{k_i^2}{m_h} + \frac{(\mathbf{k}_i + \mathbf{s} + \mathbf{q}_\perp)^2}{m_e} \right) + E_{bg} - E = 0. \quad (5.5)$$

Representing expression (5) as a quadratic polynomial in \mathbf{k}_i gives:

$$\frac{\hbar^2(m_e + m_h)k_i^2}{2m_h m_e} + \frac{\hbar^2(\mathbf{k}_i \cdot \mathbf{s} + \mathbf{k}_i \cdot \mathbf{q}_\perp + \mathbf{s} \cdot \mathbf{q}_\perp)}{m_e} + \frac{\hbar^2(s^2 + q_\perp^2)}{2m_e} + E_{bg} - E = 0. \quad (5.6)$$

Considering that φ is an angle between vectors \mathbf{k}_i and \mathbf{q}_\perp , ξ is an angle between \mathbf{k}_i and \mathbf{s} and τ is an angle between \mathbf{s} and \mathbf{q}_\perp equation (5.6) becomes:

$$\frac{\hbar^2(m_e + m_h)k_i^2}{2m_h m_e} + \frac{\hbar^2(k_i s \cos(\xi) + k_i q_{\perp} \cos(\varphi) + s q_{\perp} \cos(\tau))}{m_e} + \frac{\hbar^2(s^2 + q_{\perp}^2)}{2m_e} + E_{bg} - E = 0. \quad (5.7)$$

For simplicity the following substitutions can be made:

$$a = \frac{\hbar^2(m_e + m_h)}{2m_h m_e}; \quad (5.8)$$

$$b = \frac{\hbar^2(s \cos(\xi) + q \cos(\varphi))}{m_e}, \quad (5.9)$$

$$c = \frac{\hbar^2(s^2 + 2s q_{\perp} \cos(\tau) + q_{\perp}^2)}{2m_e} + E_{bg}. \quad (5.10)$$

Now, (5.7) simplifies to a quadratic polynomial referring to k_i as just k further on:

$$ak^2 + bk + c - E = 0. \quad (5.11)$$

Solving equation (5.11) we get two solutions for k :

$$k = \frac{-b \pm \sqrt{b^2 - 4a(c - E)}}{2a}. \quad (5.12)$$

The volume density of states for the 3D k -space for this parabolic dispersion will be equal to:

$$\rho = \frac{k^3}{3\pi^2} = \frac{(-b \pm \sqrt{b^2 - 4a(c - E)})^3}{16\pi^2 a^3}, \quad (5.13)$$

and JDOS:

$$JDOS = \frac{\partial \rho}{\partial E} = \frac{(-b \pm \sqrt{b^2 - 4a(c - E)})^2}{4a^2 \pi^2 \sqrt{b^2 - 4a(c - E)}}. \quad (5.14)$$

From this, the inelastic scattering factor can be computed numerically by taking into account all possible orientations of the initial momentum \mathbf{k}_i with respect to \mathbf{q}_{\perp} and \mathbf{s} . For this computation we choose to keep $\tau=0$ as \mathbf{q}_{\perp} and \mathbf{s} are chosen parallel in our experiment. The result of a numerical computation is presented in figure 5.2.

$$\frac{df}{dE}(\mathbf{q}_{\perp}, E) = \iint_{\varphi, \xi} JDOS(\mathbf{k}, \mathbf{q}_{\perp}, E). \quad (5.15)$$

From this we can write the EELS double differential scattering cross section in dipole approximation as [181,182]:

$$\frac{\partial^2 \sigma}{\partial \Omega \partial E} \propto \frac{1}{q_{\perp}^2 + q_E^2} \frac{df}{dE}(\mathbf{q}_{\perp}, E) = \frac{1}{k_0(\theta^2 + \theta_E^2)} \frac{df}{dE}(\mathbf{q}_{\perp}, E), \quad (5.16)$$

with scattering angle $\theta = \frac{q_{\perp}}{k_0}$, linear momentum $k_0 = \frac{2\pi}{\lambda}$ and characteristic scattering angle $\theta_E = \frac{E}{2E_0}$ neglecting relativistic corrections [188].

In order to get the full EELS spectrum, we need to integrate over the allowed \mathbf{q}_{\perp} vectors as:

$$\frac{\partial \sigma}{\partial E} = \iint_A \frac{\partial^2 \sigma}{\partial \Omega \partial E} \frac{q_{\perp}}{k_0^2} d\mathbf{q}_{\perp}, \quad (5.17)$$

where A is the area of the entrance aperture of the spectrometer centred around the chosen scattering vector $\mathbf{q}_{\perp 0} = \langle \mathbf{k}'_{\perp} \rangle - \langle \mathbf{k}_{0\perp} \rangle$, comprising vectors \mathbf{q}_{\perp} such that $|\mathbf{q}_{\perp} - \mathbf{q}_{\perp 0}| < \sqrt{\alpha^2 + \beta^2} k_0$.

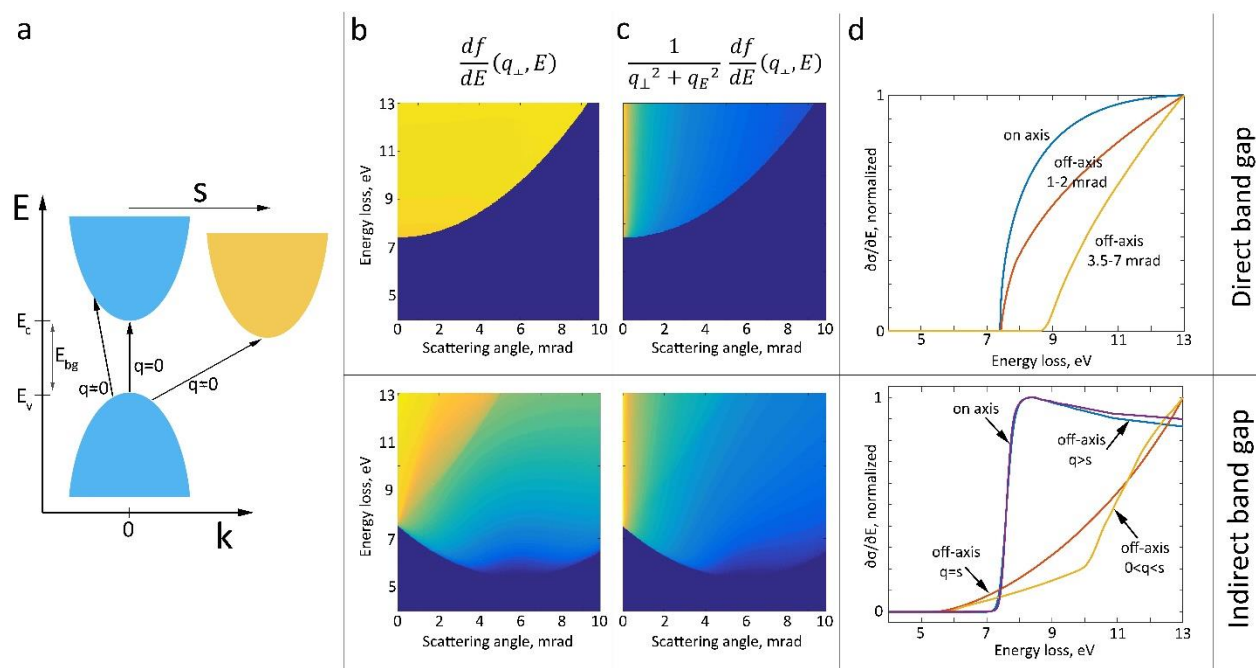


Figure 5.2 a. A two-band model for excitations in a material assuming two parabolic bands. An indirect band gap model is obtained by shifting the conduction band by a vector s . b. inelastic scattering factor dependence on the perpendicular component of the momentum transfer q_{\perp} (shown through the scattering angle $\theta = \frac{q_{\perp}}{k_0}$) calculated for the model for either $s=0$ (left side, representing a direct band gap material) or for $s=8.8 \cdot 10^9$ 1/m and $q_{\perp} \parallel s$ (right side, representing an indirect band gap material). c. Simulation of the double differential EELS cross-section for different $q_{\perp} \parallel s$. The Lorentzian distribution of the inelastic scattering is clearly visible and prefers transitions close to $q=0$. Selecting a specific scattering angle, however allows us to select only the weakly scattering part which still contains the signature of the indirect gap (d). d. Simulated EELS spectra extracted from (c) for different choices of q_{\perp} . Note that in case of direct band gap the onsets shift towards higher values when increasing the selected q_{\perp} while the shape of the onset changes. In case of an indirect band gap (left) we successfully probe it by selecting q_{\perp} transfers close to s , but attention needs to be paid to obtain enough momentum space resolution to avoid bias towards lower q_{\perp} values through the Lorentzian.

For on-axis setups, the EELS spectrum is dominated by q -transfers in the range of q_{\parallel} due to the Lorentzian envelope as shown in (fig. 5.2c). For off-axis acquisition ($q_{\perp 0} \gg q_{\parallel}$), a range of off-axis q_{\perp} vectors is selected leading to a strong reduction of the signal due to the Lorentzian factor, but now q_{\perp} vectors that are excluded in the on-axis case could be selectively detected as shown in fig. 5.2d. According to the theoretical work of Rafferty and Brown [179] and noting that Tauc plots

[180] are sometimes applied to EELS data [189], the JDOS for a direct transition should be described by the function $a(E - E_g)^n$ with $n = 0.5$ and for indirect transition $n = 1.5$. Clearly visible even in this simple model is that the correct value of the indirect band gap is obtained when $q_{\perp} = s$. The simulation also proves that a good momentum resolution is crucial to accurately measure the indirect band gap. Shifting q_{\perp} towards lower values changes the band gap onset substantially towards higher values and the spectrum obtains a more direct band gap-like shape.

Choosing q_{\perp} in between direct and indirect transitions also lifts the gap onset and results in a flatter shape of the onset region. It is also important to highlight that according to our simulations the value of n varies depending on q_{\perp} selection which can be understood as ranging from more direct-like ($n \sim 0.5$) to more indirect-like behavior ($n \sim 1.5$).

Results and discussion

We attempt to experimentally demonstrate statement (6) on a single crystal diamond film in [110] crystallographic orientation by taking spectra with the EELS spectrometer entrance shifted at different points of the first BZ. The spectra were acquired at 80 keV acceleration voltage, with $\alpha = 1$ mrad, $\beta = 1.2$ mrad and energy resolution 120 meV. This leads to a fractional momentum resolution of 0.13 or the range of momentum transfer q_{\perp} of $2.35 \cdot 10^9$ 1/m with the boundaries of the 1st BZ being at $17.6 \cdot 10^9$ 1/m from Γ to X point.

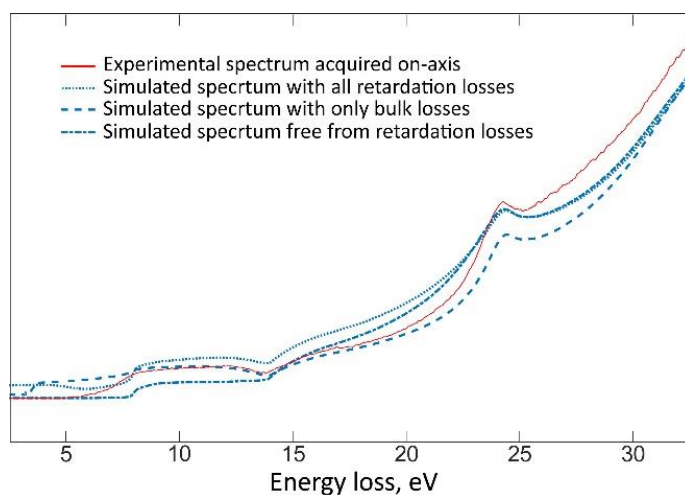


Figure 5.3 Comparison between the experimental spectrum acquired on-axis (red) and simulated spectra (blue) with or without retardation losses calculated for 80 keV, sample thickness of 50 nm and collection angle 1.2 mrad making use of Kröger equation and a tabulated diamond dielectric function ⁸.

The chosen acceleration voltage is sometimes, considered safe for obtaining the spectrum without parasitic losses. However, diamond has a high refractive index and can still cause the unwanted losses. The amount of retardation losses in the diamond sample at 80 keV was estimated through comparison of the experimental spectrum acquired on-axis (therefore, containing all possible retardation losses) and the spectra simulated with the Kröger equation. As can be seen

from the figure 5.3, parasitic losses are present in the experimental spectrum and can be attributed both to Cherenkov radiation and surface light-guided modes.

Four spectra are obtained along the Δ line of the first BZ and show the expected behavior (figure 5.4b). The spectrum taken on-axis in (000) or in the Γ point shows an onset below 5 eV which relates to retardation losses and cannot be used to estimate the true band gap value [190].

All spectra obtained off-axis are free from retardation losses. To quantitatively estimate the band gap onsets from these spectra, we fitted the loss region with the function $I(E) = a(E - E_g)^n$ convoluted with the ZLP of each spectrum making use of the procedures suggested in the literature [191]. The convolution procedure helps to take into account all the parameters which influence the shape of the spectra such as energy resolution, asymmetry of the zero loss peak *etc.* and allows to estimate the band gap onset more precisely. As mentioned in the previous part, EELS cross-section for a direct transition should be described by the function $a(E - E_g)^n$ with $n = 0.5$ for direct and 1.5 for indirect band gaps according to the simple two band model. Experimental spectra will deviate from these values of n due to, for example, the Lorentzian dependence of double differential cross-section of EELS on inelastic scattering angle which causes a bias in the inelastic scattering factor (see equation (5.16)) and figure 5.2c) and a finite momentum resolution which makes selection of a pure direct or indirect band gap transition impossible. As our simulations show, selection of different ranges of q_{\perp} also influences the band gap onset (figure 5.2d). Therefore, the most reasonable approach to estimate the band gap onset in case of experimental datasets is to leave n as a free parameter for fitting and then qualitatively label the measured transition as more 'direct' or 'indirect'.

The resulting fit values of spectral onset E_g and n for each experimental spectra acquired at a set of points in the first BZ (figure 5.1c) are given in the table 1. The first spectrum was obtained with the spectrometer entrance placed on the Δ line between Γ and X points with the length q_{\perp} smaller than required for the indirect band gap transition (see figure 5.1). The fitted value of band gap onset which has clearly indirect character is -5.9 which corresponds to the band gap values in between the direct and indirect transitions on the Δ line.

The second spectrum was taken at the point of the BZ corresponding to the lowest position of the conduction band and, therefore, selecting the indirect band gap transition. The fitted band gap value is -5.6 eV which agrees well with the accepted value for the indirect band gap of diamond [89] and n is estimated as 1.1.

When further shifting the spectrometer entrance away from (000) along the Δ direction to the X point of the BZ we observe an unusual shape of the band gap onset which corresponds to the signature of a direct rather than indirect transition and the best fit is obtained at $n \sim 0.66$. The fitted value of this band gap onset is -6.2 eV. This shape might be explained by the constructive interference of the four inelastic paths due to the position of the X point symmetrical to the four CBED reflexes (figure 5.1d) which serve as sources for inelastic scattering.

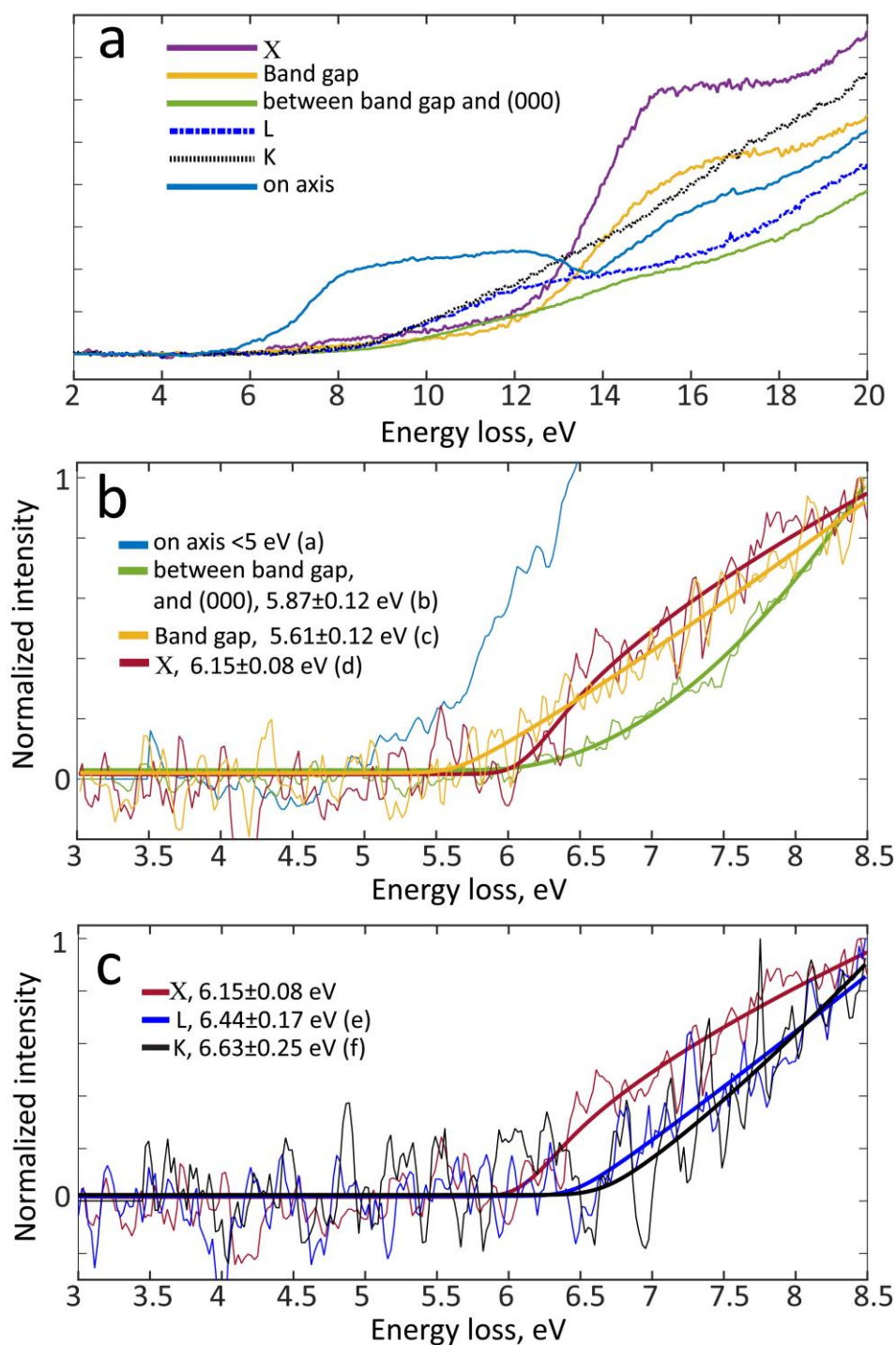


Figure 5.4. a. Experimental spectra obtained at certain points in the first BZ of diamond marked in figure 5.1. b. Experimental spectra obtained on the Δ direction in the first BZ of diamond fitted with $I(E) = a(E - E_{bg})^n$. c. Experimental spectra acquired at the main points of the first BZ of diamond and fitted the same way as (b). Letters a-f correspond to the positions marked at figure 5.1d where the spectra were acquired.

Table 5.1. Parameters of fitting experimental data with the function $I(E) = a(E - E_g)^n$ convoluted with the ZLP where E_g is the onset of the spectra. The spectra are demonstrated in figure 5.4. Error bars are based on an asymptotic normal distribution for the estimates from a nonlinear least square fit.

Point in BZ	Before band gap	Band gap	X	K	L
E_g , eV	5.87±0.12	5.61±0.12	6.15±0.08	6.63±0.25	6.44±0.17
n	2.0	1.1	0.66	1.2	1.1

The behavior of spectra taken at the other main points of the analyzed slice of the BZ agrees with the statement (6) in the experiment section. Even with approximately the same length of momentum transfer q_{\perp} the spectra obtained at L and K points are different from the ones acquired at X or the indirect band gap points. The onsets for L and K are close to the typical indirect behavior and estimated to be approximately 6.4 eV and 6.6 eV respectively, being far above the onsets for X or indirect band gap points placed at the Δ direction of the BZ. This proves the possibility to probe the band structure at different points and even partly reconstruct the lower surface of the conduction band if we assume that the shortest transitions always originate from the Γ point. This is possible in diamond due to the presence of an isolated global maximum of the valence band around the Γ point, causing transitions from different states to have a significantly higher energy.

Applying to the other materials this proposition should be taken with care as the bands can be flatter and transition from, for example, Γ to K point might have the same length as some intermediate transition and different initial states will complicate the reconstruction of the conduction band as the shape of both valence and conduction band will contribute to shape the JDOS. Nevertheless, the experimental measurement of the indirect band gap should always be possible as the shortest global transition always originates from Γ point.

Signal to noise ratio remains an open issue when acquiring spectra far outside the CBED disks. The current results show, that acceptable signal levels can be obtained and progress in single electron detectors, is providing an attractive route to further improve the signal to noise ratio and open a new era of band structure studies with EELS in TEM [192].

Conclusions

In this chapter we have shown a simple way to deliberately measure the indirect band gap of diamond and also probe the energy of other transitions in the diamond band structure with EELS. It opens an interesting possibility to partly reconstruct the band structure of materials using EELS. If the band structure is unknown the suggested method can be used to estimate the position and energy of the indirect or direct band gap transitions by analyzing only a part of the first Brillouin zone which should include the points sufficient for further extrapolation. EELS can allow to analyze the band structure not only at the surface, as most other techniques, but also at a chosen place in the bulk material by preparing a targeted specimen or e.g. from an individual nanoparticle. EELS has already proven to be able to map the direct band gaps with nanometer resolution [94,95,191]. This can be extended to indirect band gaps and can help to link the structure of, for instance, indirect semiconductors with defects, strain or impurities to the properties of their band structure.

Chapter 6. Future prospects

In the last chapter a few hints are given on the possibility to partly reconstruct the band structure of diamond and other materials by measuring the energy loss and the direction of the momentum transfer of the transition from the valence to the conduction band with EELS. As mentioned before, low loss EELS to first approximation represents only the joint density of states limiting the possibility to fully reconstruct the band structure. The retrieval of a single band, like in angle-resolved photoemission spectroscopy (ARPES), seems unfeasible with current understanding of the method.

However, by measuring the minimum energy gap between valence and conduction bands the energy surface which may be referred as a '*band gap surface*', can be estimated from the EELS data. This surface would represent the energy and direction in reciprocal k -space of the transitions from the highest point¹ of the valence band (usually the Γ point) to the lowest points of the conduction band.

Experiment on partial reconstruction of the band structure

The energy and direction of every transition within the first Brillouin zone initiating from the Γ point can be obtained in a simple STEM-EELS experiment described in the chapter 5. In this set-up the spectrometer entrance is placed in the same plane as the CBED pattern. By shifting the pattern over the fixed entrance aperture, the energy loss spectrum for every relative position of the CBED and the spectrometer entrance aperture can be obtained. Taking advantage of the fact that most of the interband transitions in this set-up are acquired from a very thin slice of a first BZ (about q_{\parallel} or $1/160$ of the first BZ), the coordinates of the band gap surface can be determined from a distance and direction between the (000) reflection (Γ point) and the position of the spectrometer entrance² (basically, q_{\perp} momentum resolution). The band gap onset of the spectrum acquired at each position of the spectrometer entrance, determines the minimum energy of the transition. To retrieve the band gap surface for all the possible transitions, one should map a few 'slices' of the first BZ, containing all main symmetry points.

The main experimental challenge comes from the fact that the position of the spectrometer is static and only CBED pattern can be moved with accordance to it. This is manually possible with diffraction shift control of the microscope, making the scanning tedious for large datasets. An automated scanning procedure is not conventional and not implemented in current instruments. Development of such an automated movement of the diffraction plane is a very important task for the future research in this direction in terms of reducing the acquisition time and avoiding mistakes of the operator.

Another difficulty lays in the weak signal outside the Bragg reflections due to Lorentzian dependence of EELS intensity on the scattering angle. This can be addressed by setting very high exposure times which is not always optimal due to the sample damage. Very sensitive single electron detectors such as the Medipix Merlin or Gatan K2 could help to reduce the exposure time

¹ If we assume that all transitions with minimum energy initiate from the Γ point or any other highest point in the valence band, then all the momentum transfers \mathbf{q} can be considered as coordinates \mathbf{k} of the reciprocal space with zero at this highest point.

² Note that this is valid only within the first BZ. The transitions coming from other Bragg reflections will impact the signal outside the boundaries of the first BZ.

Chapter 6. Future prospects

and solve this issue in the future. However, diamond is a good testing material as it can withstand relatively high electron dose (see chapter 3).

The first attempt to reconstruct the band gap surface for one slice of the first BZ was done at 80 keV for a diamond sample oriented in [011] zone axis parallel to the primary electron beam. In this specific orientation the first BZ of diamond is sliced with a plane containing a few major symmetry points, such as Γ , X, L, U, K (see chapter 5). The reciprocal space was mapped in between $(\bar{1}\bar{1}\bar{1})$, (200), $(11\bar{1})$ and (000) CBED reflections in order to collect all mentioned symmetry points. The experimental conditions were similar to the ones used in the previous chapter with the convergence angle $\alpha=1$ mrad, collection angle $\beta=1.2$ mrad and fractional momentum resolution of 0.13.

The x and y axis of the obtained datacube represent the coordinates of the reciprocal space with zero at the Γ point. The z axis contains the energy loss spectrum for every k_x and k_y . This datacube can be analyzed in different ways in order to obtain the band gap surface. The most conventional way described in chapter 5, is to determine the band gap onset for every spectrum by fitting it with the function $I(E) = a(E - E_g)^n$. However, this approach did not give the meaningful results due to the weak signal to noise ratio¹.

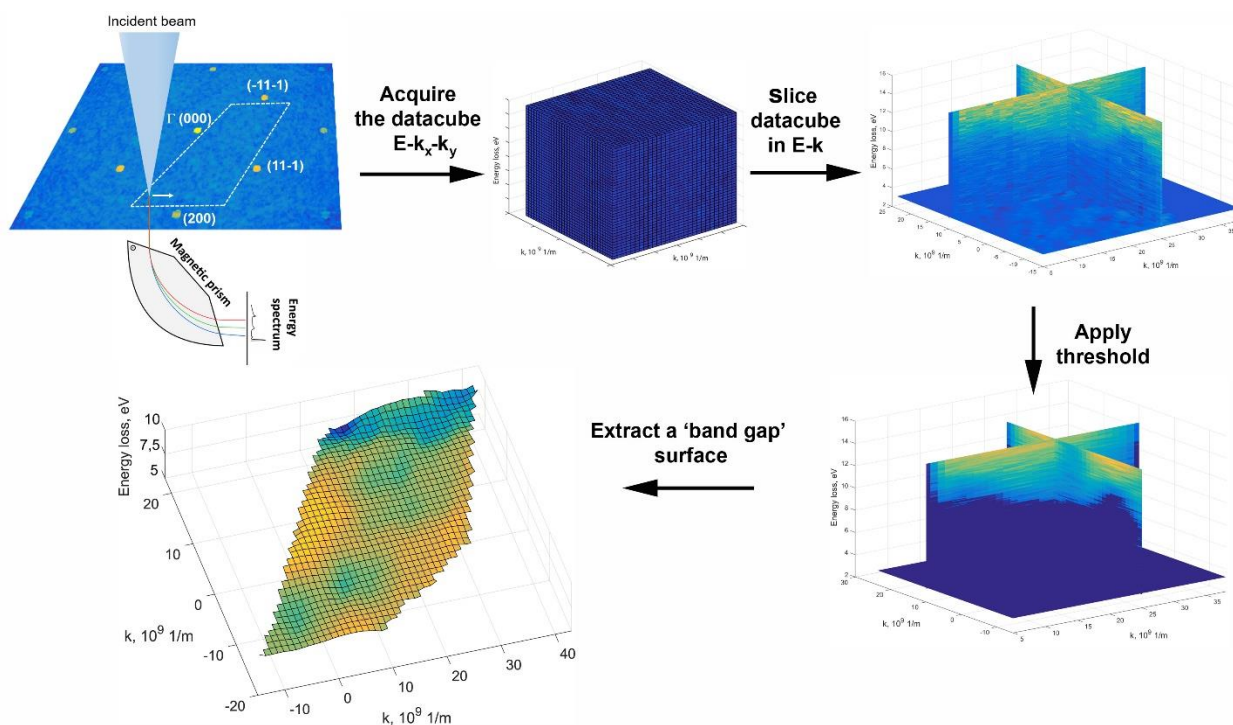


Figure 6.1. Step by step description of the retrieval of the band gap surface of diamond.

Another way to approach the data analysis provided more insights. The datacube can be sliced perpendicular to the k -plane showing the possible changes in the intensity of the spectra

¹ Note that the spectra of different indirect transitions presented in chapter 5 were acquired for about 10 minutes each. Current dataset (29x35) would require approximately 170 hours with this exposure time.

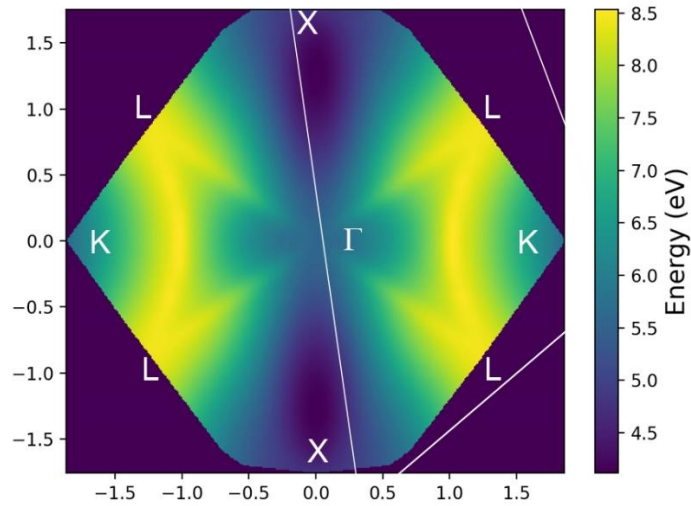
Chapter 6. Future prospects

along one direction of k (see figure 6). In order to avoid the Lorentzian dependence of EELS signal on q , each spectrum with removed ZLP was normalized by its total intensity. From one slice (figure 6.1) one can clearly see the difference between the background level and the signal from interband transitions together with the evident change in the band gap onset along the chosen direction of k . By applying a threshold level which was taken as a constant for the whole dataset, the background was removed showing the change in the band gap onset even clearer. The sum of this dataset in energy z direction from 5 to 10 eV resulted in the JDOS projected over wave vector k . As only small energy region was taken, the JDOS can be considered as a band gap surface presented at the figures 6.1 and 6.2.

The obtained surface has a few regions with lower band gap values displayed with darker blue color and some brighter areas with higher transition energies. To evaluate the experimental results, a simulated band gap surface was obtained by calculating the shortest transitions from the Γ point in the valence band to the lowest unoccupied states in the conduction band retrieved only for the reciprocal points laying in the [110] plane of the first diamond BZ, hereby approximating the simulation to the experiment. The simulated surface has two main valleys between Γ and two symmetrical X points representing the lowest possible transitions in the band structure of diamond (see figure 6.3). The bright yellow lines connecting Γ and four symmetrical L points represent the highest energies of band gap transitions which are also displayed in a more conventional 'walk in k -space' plot on figure 6.3. Two symmetrical K points show the second local minimum of the band gap transitions from the Γ point.

A few similarities can be found between the experimental and simulated band gap surfaces. The experimental map also has the lowest energy in between Γ and X points. The experiment agrees with the simulated results as well by showing high energies of transitions in between Γ and two symmetrical L points. Interestingly enough, there are another two visible lines representing higher energies of transitions which are not present in the simulation. This effect could be related to the elastic scattering of already inelastically scattered electrons which could form interference regions at specific energy losses [193]. The energy values just around Γ point could be affected by the retardation losses or/and elastic scattering which can modify the distribution of inelastic scattering [194], particularly in thicker samples. This could cause artefacts and explain slightly higher values of the interband transitions around this point than expected. The finite momentum resolution which smears out the transitions and/or the fact that for the high energy transitions there could be a few with the same length and direction but initiating from the different points, could also cause the deviation of the experiment from the simulation. However, the last issue will not affect the lowest transitions which were of most interest here.

Simulated 'band gap surface' for diamond in [110] orientation



Experimental 'band gap surface' for diamond in [110] orientation

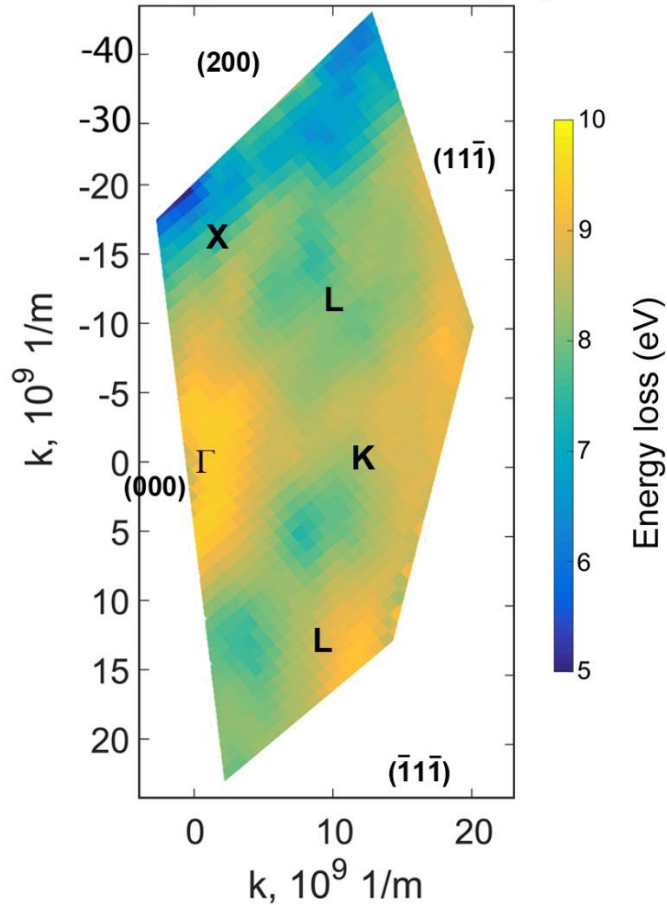


Figure 6.2. Possible interpretation of the experimental band gap surface.

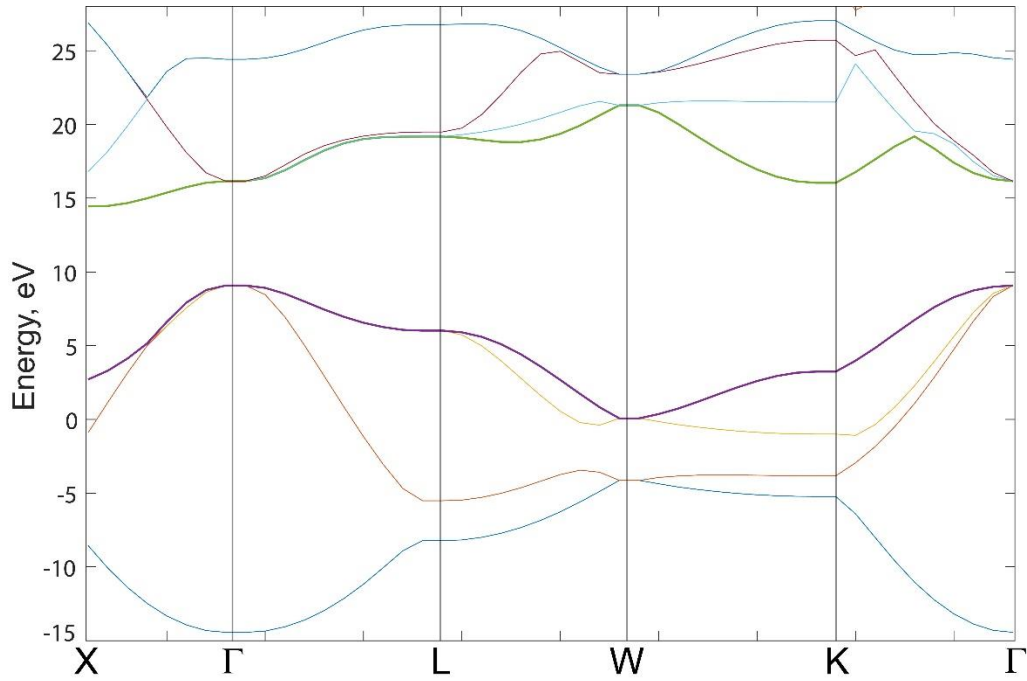


Figure 6.3. The band structure of diamond [195].

The band structure of diamond from the figure 6.3 can be compared with the experiment, by assuming once more that all the shortest transitions originate from the Γ point of the valence band. This means that the JDOS for the lowest energy transitions could be represented as a convolution of the lowest unoccupied states with the single peak at the Γ point. This will result in a JDOS of the lowest energy transitions shaped as a lowest conduction band. The comparison between simulated and experimental JDOS for two directions in the first BZ of diamond, Γ -X and Γ -L, is shown in the figure 6.4. In general, the experimental plots demonstrate the same behavior as the simulated plots. The energy of states decreases from Γ to X point and increases from Γ to L point both in the experiment and simulation. The higher than expected energies of the interband transitions at the Γ point in the experimental plots are possibly caused by the effects related to elastic scattering which as mentioned above, could modify the distribution of inelastic electrons.

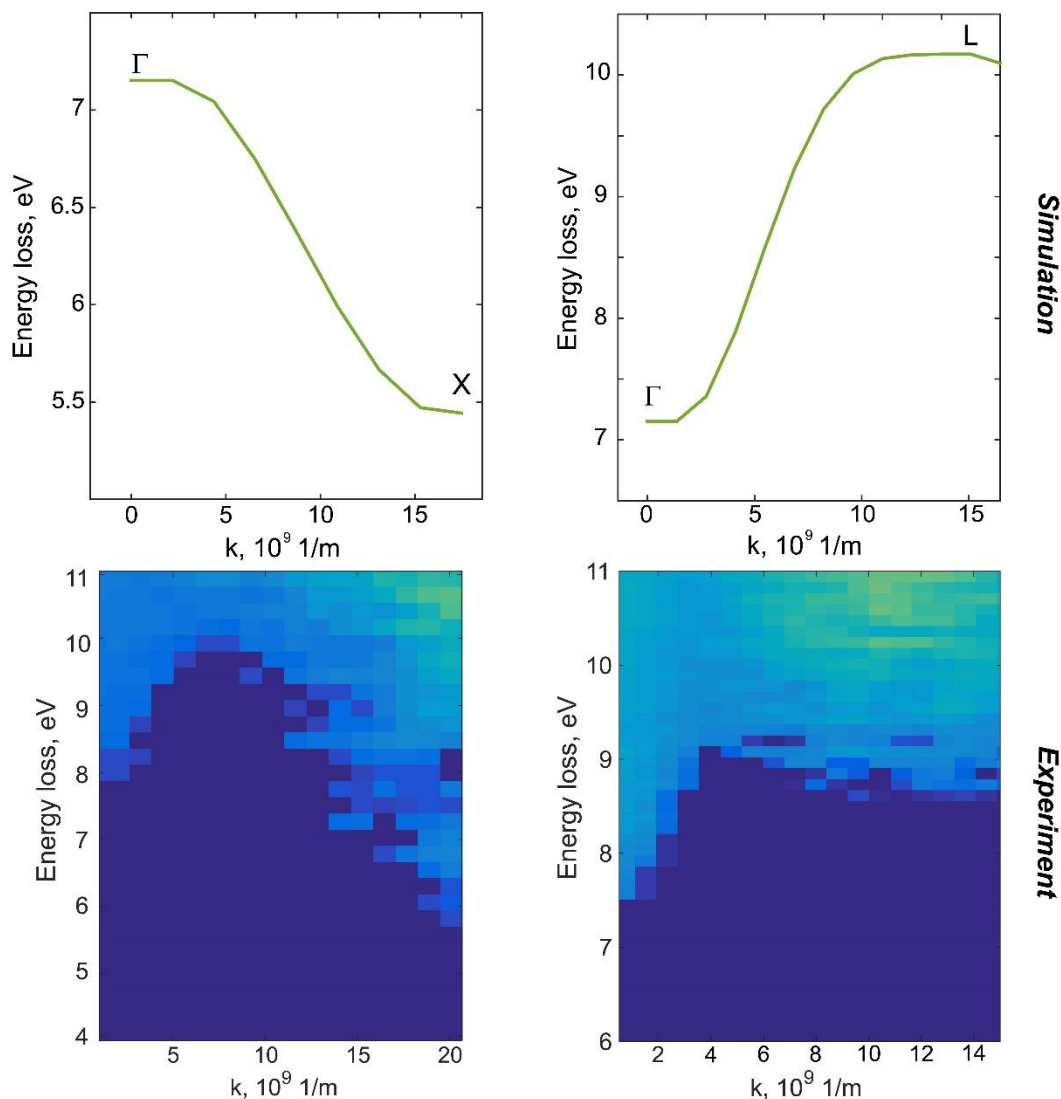


Figure 6.4. Comparison of simulated and experimental JDOS (obtained only for the shortest transitions) for Γ -X direction (left) and Γ -L direction (right) in the BZ zone of diamond.

Conclusions

The experimental results are promising and demonstrate that the method could become a powerful tool to study the band structure of materials with nanometer resolution. The data also shows that the full reconstruction of the band gap surface in 3D is, in principle, possible and can be accomplished by mapping a few additional slices of the first BZ which contain other main symmetry points. For the future, more data on different materials is required to properly test this technique. Also, technical improvements, such as introduction of the automated diffraction shifts, are necessary in order to make this method more feasible and accessible.

General conclusions

This work is dedicated to the investigation of diamond materials, natural and artificial, by means of transmission electron microscopy and electron energy loss spectroscopy. We show the capability of TEM to answer multiple questions of material characterization, from the microstructure and composition in the first part of the thesis, to dielectric properties and band gaps in the second part.

We give an overview on the variety of diamond materials and TEM techniques, well-established and new, in the introductory chapter. In the second chapter we show how state-of-the-art TEM can characterize novel diamond based materials and explain how their atomic structure and compositions impact the macroscopic properties. The first characterized material is a nanocomposite of hexagonal boron nitride and polycrystalline diamond for large-area field emitters. The reason behind superior field emitting properties of this combination was revealed with the help of TEM and based on the direct growth of the hexagonal phase of BN on the diamond surface. The mechanism of this growth was suggested as well. The second studied material is a diamond layer grown by the novel CVD method at low temperatures of about 400 °C. High resolution TEM, EELS and EDX data helped to suggest three mechanisms of the unusual plate-like morphology of this layer. All three mechanisms are based on the presence of the impurity atoms (such as Si) which, in the first mechanism, cause the formation of the fullerenes at the early stages of CVD growth further creating stacking faults which, in large amounts, modify the morphology. Two other mechanisms are based on either inhibiting or selective etching of one of the crystal planes by the impurity.

The third chapter proposes a solution to the structure of a famous platelet defect in natural diamond that was studied for decades. With improved spatial resolution of aberration-corrected microscope, it was finally possible to directly image the internal structure of the defect and suggest the consistent model for this defect. The image processing techniques used in this chapter also helped to create the correct model by reducing the noise level and estimate the atomic positions with high accuracy.

The second part of the thesis from chapter 4 to 6 step-by-step develops the idea on measuring the band gaps of diamond and other materials. In chapter four we show how to avoid the retardation losses, such as Cherenkov radiation and collect a clean band gap signal with a simple STEM-EELS set-up using a ring (Bessel) aperture. The retardation losses are contained in a narrow solid angle around Bragg reflections. They can be avoided by collecting the spectra outside these reflections. The Bessel aperture in the condenser plane creates ring shaped reflections in the diffraction plane and the spectrometer entrance can be put inside this ring, collecting only the retardation-free signal and also averaging the possible anisotropy. We bring the attention to the importance of the correct experimental settings, such as convergence and collection angle. Compared to other works dedicated to this topic, we also investigate the influence of momentum transfer on the band gap. On a simple model consisting of two parabolic bands we show how the deviation from the correct parameters can lead to the wrong band gap onsets.

General conclusions

Making use of the non-zero momentum transfer in EELS, in chapter 5 we measure the indirect band gap of diamond and other indirect transitions in the diamond band structure. We highlight the importance of the good momentum resolution in EELS in order to obtain the correct value of the indirect band gap supported by the simulations on a similar two parabolic band model.

In the last chapter we show the first results on the partial reconstruction of the band structure of diamond which are in reasonable agreement with simulations. Further development of this method could provide a nice tool to study the lowest transitions in the band structure and obtain a 'band gap' energy surface. The advantage of this technique over other techniques is spatial resolution and the possibility to select and investigate the exact object, for instance, a nanoparticle, or a precise layer in the semiconductor, by preparing TEM sample from the bulk. We also believe that this work gives more understanding on the band gap measurements with EELS and makes this method more feasible.

List of scientific contributions

List of publications:

1. S. Korneychuk, B. Partoens, G. Guzzinati, R. Ramaneti, J. Derluyn, K. Haenen, J. Verbeeck, Exploring possibilities of band gap measurement with off-axis EELS in TEM, *Ultramicroscopy*. 189 (2018) 76-84. doi:10.1016/j.ultramic.2018.03.021.
2. S. Korneychuk, G. Guzzinati, J. Verbeeck, Measurement of the indirect band gap of diamond with EELS in TEM, *Phys. Status Solidi (A)*, in press (2018), doi:10.1002/pssa.201800318.
3. S. Deshmukh, K.J. Sankaran, K. Srinivasu, S. Korneychuk, D. Banerjee, A. Barman, G. Bhattacharya, D.M. Phase, M. Gupta, J. Verbeeck, K.C. Leou, I.N. Lin, K. Haenen, S.S. Roy, Local probing of the enhanced field electron emission of vertically aligned nitrogen-doped diamond nanorods and their plasma illumination properties, *Diam. Relat. Mater.* 83 (2018) 118–125. doi:10.1016/j.diamond.2018.02.005.
4. S. Deshmukh, K.J. Sankaran, S. Korneychuk, J. Verbeeck, J. Mclaughlin, K. Haenen, S.S. Roy, Nanostructured nitrogen doped diamond for the detection of toxic metal ions, *Electrochim. Acta*. 283 (2018) 1871–1878. doi:10.1016/j.electacta.2018.07.067.
5. Y. Zhou, R. Ramaneti, J. Anaya, S. Korneychuk, J. Derluyn, H. Sun, J. Pomeroy, J. Verbeeck, K. Haenen, M. Kuball, Thermal characterization of polycrystalline diamond thin film heat spreaders grown on GaN HEMTs, *Appl. Phys. Lett.* 111 (2017). doi:10.1063/1.4995407.
6. S. Drijkoningen, P. Pobedinskas, S. Korneychuk, A. Momot, Y. Balasubramaniam, M.K. Van Bael, S. Turner, J. Verbeeck, M. Nesládek, K. Haenen, On the Origin of Diamond Plates Deposited at Low Temperature, *Cryst. Growth Des.* 17 (2017) 4306–4314. doi:10.1021/acs.cgd.7b00623.
7. D.Q. Hoang, S. Korneychuk, K.J. Sankaran, P. Pobedinskas, S. Drijkoningen, S. Turner, M.K. Van Bael, J. Verbeeck, S.S. Nicley, K. Haenen, Direct nucleation of hexagonal boron nitride on diamond: Crystalline properties of hBN nanowalls, *Acta Mater.* 127 (2017) 17–24. doi:10.1016/j.actamat.2017.01.002.
8. R. Ramaneti, K.J. Sankaran, S. Korneychuk, C.J. Yeh, G. Degutis, K.C. Leou, J. Verbeeck, M.K. Van Bael, I.N. Lin, K. Haenen, Vertically aligned diamond-graphite hybrid nanorod arrays with superior field electron emission properties, *APL Mater.* 5 (2017). doi:10.1063/1.4985107.

List of scientific contributions

9. S. Turner, H. Idrissi, A.F. Sartori, S. Korneychuk, Y.-G. Lu, J. Verbeeck, M. Schreck, G. Van Tendeloo, Direct imaging of boron segregation at dislocations in B:diamond heteroepitaxial films, *Nanoscale*. 8 (2016) 2212–2218. doi:10.1039/C5NR07535A.
10. K.J. Sankaran, D.Q. Hoang, S. Kunuku, S. Korneychuk, S. Turner, P. Pobedinskas, S. Drijkoningen, M.K. Van Bael, J. D'Haen, J. Verbeeck, K.C. Leou, I.N. Lin, K. Haenen, Enhanced optoelectronic performances of vertically aligned hexagonal boron nitride nanowalls-nanocrystalline diamond heterostructures, *Sci. Rep.* 6 (2016) 1–11. doi:10.1038/srep29444.
11. K.J. Sankaran, D.Q. Hoang, S. Korneychuk, S. Kunuku, J.P. Thomas, P. Pobedinskas, S. Drijkoningen, M.K. Van Bael, J. D'Haen, J. Verbeeck, K.-C. Leou, K.T. Leung, I.-N. Lin, K. Haenen, Hierarchical hexagonal boron nitride nanowall–diamond nanorod heterostructures with enhanced optoelectronic performance, *RSC Adv.* 6 (2016) 90338–90346. doi:10.1039/C6RA19596B.
12. K.J. Sankaran, D.Q. Hoang, K. Srinivasu, S. Korneychuk, S. Turner, S. Drijkoningen, P. Pobedinskas, J. Verbeeck, K.C. Leou, I.N. Lin, K. Haenen, Engineering the interface characteristics on the enhancement of field electron emission properties of vertically aligned hexagonal boron nitride nanowalls, *Phys. Status Solidi Appl. Mater. Sci.* 213 (2016) 2654–2661. doi:10.1002/pssa.201600233.
13. E.A. Ekimov, O.S. Kudryavtsev, S. Turner, S. Korneychuk, V.P. Sirotinkin, T.A. Dolenko, A.M. Vervalde, I.I. Vlasov, The effect of molecular structure of organic compound on the direct high-pressure synthesis of boron-doped nanodiamond, *Phys. Status Solidi.* 213 (2016) 2582–2589. doi:10.1002/pssa.201600181.

Conferences:

- Hasselt Diamond Workshop, SBDD XXI.
Poster presentation: 'Direct visualisation of the nitrogen platelet structure in natural Ia diamonds by ADF-STEM'. Svetlana Korneychuk, Stuart Turner, Artem Abakumov, Alexey Bosak, Jo Verbeeck. Hasselt, Belgium, March 9-11, 2016.
- The 16th European Microscopy Congress EMC 2016.
Poster presentation: 'Determination of the platelet structure in natural diamond by ADF-STEM'. Svetlana Korneychuk, Stuart Turner, Artem Abakumov, Alexey Bosak, Jo Verbeeck. Lyon, France, 28 August - 2 September 2016.
- Hasselt Diamond Workshop, SBDD XXII.
Oral presentation: 'Band gap measurements of diamond materials with EELS using electron Bessel beams'. Svetlana Korneychuk, Rajesh Ramaneti, Yan Zhou, Julian Anaya, Paulius

List of scientific contributions

Pobedinskas, Joff Derluyn, Huarui Sun, James Pomeroy, Ken Haenen, Martin Kuball, Johan Verbeeck. Hasselt, Belgium, March 8-10, 2017.

- 13th Multinational Congress on Microscopy
Oral presentation: 'Measuring band gaps of semiconductors by off-axis EELS with Bessel aperture'. Svetlana Korneychuk, Giulio Guzzinati, Rajesh Ramaneti, Paulius Pobedinskas, Joff Derluyn, Ken Haenen, Johan Verbeeck. Rovinj, Croatia September 24-29, 2017.
- Hasselt Diamond Workshop, SBDD XXIII.
Poster presentation: 'Exploring possibilities of band gap measurement with off-axis EELS in TEM'. Svetlana Korneychuk, Bart Partoens, Giulio Guzzinati, Rajesh Ramaneti, Joff Derluyn, Ken Haenen and Jo Verbeeck. Hasselt, Belgium, March 7-9, 2018.

Bibliography

1. Hirsch, A. The era of carbon allotropes. *Nat. Mater.* **9**, 868–871 (2010).
2. Fischer-Cripps, A. C. *Nanoindentation*. (Springer, 2004).
3. Broda, A. *et al.* Highly efficient heat extraction by double diamond heat-spreaders applied to a vertical external cavity surface-emitting laser. *Opt. Quantum Electron.* **49**, 1–7 (2017).
4. John, P., Polwart, N., Troupe, C. E. & Wilson, J. I. B. The oxidation of (100) textured diamond. *Diam. Relat. Mater.* **11**, 861–866 (2002).
5. Davies, G. & Evans, T. Graphitization of diamond at zero pressure and at a high pressure. *Proc. R. Soc. London. A. Math. Phys. Sci.* **328**, 413 LP-427 (1972).
6. Thomas, M. E. & Tropf, W. Optical Properties of Diamond. *Johns Hopkins APL Tech. Dig.* **14**, 16–23 (1993).
7. Doherty, M. W. *et al.* The nitrogen-vacancy colour centre in diamond. *Phys. Rep.* **528**, 1–45 (2013).
8. Phillip, H. R. & Taft, E. A. Kramers-Kronig Analysis of Reflectance Data for Diamond. *Phys. Rev.* **136**, (1964).
9. Wort, C. J. H. & Balmer, R. S. Diamond as an electronic material. *Mater. Today* **11**, 22–28 (2008).
10. Isberg, J., Hammersberg, J., Johansson, E., Twitchen, D. J. & Whitehead, A. J. High Carrier Mobility in Single-Crystal Plasma-Deposited Diamond.pdf. *Science (80-.)*. **297**, 1670–1673 (2002).
11. Kohn, E. & Denisenko, A. Concepts for diamond electronics. *Thin Solid Films* **515**, 4333–4339 (2007).
12. Koizumi, S. & Watanabe, K. Ultraviolet Emission from pn Junction. *Science (80-.)*. **292**, 1899–1901 (2012).
13. Carlson, R. W. *The Mantle and Core*. (Elsevier, 2005).
14. Walker, J. Optical absorption and luminescence in diamond. *Reports Prog. Phys.* **42**, 1605 (1979).
15. Kaiser, W. & Bond, W. L. Nitrogen, a major impurity in common type I diamond. *Phys. Rev.* **115**, 857–863 (1959).
16. Robertson, R., Fox, J. J. & Martin, A. E. Two Types of Diamond. *Philos. Trans. R. Soc. London. Ser. A, Contain. Pap. a Math. or Phys. Character* **232**, 463 LP-535 (1933).
17. Mainwood, A. Nitrogen and nitrogen-vacancy complexes and their formation in diamond. *Phys. Rev. B* **49**, 7934–7941 (1994).
18. Wang, W. & Smit, K. Very Large Type Ib Natural Diamond. *Gems@Gemology* **51**, (2015).
19. Fritsch, E., Hainschwang, T., Massi, L. & Rondeau, B. *Hydrogen-Related Optical Centers in*

Bibliography

- Natural Diamond: An Update. New diamond and frontier carbon technology: an international journal on new diamond, frontier carbon and related materials* **17**, (2007).
20. Iakoubovskii, K. & Adriaenssens, G. J. Optical characterization of natural Argyle diamonds. *Diam. Relat. Mater.* **11**, 125–131 (2002).
 21. Collins, A. T. The optical and electronic properties of semiconducting diamond. *Philos. Trans. R. Soc. London. Ser. A Phys. Eng. Sci.* **342**, 233 LP-244 (1993).
 22. Iakoubovskii, K., Baker, J. M. & Newton, M. E. Electron spin resonance study of perturbed di-interstitials in diamond. *Phys. status solidi* **201**, 2516–2520 (2004).
 23. Collins, A. T., Connor, A., Ly, C. H., Shareef, A. & Spear, P. M. High-temperature annealing of optical centers in type-I diamond. *J. Appl. Phys.* **97**, (2005).
 24. Walkert, J. Optical absorption and luminescence in diamond. *Reports Prog. Phys.* **42**, 1606–1659 (1979).
 25. Raman, C. V. & Nilakantan, P. Reflection of X-rays with change of frequency- Part 11. The case of diamond. *Proc. Ind. Acad. Sci. A* **11**, 389–397 (1940).
 26. Romani, S. & Evans, J. H. Platelet defects in hydrogen implanted silicon. *Nucl. Inst. Methods Phys. Res. B* **44**, 313–317 (1990).
 27. Pailloux, F., David, M. L. & Pizzagalli, L. Quantitative HRTEM investigation of nanoplatelets. *Micron* **41**, 135–142 (2010).
 28. Bangert, U., Barnes, R., Gass, M. H., Bleloch, A. L. & Godfrey, I. S. Vacancy clusters, dislocations and brown colouration in diamond. *J. Phys. Condens. Matter* **21**, (2009).
 29. Kiflawi, I. & Bruley, J. The nitrogen aggregation sequence and the formation of voidites in diamond. *Diam. Relat. Mater.* **9**, 87–93 (2000).
 30. Zaitsev, A. M. *Optical Properties of Diamond : A Data Handbook*. (Springer, 2001).
 31. Chen, J. H., Bernaerts, D., Seo, J. W., Van Tendeloo, G. & Kagi, H. Voidites in polycrystalline natural diamond. *Philos. Mag. Lett.* **77**, 135–140 (1998).
 32. Berger, S. D. & Pennycook, S. J. Detection of nitrogen at {100} platelets in diamond. *Nature* **298**, 635–637 (1982).
 33. Fallon, P. J., Brown, L. M., Barry, J. C. & Bruley, J. Nitrogen determination and characterization in natural diamond platelets. *Philos. Mag. A Phys. Condens. Matter, Struct. Defects Mech. Prop.* **72**, 21–37 (1995).
 34. Goss, J. P. *et al.* Extended defects in diamond: The interstitial platelet. *Phys. Rev. B* **67**, 165208 (2003).
 35. Willems, B., Martineau, P. M., Fisher, D., Van Royen, J. & Van Tendeloo, G. Dislocation distributions in brown diamond. *Phys. Status Solidi Appl. Mater. Sci.* **203**, 3076–3080 (2006).
 36. Blumenau, T. *et al.* Dislocations in diamond: Dissociation into partials and their glide motion. *Phys. Rev. B - Condens. Matter Mater. Phys.* **68**, 1–9 (2003).
 37. Barnard, A. S. *The diamond formula: diamond synthesis-a gemological perspective*.

Bibliography

- (Butterworth-Heinemann, 2000).
38. Iakoubovskii, K. *et al.* Reports on Progress in Physics Related content Growth and application of undoped and doped diamond films Growth and application of undoped and doped diamond. (1998).
 39. Ohtsuka, K., Suzuki, K., Sawabe, A. & Inuzuka, T. Epitaxial growth of diamond on iridium. *Japanese J. Appl. Physics, Part 2* **35**, (1996).
 40. Tallaire, A., Kasu, M., Ueda, K. & Makimoto, T. Origin of growth defects in CVD diamond epitaxial films. *Diam. Relat. Mater.* **17**, 60–65 (2008).
 41. Turner, S. *et al.* Direct imaging of boron segregation at dislocations in B:diamond heteroepitaxial films. *Nanoscale* **8**, 2212–2218 (2016).
 42. Ralchenko, V. *et al.* Nanodiamond Seeding for Nucleation and Growth of CVD Diamond Films BT - Synthesis, Properties and Applications of Ultrananocrystalline Diamond. in (eds. Gruen, D. M., Shenderova, O. A. & Vul', A. Y.) 109–124 (Springer Netherlands, 2005).
 43. Dischler, B. & Wild, C. *Low-Pressure Synthetic Diamond*. (Springer, 1998).
 44. Ando, Y. *et al.* Rapid doping of combustion flame CVD diamonds using supersonic expanding nitrogen plasma jets. *Vacuum* **73**, 493–498 (2004).
 45. May, P. W., Harvey, J. N., Smith, J. A. & Mankelevich, Y. A. Reevaluation of the mechanism for ultrananocrystalline diamond deposition from Ar/CH₄/H₂ gas mixtures. *J. Appl. Phys.* **99**, 104907 (2006).
 46. Zhou, D., McCauley, T. G., Qin, L. C., Krauss, A. R. & Gruen, D. M. Synthesis of nanocrystalline diamond thin films from an Ar–CH₄ microwave plasma. *J. Appl. Phys.* **83**, 540 (1998).
 47. Zhou, Y. *et al.* Thermal characterization of polycrystalline diamond thin film heat spreaders grown on GaN HEMTs. *Appl. Phys. Lett.* **111**, (2017).
 48. Kromka, A., Babchenko, O., Izak, T., Hruska, K. & Rezek, B. Linear antenna microwave plasma CVD deposition of diamond films over large areas. *Vacuum* **86**, 776–779 (2012).
 49. Potocký, Š., Babchenko, O., Hruška, K. & Kromka, A. Linear antenna microwave plasma CVD diamond deposition at the edge of no-growth region of C-H-O ternary diagram. *Phys. Status Solidi Basic Res.* **249**, 2612–2615 (2012).
 50. Ficek, M. F. *et al.* Linear antenna microwave chemical vapour deposition of diamond films on long-period fiber gratings for bio-sensing applications. *Opt. Mater. Express* **7**, 32–38 (2017).
 51. Sankaran, K. J. *et al.* Enhanced optoelectronic performances of vertically aligned hexagonal boron nitride nanowalls-nanocrystalline diamond heterostructures. *Sci. Rep.* **6**, 1–11 (2016).
 52. Deshmukh, S. *et al.* Local probing of the enhanced field electron emission of vertically aligned nitrogen-doped diamond nanorods and their plasma illumination properties. *Diam. Relat. Mater.* **83**, 118–125 (2018).
 53. Khan, M. B. & Khan, Z. H. Nanodiamonds: Synthesis and Application. *Nanomaterials and Their Application.* **84**, 1–26 (2017).
 54. Knoll, M. & Ruska, E. Das Elektronenmikroskop. *Zeitschrift für Phys.* **78**, 318–339 (1932).

Bibliography

55. Hawkes, P. W. Ernst ruska. *Phys. Today* **43**, 84–85 (1990).
56. Williams, D. B. & Carter, C. . *Transmission Electron Microscopy*. (Springer, 2009).
57. Hawkes, P. W. *Magnetic Electron Lenses*. (Springer, 1982).
58. De Graef, M. *Introduction to Conventional Transmission Electron Microscopy*. (2002).
59. Hawkes, P. W. & Kasper, E. Principles of Electron Optics : Applied Geometrical Optics. *Acad. Press* **1**, (1989).
60. Verbeeck, J. *et al.* Demonstration of a 2x2 programmable phase plate for electrons. *Ultramicroscopy* **190**, 58–65 (2018).
61. Durnin, J., Miceli, J. & Eberly, J. H. Diffraction-free beams. *Phys. Rev. Lett.* **58**, 1499–1501 (1987).
62. Guzzinati, G. Exploring electron beam shaping in transmission electron microscope. (PhD Thesis, University of Antwerp, 2015).
63. Grillo, V. *et al.* Generation and application of bessel beams in electron microscopy. *Ultramicroscopy* **166**, 48–60 (2016).
64. Verbeeck, J., Tian, H. & Schattschneider, P. Production and application of electron vortex beams. *Nature* **467**, 301 (2010).
65. Bandres, M. A. & Gutiérrez-Vega, J. C. Ince--Gaussian beams. *Opt. Lett.* **29**, 144–146 (2004).
66. Reimer, L. & Kohl, H. *Transmission Electron Microscopy*. (Springer, 2008).
67. Goldstein, J. *et al.* *Scanning Electron Microscopy and X-ray Microanalysis: Third Edition*. (Springer, 2003).
68. Nakaji, D., Grillo, V., Yamamoto, N. & Mukai, T. Contrast analysis of dislocation images in TEM – cathodoluminescence technique. *J. Electron Microsc. (Tokyo)*. **54**, 223–230 (2005).
69. Ciston, J. *et al.* Surface determination through atomically resolved secondary-electron imaging. *Nat. Commun.* **6**, (2015).
70. Allen, L. J., McBride, W., O’Leary, N. L. & Oxley, M. P. Exit wave reconstruction at atomic resolution. *Ultramicroscopy* **100**, 91–104 (2004).
71. Goris, B. *et al.* Measuring Lattice Strain in Three Dimensions through Electron Microscopy. *Nano Lett.* **15**, 6996–7001 (2015).
72. Olivier, E. J. *et al.* Imaging the atomic structure and local chemistry of platelets in natural type Ia diamond. *Nat. Mater.* **17**, 243–248 (2018).
73. De Backer, A., van den Bos, K. H. W., Van den Broek, W., Sijbers, J. & Van Aert, S. StatSTEM: An efficient approach for accurate and precise model-based quantification of atomic resolution electron microscopy images. *Ultramicroscopy* **171**, 104–116 (2016).
74. Alania, M. *et al.* Depth sectioning combined with atom-counting in HAADF STEM to retrieve the 3D atomic structure. *Ultramicroscopy* **177**, 36–42 (2017).
75. Van Den Bos, K. H. W. *et al.* Unscrambling Mixed Elements using High Angle Annular Dark

Bibliography

- Field Scanning Transmission Electron Microscopy. *Phys. Rev. Lett.* **116**, 1–6 (2016).
76. Jones, L. *et al.* Smart Align---a new tool for robust non-rigid registration of scanning microscope data. *Adv. Struct. Chem. Imaging* **1**, 8 (2015).
77. Wang, J.-T. *et al.* Body-Centered Orthorhombic C16: A Novel Topological Node-Line Semimetal. *Phys. Rev. Lett.* **116**, 195501 (2016).
78. Jones, L. & Nellist, P. D. Identifying and Correcting Scan Noise and Drift in the Scanning Transmission Electron Microscope. *Microsc. Microanal.* **19**, 1050–1060 (2013).
79. Egerton, R. F. *Electron Energy-Loss Spectroscopy in the Electron Microscope.* (2011).
80. Krivanek, O. L. *et al.* Vibrational spectroscopy in the electron microscope. *Nature* **514**, 209–12 (2014).
81. Verbeeck, J. Electron energy loss spectroscopy of nanoscale materials. *PhD Thesis* (University of Antwerp, 2002).
82. Inokuti, M. Inelastic Collisions of Fast Charged Particles with Atoms and Molecules---The Bethe Theory Revisited. *Rev. Mod. Phys.* **43**, 297–347 (1971).
83. García De Abajo, F. J. Optical excitations in electron microscopy. *Rev. Mod. Phys.* **82**, 209–275 (2010).
84. Ritchie, R. . Plasma Losses by Fast Electrons in Thin Films. *Phys. Rev.* **106**, (1957).
85. Fossard, F. *et al.* Angular resolved electron energy loss spectroscopy in hexagonal boron nitride. *arXiv:1701.05119* 1–16 (2017).
86. Stöger-Pollach, M., Laister, A. & Schattschneider, P. Treating retardation effects in valence EELS spectra for Kramers-Kronig analysis. *Ultramicroscopy* **108**, 439–444 (2008).
87. Kröger, E. Transition radiation Cerenkov radiation and energy losses of relativistic charged particles traversing thin foils at oblique incidence. *Zeitschrift f. Phys.* 403–421 (1970).
88. Erni, R. & Browning, N. D. The impact of surface and retardation losses on valence electron energy-loss spectroscopy. *Ultramicroscopy* **108**, 84–99 (2008).
89. Kittel, C. *Introduction to Solid State Physics.*
90. Park, J. *et al.* Bandgap measurement of thin dielectric films using monochromated STEM-EELS. *Ultramicroscopy* **109**, 1183–1188 (2009).
91. Erni, R. On the validity of the Cherenkov limit as a criterion for precise band gap measurements by VEELS. *Ultramicroscopy* **160**, 80–83 (2016).
92. Stöger-Pollach, M. Optical properties and bandgaps from low loss EELS: Pitfalls and solutions. *Micron* **39**, 1092–1110 (2008).
93. Vatanparast, M. *et al.* Bandgap measurement of high refractive index materials by off-axis EELS. *Ultramicroscopy* **182**, (2016).
94. Stöger-Pollach, M., Schachinger, T., Biedermann, K. & Beyer, V. Valence EELS below the limit of inelastic delocalization using conical dark field EFTEM or Bessel beams. *Ultramicroscopy* **173**, 24–30 (2017).

Bibliography

95. Korneychuk, S. *et al.* Exploring possibilities of band gap measurement with off-axis EELS in TEM. *Ultramicroscopy in press*, (2018).
96. Gu, L. *et al.* Band-gap measurements of direct and indirect semiconductors using monochromated electrons. *Phys. Rev. B - Condens. Matter Mater. Phys.* **75**, 1–8 (2007).
97. Liu, Q., March, K. & Crozier, P. A. Nanoscale Probing of bandgap states on oxide particles using electron energy-loss spectroscopy. *Ultramicroscopy* **June**, 1–10 (2016).
98. Slater, J. C. A Simplification of the Hartree-Fock Method. *Phys. Rev.* **81**, 385–390 (1951).
99. Verbeeck, J. & Bertoni, G. Deconvolution of core electron energy loss spectra. *Ultramicroscopy* **109**, 1343–1352 (2009).
100. Verbeeck, J. & Van Aert, S. Model based quantification of EELS spectra. *Ultramicroscopy* **101**, 207–224 (2004).
101. Jensen, K. L. *Field emitter arrays for plasma and microwave source applications. Physics of Plasmas* **6**, (1999).
102. J. Powers, M. *et al.* Observation of a negative electron affinity for boron nitride. *Applied Physics Letters* **67**, (1995).
103. Harniman, R. L. *et al.* Direct observation of electron emission from grain boundaries in CVD diamond by PeakForce-controlled tunnelling atomic force microscopy. *Carbon N. Y.* **94**, 386–395 (2015).
104. Jothiramalingam, S., Kunuku, S., Leou, K. C., H. Tai, N. & Lin, I. *High stability electron field emitters made of nanocrystalline diamond coated carbon nanotubes. Applied Physics Letters* **103**, (2013).
105. Ghassemi, H. M., Lee, C. H., Yap, Y. K. & Yassar, R. S. Field emission and strain engineering of electronic properties in boron nitride nanotubes. *Nanotechnology* **23**, (2012).
106. Liu, N. *et al.* Patterned Growth and Field-Emission Properties of AlN Nanocones. *ACS Appl. Mater. Interfaces* **1**, 1927–1930 (2009).
107. Li, Y. B., Bando, Y., Golberg, D. & Kurashima, K. Field emission from MoO₃ nanobelts. *Appl. Phys. Lett.* **81**, 5048–5050 (2002).
108. Lin, J. *et al.* Synthesis of In₂O₃ Nanowire-Decorated Ga₂O₃ Nanobelt Heterostructures and Their Electrical and Field-Emission Properties. *ACS Nano* **4**, 2452–2458 (2010).
109. Yang, T.-H., Harn, Y.-W., Chiu, K.-C., Fan, C.-L. & Wu, J.-M. Promising electron field emitters composed of conducting perovskite LaNiO₃ shells on ZnO nanorod arrays. *J. Mater. Chem.* **22**, 17071–17078 (2012).
110. Kim, H., Jeon, S., Lee, M., Lee, J. & Yong, K. Fabrication of a novel hierarchical assembly of ZnO nanowires on WO_x nanowhiskers for highly efficient field electron emission. *J. Mater. Chem.* **21**, 13458 (2011).
111. Sankaran, K. J. *et al.* Hierarchical hexagonal boron nitride nanowall–diamond nanorod heterostructures with enhanced optoelectronic performance. *RSC Adv.* **6**, 90338–90346 (2016).

Bibliography

112. Sun, Y. *et al.* Field emission behavior of carbon nanotube field emitters after high temperature thermal annealing. *AIP Adv.* **4**, (2014).
113. Dean, K. A., Burgin, T. P. & Chalamala, B. R. Evaporation of carbon nanotubes during electron field emission. *Appl. Phys. Lett.* **79**, 1873–1875 (2001).
114. Kern, W. & Soc, J. E. The Evolution of Silicon Wafer Cleaning Technology. *J. Electrochem. Soc.* **137**, 1887–1892 (1990).
115. Forbes, R. G. Extraction of emission parameters for large-area field emitters, using a technically complete Fowler–Nordheim-type equation. *Nanotechnology* **23**, 95706 (2012).
116. Cumings, J. & Zettl, A. Field emission and current-voltage properties of boron nitride nanotubes. *Solid State Commun.* **129**, 661–664 (2004).
117. Fowler, R. H. & Nordheim, L. Electron field emission in intense electric fields. *Proc. R. Soc. London, Ser. A.* **119** 173–181 (1928).
118. Mirkarimi, P. B., McCarty, K. F. & Medlin, D. L. Review of advances in cubic boron nitride film synthesis. *Mater. Sci. Eng. R Reports* **21**, 47–100 (1997).
119. Hoang, D. Q. *et al.* Direct nucleation of hexagonal boron nitride on diamond: Crystalline properties of hBN nanowalls. *Acta Mater.* **127**, 17–24 (2017).
120. Kim, S.-K. *et al.* Efficient catalytic conversion of ammonia borane to borazine and its use for hexagonal boron nitride (white graphene). *J. Mater. Chem. A* **1**, 1976–1981 (2013).
121. Loiseau, A., Willaime, F., Demoncey, N., Hug, G. & Pascard, H. Boron nitride nanotubes with reduced numbers of layers synthesized by arc discharge. *Phys. Rev. Lett.* **76**, 4737–4740 (1996).
122. Turner, S. Transmission Electron Microscopy: Characterisation of O - D Nanomaterials. (University of Antwerp, 2010).
123. Fang, X., Bando, Y., Gautam, U. K., Ye, C. & Golberg, D. Inorganic semiconductor nanostructures and their field-emission applications. *J. Mater. Chem.* **18**, 509–522 (2008).
124. Drijkoningen, S. *et al.* On the Origin of Diamond Plates Deposited at Low Temperature. *Cryst. Growth Des.* **17**, 4306–4314 (2017).
125. Angus, J. C., Sunkara, M., Sahaida, S. R. & Glass, J. T. Twinning and faceting in early stages of diamond growth by chemical vapor deposition. *J. Mater. Res.* **7**, 3001–3009 (1992).
126. Alexeev, A. M. *et al.* Diamond platelets produced by chemical vapor deposition. *Diam. Relat. Mater.* **65**, 13–16 (2016).
127. Frondel, C. & Marvin, U. Lonsdaleite, a Hexagonal Polymorph of Diamond. *Nature* **214**, 587 (1967).
128. Shenderova, O. a. & Gruen, D. M. *Ultrananocrystalline Diamond: Synthesis, Properties and Applications.* (2012).
129. Sunkara, M. K. Monte-Carlo Simulation of Diamond Nucleation and Growth. (Case Western Reserve University, 1993).

Bibliography

130. Ringe, E., Van Duyne, R. P. & Marks, L. D. Kinetic and Thermodynamic Modified Wulff Constructions for Twinned Nanoparticles. *J. Phys. Chem. C* **117**, 15859–15870 (2013).
131. Butler, J. E. & Oleynik, I. A. Mechanism for Crystal Twinning in the Growth of Diamond by Chemical Vapour Deposition. *Philos. Trans. R. Soc., A* **366**, 295–311 (2008).
132. Evans, T. & Phaal, C. Imperfections in Type I and Type II Diamonds. *Proc. R. Soc. A* **270**, 538–552 (1962).
133. Kiflawi, I. & Lang, A. R. R. Polarised infrared cathodoluminescence from platelet defects in natural diamonds. *Nature* **267**, 36 (1977).
134. Humble, P. The Structure and Mechanism of Formation of Platelets in Natural Type Ia Diamond. *Proc. R. Soc. A Math. Phys. Eng. Sci.* **381**, 65–81 (1982).
135. Bosak, A., Chernyshov, D., Krisch, M. & Dubrovinsky, L. Symmetry of platelet defects in diamond: New insights with synchrotron light. *Acta Crystallogr. Sect. B Struct. Sci.* **66**, 493–496 (2010).
136. Barry, J. C., Bursill, L. A. & Hutchison, J. L. On the structure of {100} platelet defects in type Ia diamond. *Philos. Mag. A* **51**, 15–49 (1985).
137. Davies, G. The A nitrogen aggregate in diamond-its symmetry and possible structure. *J. Phys. C Solid State Phys.* **9**, L537 (1976).
138. Walkert, J. & Walker, J. Optical absorption and luminescence in diamond. *Reports Prog. Phys.* **42**, 1605 (1979).
139. Lang, A. R. A proposed structure for nitrogen impurity platelets in diamond. *Proc. Phys. Soc.* **84**, 871–876 (1984).
140. Evans, T. & Qi, Z. The Kinetics of the Aggregation of Nitrogen Atoms in Diamond. *Proc. R. Soc. A Math. Phys. Eng. Sci.* **381**, 159–178 (1982).
141. Kiflawi, I., Bruley, J., Luyten, W. & Van Tendeloo, G. ‘Natural’ and ‘man-made’ platelets in type-Ia diamonds. *Philos. Mag. B Phys. Condens. Matter; Stat. Mech. Electron. Opt. Magn. Prop.* **78**, 299–314 (1998).
142. Humble, P. The Structure and Mechanism of Formation of Platelets in Natural Type Ia Diamond. *Proc. R. Soc. A* **381**, 65–81 (1982).
143. Goss, J. P., Briddon, P. R., Jones, R. & Heggie, M. I. Platelets and the $\langle 110 \rangle$ $\frac{a_0}{4}$ {001} stacking fault in diamond. *Phys. Rev. B* **73**, 115204 (2006).
144. Korneychuk, S., Turner, S., Abakumov, A. & Verbeeck, J. Determination of the platelet structure in natural diamond by ADF-STEM. in *European Microscopy Congress 2016: Proceedings* (2016).
145. Nastasi, M. *et al.* Nucleation and growth of platelets in hydrogen-ion-implanted silicon. *Appl. Phys. Lett.* **86**, 1–3 (2005).
146. Rose, H. H. Optics of high-performance electron microscopes. *Sci. Technol. Adv. Mater.* **9**, (2008).
147. Buban, J. P., Ramasse, Q., Gipson, B., Browning, N. D. & Stahlberg, H. High-resolution low-dose

Bibliography

- scanning transmission electron microscopy. *J. Electron Microsc. (Tokyo)*. **59**, 103–112 (2010).
148. Krizhevsky, A., Sutskever, I. & Hinton, G. E. ImageNet Classification with Deep Convolutional Neural Networks. *Adv. Neural Inf. Process. Syst.* 1–9 (2012). doi:http://dx.doi.org/10.1016/j.protcy.2014.09.007
 149. Van Aert, S. *et al.* Quantitative atomic resolution mapping using high-angle annular dark field scanning transmission electron microscopy. *Ultramicroscopy* **109**, 1236–1244 (2009).
 150. Kresse, G. & Furthmüller, J. Efficiency of ab-initio total energy calculations for metals and semiconductors using a plane-wave basis set. *Comput. Mater. Sci.* **6**, 15–50 (1996).
 151. Kresse, G. & Furthmüller, J. Efficient iterative schemes for ab initio total-energy calculations using a plane-wave basis set. *Phys. Rev. B* **54**, 11169–11186 (1996).
 152. Perdew, J. P., Burke, K. & Ernzerhof, M. Generalized Gradient Approximation Made Simple. *Phys. Rev. Lett.* **77**, 3865–3868 (1996).
 153. Iakoubovskii, K. & Adriaenssens, G. J. Characterization of platelet-related infrared luminescence in diamond. *Philos. Mag. Lett.* **80**, 441–444 (2000).
 154. Koch, C. Determination of core structure periodicity and point defect density along dislocations. (Arizona State University, 2002).
 155. Verbeeck, J. & Van Aert, S. Model based quantification of EELS spectra. *Ultramicroscopy* **101**, 207–224 (2004).
 156. Turner, S. *et al.* Aberration-corrected microscopy and spectroscopy analysis of pristine , nitrogen containing detonation nanodiamond Invited Article. *Phys. Status Solidi A* **198A**, 1976–1984 (2013).
 157. Brydson, R., Brown, L. M. & Bruley, J. Characterizing the local nitrogen environment at platelets in type IaA / B diamond. *J. Microsc.* **189**, 137–144 (1998).
 158. Gutiérrez-Sosa, A. *et al.* Band-gap-related energies of threading dislocations and quantum wells in group-III nitride films as derived from electron energy loss spectroscopy. *Phys. Rev. B - Condens. Matter Mater. Phys.* **66**, 353021–3530210 (2002).
 159. Lakner, H., Rafferty, B. & Brockt, G. Electronic structure analysis of (In,Ga,Al)N heterostructures on the nanometre scale using EELS. *J. Microsc.* **194**, 79–83 (1999).
 160. Batson, P. E., Kavanagh, K. L., Woodall, J. M. & Mayer, J. W. Electron-energy-loss scattering near a single misfit dislocation at the GaAs/GaInAs interface. *Phys. Rev. Lett.* **57**, 2729–2732 (1986).
 161. Lazar, S., Botton, G. A., Wu, M. Y., Tichelaar, F. D. & Zandbergen, H. W. Materials science applications of HREELS in near edge structure analysis and low-energy loss spectroscopy. *Ultramicroscopy* **96**, 535–546 (2003).
 162. Cherenkov, P. A. Visible emission of clean liquids by action of γ radiation. *Dokl. Akad. Nauk USSR* **2**, (1934).
 163. Vavilov, S. I. On the possible causes of blue γ -glow of liquids. *Dokl. Akad. Nauk USSR* **2**, (1934).

Bibliography

164. Couillard, M., Kociak, M., Stéphan, O., Botton, G. A. & Colliex, C. Multiple-interface coupling effects in local electron-energy-loss measurements of band gap energies. *Phys. Rev. B - Condens. Matter Mater. Phys.* **76**, 2–6 (2007).
165. Egerton, R. F. Electron Energy-Loss Spectroscopy in the TEM. *Reports Prog. Phys.* **72**, 16502 (2009).
166. Zhang, L., Erni, R., Verbeeck, J. & Van Tendeloo, G. Retrieving the dielectric function of diamond from valence electron energy-loss spectroscopy. *Phys. Rev. B* **77**, 1–7 (2008).
167. Zhang, L., Turner, S., Brosens, F. & Verbeeck, J. Model-based determination of dielectric function by STEM low-loss EELS. *Phys. Rev. B - Condens. Matter Mater. Phys.* **81**, 1–6 (2010).
168. Zhang, L. Electron energy loss spectroscopy Fundamental aspects and its application to diamond. (PhD Thesis, University of Antwerp, 2010).
169. Egerton, R. F. *Electron Energy-Loss Spectroscopy in the Electron Microscope*. (Springer, 2011).
170. Vatanparast, M., Egoavil, R., Reenaas, T. W., Verbeeck, J. & Vullum, P. E. Bandgap measurement of high refractive index materials by off-axis EELS. *Ultramicroscopy* **182**, (2017).
171. Gu, L. *et al.* Mapping of valence energy losses via energy-filtered annular dark-field scanning transmission electron microscopy. *Ultramicroscopy* **109**, 1164–1170 (2009).
172. Egerton, R. F. & Bergen, M. <http://www.tem-eels.ca/computer-programs/>.
173. Saitoh, K., Hirakawa, K., Nambu, H., Tanaka, N. & Uchida, M. Generation of Electron Bessel Beams with Nondiffractive Spreading by a Nanofabricated Annular Slit. *J. Phys. Soc. Japan* **85**, (2016).
174. Lobato, I., van Aert, S. & Verbeeck, J. Progress and new advances in simulating electron microscopy datasets using MULTEM. *Ultramicroscopy* **168**, 17–27 (2016).
175. Born, M. & Wolf, E. *Principles of Optics*. (Pergamon Press, 1970).
176. Kuno, M. *Introductory Nanoscience*. (Garland Science, 2011).
177. Kittel, C. *Introduction to Solid State Physics*. (J.Wiley&Sons, 2005).
178. Gildenblat, G. S. & Schmidt, P. E. *Handbook Series on Semiconductor Parameters*. **1**, (World Scientific, London, 1996).
179. Rafferty, B. & Brown, L. Direct and indirect transitions in the region of the band gap using electron-energy-loss spectroscopy. *Phys. Rev. B* **58**, 10326–10337 (1998).
180. Tauc, J. Optical properties and electronic structure of amorphous Ge and Si. *Mater. Res. Bull.* **3**, 37–46 (1968).
181. Egerton, R. F., McLeod, R. A. & Malac, M. Validity of the dipole approximation in TEM-EELS studies. *Microsc. Res.* **77**, 773–778 (2014).
182. Löffler, S., Ennen, I., Tian, F., Schattschneider, P. & Jaouen, N. Breakdown of the dipole approximation in core losses. *Ultramicroscopy* **111**, 1163–1167 (2011).
183. Uhlemann, S., Muller, H., Hartel, P., Zach, J. & Haider, M. Thermal magnetic field noise limits

- resolution in transmission electron microscopy. *Phys. Rev. Lett.* **111**, 1–5 (2013).
184. Strite, S. & Morkoc, H. GaN, AlN, and InN: A review. *J. Vac. Sci. Technol. B Microelectron. Nanom. Struct.* **10**, 1237 (1992).
 185. Schattschneider, P., Hébert, C., Franco, H. & Jouffrey, B. Anisotropic relativistic cross sections for inelastic electron scattering, and the magic angle. *Phys. Rev. B - Condens. Matter Mater. Phys.* **72**, (2005).
 186. Calzaferri, G. & Rytz, R. The Band Structure of Diamond. *J. Phys. Chem.* **100**, 11122–11124 (1996).
 187. Kuno, M. *Introductory nanoscience: physical and chemical concepts*. (Garland Science, 2012).
 188. Jouffrey, B., Schattschneider, P. & Hébert, C. The Magic Angle: a solved mystery. *Ultramicroscopy* **102**, 61–66 (2004).
 189. Dileep, K., Sahu, R., Sarkar, S., Peter, S. C. & Datta, R. Layer specific optical band gap measurement at nanoscale in MoS₂ and ReS₂ van der Waals compounds by high resolution electron energy loss spectroscopy. *J. Appl. Phys.* **119**, (2016).
 190. Stöger-Pollach, M. & Schattschneider, P. The influence of relativistic energy losses on bandgap determination using valence EELS. *Ultramicroscopy* **107**, 1178–1185 (2007).
 191. Granerød, C. S., Zhan, W. & Prytz, Ø. Automated approaches for band gap mapping in STEM-EELS. *Ultramicroscopy* **184**, 39–45 (2018).
 192. Hart, J. L. *et al.* Direct Detection Electron Energy-Loss Spectroscopy: A Method to Push the Limits of Resolution and Sensitivity. *Sci. Rep.* **7**, 1–14 (2017).
 193. Schattschneider, P., Hébert, C. & Jouffrey, B. Orientation dependence of ionization edges in EELS. *Ultramicroscopy* **86**, 343–353 (2001).
 194. Bringans, R. D. & Liang, W. Y. Journal of Physics C : Solid State Physics Related content Energy bands of the cadmium halides from electron energy loss spectroscopy Energy bands of the cadmium halides from electron energy loss spectroscopy. (1981).
 195. Liu, X., Li, L., Li, Q., Li, Y. & Lu, F. Optical and mechanical properties of C, Si, Ge, and 3C-SiC determined by first-principles theory using Heyd-Scuseria-Ernzerhof functional. *Mater. Sci. Semicond. Process.* **16**, 1369–1376 (2013).

Thanks

It has been long four years since I started my PhD but at the same moment I feel that the time passed very quickly. During these years I have experienced many bright episodes in my research and many more when nothing was working again. The first ones were always compensating the last. However, my way through PhD would not be such fun if I did not share all this with a few people.

Firstly, I want to thank my promoter, Jo Verbeeck, for giving me the opportunity to join EMAT and work in such interesting environment. I learned a lot during my PhD and, thanks to his guidance, was able to face the unexplored. He could always inspire me with new ideas and provide a great scientific expertise.

I also want to thank Stuart Turner who guided me at the first steps and opened the world of TEM for me spending many hours at the microscope and patiently answering my newbie questions. He taught me the essentials of the craft of electron microscopy.

Next, I would like to thank Sankaran, Rajesh, Sien, Quang and Ken Haenen from Hasselt University for the fruitful collaboration and diamond-based samples of high quality.

Many thanks to my current and former colleagues at EMAT for their help and excellent competence: Marnik provided me with theory insights; Artem shared his knowledge about defects and crystallography; Armand, Nico, Ricardo, Olesia and Dmitri gave a hand at the microscope and a scientific advice.

Special thanks to Giulio who showed me how far you can push the microscope outside the limits of the conventional TEM and also was able to withstand my emotional state during the long months of PhD writing.

And, finally, I want to thank my mom for her support, understanding and help in releasing a bit of stress during my PhD journey.